LA--12533-T

DE93 011570

Partial Cross Sections in H^- Photodetachment

Monica Halka

Los Alamos
NATIONAL LABORATORY
Los Alamos, New Mexico 87545

MASTER

ACKNOWLEDGEMENTS

I am deeply grateful to my advisor and supervisor, Howard Bryant, whose uncommon patience has carried me through my graduate work, and whose tutorship has helped me learn how to approach a question from many different angles. It has been a great honor to work with such a fine and gentle man.

The benefits of the companionship of my coworker, fellow graduate student, and friend of many years, Ed MacKerrow, cannot be overrated. Conversations with Ed have always helped to sort out confusing ideas, and his presence has been a comfort during stressful times.

I am also grateful to Amir Mohagheghi and Chen-Yau Tang, former members of this experimental group for helping to familiarize me with the setup. I am grateful to a former graduate student, Phil Harris, for allowing me to analyze and use in this thesis the electric field data acquired in 1989. Bill Miller, the group's technician and source of electronics expertise, I thank for injecting a note of sanity into everyday life.

I thank Stan Cohen, a LAMPF staff member and ongoing collaborator, for his in-depth computer knowledge and his empathetic understanding of graduate student trials and tribulations. The help of another LAMPF staff member and collaborator with the UNM group, Bob Quick, was invaluable. I am especially grateful for his partnership on all-night shifts during experimental runs and for his continued willingness to discuss physics problems during his incredibly busy schedule.

Other LAMPF staff members, without whom this experimental work might not have happened, include Joe Tiee, Albert Hsu, Joey Donahue, Art Gonzales, Fred Montoya, and Alma Sondreal.

The assistance of Jim Hontas at the UNM Physics Department shop is greatly appreciated for his help in building the Čerenkov detector. I also wish to thank Randy Reeder, a UNM postdoc, for physics discussions and for his constant good nature, which brightened many gloomy days.

Many atomic theorists have been extremely (inordinately) patient in answering my questions on theory. I wish to thank Chris Greene for discussions on MQDT pertaining to H^-, Hossein Sadeghpour for sharing his data before publication and for late-night telephone conversations concerning physics and life, Chii-Dong Lin and Bin Zhou for their help in understanding electric field effects, Tony Starace and Joe Macek for their help in understanding the shape resonance partial decay, John Briggs and Jan-Michael Rost for explanations of prolate spheroidal coordinates and propensity rules, and David Harmin for his lecture notes and e-mail.

Last but not least, I am grateful to my former advisor, Bernd Bassalleck, for his encouragement and moral support—even after I deserted his experimental group. All the above-mentioned people have been good friends, and for this I give the most thanks.

PARTIAL CROSS SECTIONS IN H$^-$ PHOTODETACHMENT

by

Monica H. Halka

ABSTRACT

This dissertation reports experimental measurements of partial decay cross sections in the H$^-$ photodetachment spectrum. Observed decays of the $^1P^o$ H$^{-**}(n)$ doubly-excited resonances to the H(N=2) continuum are reported for n=2, 3, and 4 from 1990 runs in which the author participated. A recent analysis of 1989 data revealing effects of static electric fields on the partial decay spectrum above 13.5 eV is also presented.

The experiments were performed at the High Resolution Atomic Beam Facility (HIRAB), the Los Alamos Meson Physics Facility (LAMPF), with a relativistic H$^-$ beam (β=0.842) intersecting a Nd:YAG laser. Variation of the intersection angle amounts to Doppler-shifting the photon energy, allowing continuous tuning of the laser energy as viewed from the moving ions' frame.

The H^{-**}(3) data thus obtained are the first clear evidence that the H$^-$ resonances should decay preferentially to the nearest energetically accessible continuum channel. The resonance profiles agree with theoretical predictions of Sadeghpour *et al* [1] who used R-matrix methods. An experimental determination of the $n=2$ shape resonance branching ratio is reported, wherein the shape resonance is shown to prefer the H(2) channel for energies between 10.975 and 11.2 eV.

The applied electric field data obtained in 1989 display unpredicted, large downward shifts in the threshold energy, field-induced resonances in the threshold region, and the expected weakening or disappearance of the resonances normally observed in zero-field. First evidence is presented of a Feshbach resonance being transformed to a shape resonance by a static field. The threshold shifts and much of the structure have been identified by Zhou and Lin using hyperspherical treatment.

Contents

1 Introduction 1

1.1 General History of Autoionizing States 1

1.1.1 Two Very Different Types of Resonance: Feshbach and Shape 9

1.1.2 Convenient Coordinate Representations 10

1.2 H⁻ Resonances Observed in the Total Cross Section 14

1.3 Observations of Partial Decay of Autoionizing States 15

1.4 Threshold Behavior 16

1.5 Physical Motivation for Measurement of Partial Cross Sections 16

2 Theory of Partial Decay 18

2.1 Shape Resonance Partial Decay in Zero Field 18

2.2 Partial Decay of n=3 and 4 Resonances 21

2.3 Partial Cross Sections in Static Electric Fields 23

2.3.1 Thresholds 24

2.3.2 Resonances in Applied Fields 31

3 Experimental Method 33

3.1 The LAMPF H^- Beam 33

3.2 Relativity's Role 37

3.3 Energy Resolution 38

3.4 1990 Apparatus 40

3.5 1989 Apparatus 48

3.6 Beam alignment aids 50

4 Gadgets 51

4.1 Laser and Optics 51

4.2 Detectors 54

4.2.1 Electron Spectrometer 54

4.2.2 Čerenkov detector 57

4.2.3 Faraday Cup 59

5 Data Acquisition 62

5.1 Hardware 62

5.2 Software 71

6 Data Analysis 74

6.1 1990 Analysis 74

6.1.1 Cross Section Calculations 76

6.1.2 Background Subtraction 77

6.1.3 Energy Calibration and Resolution 77

6.1.4 Fitting the Data 79
6.1.5 Systematic Errors 80
6.2 1989 Analysis 83
6.2.1 Fitting the Data 83

7 Results and Conclusions **85**

7.1 Partial Decay into H(2) by Excited H^- near the n=3 and 4 Thresholds 85
7.2 Shape Resonance Branching Ratio Measurement 93
7.2.1 $H^{-**}(2) \rightarrow H(2)$ Partial Cross Section 97
7.2.2 The Shape Resonance Total Cross Section 100
7.2.3 The Branching Ratio 102
7.3 Field-Induced Structure and Threshold Shifts 102

8 Summary and Outlook **121**

8.1 Summary 121
8.2 Outlook 123

A Relativistic transformations **126**

B Hyperspherical Coordinates **129**

C Prolate Spheroidal Coordinates **134**

D Propensity Rules **136**

E Q-program PROC8.FOR **138**

F CAMAC Module List 142

G Fano fits 145

H Fano parameters for resonances in applied fields 160

I Shape resonance data of J. Callaway 162

J Shape resonance width 163

List of Figures

1.1 Various resonance asymmetries. 4

1.2 '+' and '−' states of H^-. 8

1.3 $^1P^o$ adiabatic curves of H^-. 12

1.4 Dominant $^1P^o$ potential curves. 13

2.1 Dipole potential barrier lowered by applied-field potential. 26

2.2 Potential as a function of R for the N=4 manifold. 28

2.3 N=4 diabatic potentials in 87 kV/cm field. 30

3.1 Optically-pumped polarized ion source. 34

3.2 The LAMPF beamline. 36

3.3 $\delta\alpha$ and δp contributions to the energy resolution. 39

3.4 The HIRAB beamline. 41

3.5 The interaction regions. 43

3.6 The mirror arrangement. 44

3.7 The 1989 setup for electric field studies in the first and only scattering chamber. 49

4.1 Schematic diagram of the Nd:YAG laser. 52

4.2 YAG energy levels of interest. 53

4.3 Prism harmonic separator. 55

4.4 The electron spectrometer. 56

4.5 The Čerenkov detector. 58

4.6 The Faraday cup. 60

5.1 Digital electronics circuits. 63

5.2 Digital electronics circuits. 64

5.3 Digital electronics circuits. 65

5.4 Digital electronics circuits. 66

5.5 Digital electronics circuits. 67

5.6 Digital electronics circuits. 68

5.7 Laser event and background timing diagram. 70

6.1 n=2 Feshbach resonance. 78

6.2 Shape resonance $2s$ and $2p$ profiles. 82

7.1 Lowest $H^{-**}(3)$ resonance. 86

7.2 Lowest $H^{-**}(4)$ resonance. 87

7.3 Entire $H^{-**}(4)$ resonance region compared with R-matrix theory. . . . 88

7.4 Theoretical n=4 partial cross sections. 90

7.5 Fano profiles for the lowest $H^{-**}(3)$ total and partial cross section. . . 91

7.6 Theoretical n=3 partial cross sections. 92

7.7 Theoretical photodetachment partial cross section vs energy above the threshold for production of H(2) plus a free electron. 96

7.8 Shape resonance partial cross section compared with theories of Liu et al and Hyman et al. 98

7.9 Shape resonance partial cross section compared with theories of Sadeghpour et al and Broad and Reinhardt. 99

7.10 Photodetachment total cross section vs photon energy near the n=2 threshold. 101

7.11 Shape resonance branching ratio vs photon energy. 103

7.12 Photodetachment of H^- with detection of fragment H(4) atom for F=0 and 13 kV/cm. 104

7.13 Photodetachment of H^- with detection of fragment H(4) atom for F=25 and 38 kV/cm. 105

7.14 Photodetachment of H^- with detection of fragment H(4) atom for F=63 and 87 kV/cm. 106

7.15 Photodetachment of H^- with detection of fragment H(5) atom for F=0 and 13 kV/cm. 107

7.16 Photodetachment of H^- with detection of fragment H(5) atom for F=38 and 50 kV/cm. 108

7.17 Photodetachment of H^- with detection of fragment H(5) atom for F=63 and 75 kV/cm. 109

7.18 Photodetachment of H^- with detection of fragment H(6) atom for F=0, 13, and 25 kV/cm. 110

7.19 Thresholds fit to a step function. 112

7.20 Threshold shift ΔE relative to the zero-field threshold vs field strength. 113

7.21 Fano parameters from fits to first $H^{-**}(5)$ for various field magnitudes. 117

7.22 Fano parameters from fits to second $H^{-**}(5)$ for various field magnitudes. 118

7.23 Fano parameters from fits to first $H^{-**}(6)$ for various field magnitudes. 119

7.24 Fano parameters from fits to second $H^{-**}(6)$ for various field magnitudes. 120

B.1 Diabatic potential curves. 131

G.1 Lowest resonance in n=5 manifold with F=0. 145

G.2 Lowest resonance in n=5 manifold with F=13 and 25 kV/cm. 146

G.3 Lowest resonance in n=5 manifold with F=38 and 63 kV/cm. 147

G.4 Lowest resonance in n=5 manifold with F=87 kV/cm. 148

G.5 Second resonance in n=5 manifold with F=0 and 2.5 kV/cm. 149

G.6 Second resonance in n=5 manifold with F=5 and 7.5 kV/cm. 150

G.7 Second resonance in n=5 manifold with F=10 and 11 kV/cm. 151

G.8 Second resonance in n=5 manifold with F=13 and 25 kV/cm. 152

G.9 Second resonance in n=5 manifold with F=38 and 63 kV/cm. 153

G.10 Second resonance in n=5 manifold with F=87 kV/cm. 154

G.11 Lowest resonance in n=6 manifold with F=0 and 13 kV/cm. 155

G.12 Lowest resonance in n=6 manifold with F=25 and 38 kV/cm. 156

G.13 Lowest resonance in n=6 manifold with F=50 and 63 kV/cm. 157

G.14 Lowest resonance in n=6 manifold with F=75 and 87 kV/cm. 158

G.15 Lowest resonance in n=3 and 4 manifolds. 159

List of Tables

2.1 Dipole parameter α relevant to H$^-$ photodetachment accompanied by excitation of H(n). 25

7.1 Fano parameters for the first resonances near n=3 and n=4 thresholds. 86

7.2 Fano parameters and χ^2/ν values from fits to total and partial shape resonance cross sections. 95

Chapter 1

Introduction

1.1 General History of Autoionizing States

The simplest three-body atomic system, the negative hydrogen ion, H^-, is the most interesting of the two-electron ions because the electron correlations are especially strong; the usual approximation that the two electrons move in hydrogen-like orbits with their mutual interaction modeled by a screening constant is grossly inadequate. In fact, this independent-particle approximation predicts H^- to be unbound—evidence that the correlations between the two electrons as they move about the proton must be carefully considered [2]. These correlations make possible the existence of doubly-excited states, or H^- resonances designated here as H^{-**}, where both electrons have a principal quantum number greater than one.

Since the late 1960s the study of photodetachment of negative ions has brought to light many unique properties of correlated-electron systems. Experimental work performed with and without applied electromagnetic fields has facilitated a steadily increasing understanding of processes involved. Theory has so far been able to explain or predict the general behavior of cross sections and resonance energies and widths, but mysteries remain, especially when external fields are involved.

The correlations between interacting atomic electrons are intricate, making calculation difficult. The dynamics, especially for high-n excitations, is not completely understood, and much controversy still flares concerning the mechanisms of double escape (when both electrons are detached by one photon). Each year the H^- experiments performed by the UNM/LAMPF group contribute a little more understanding of the three-body Coulomb problem.

Theoretical work on quasibound or "autoionizing" resonant states of two-electron ions, in which both electrons are excited out of their ground states by a photon with an energy greater than the electron affinity of the neutral atom, was initially stimulated by experimental observation. Before 1957 it was generally understood that negative ions should have no structure in the detachment cross section above the binding energy of the outermost electron. An indication to the contrary was provided in an electron-helium scattering experiment, when Schulz [3] observed a linear rise with $\Delta E = E - E_{threshold}$ in the cross section above the single electron detachment threshold. The Wigner theory [4] had predicted a $\sqrt{\Delta E}$ dependence. This unexpected behavior was interpreted [5] as evidence for a Breit-Wigner type resonance above threshold—a doubly-excited state embedded in the continuum of free electrons.

Such resonant states do not always form a peak in the cross section. They can be dips, or a combination of dip and peak as shown in Figure 1.1. We recall that in the Breit-Wigner description the resonant cross sections may be written in terms of a shift in the resonance's phase. When the resonance profile (plot of cross section vs energy) is asymmetric, interference is suspected. Interference can be a result of forces which are independent of energy—centrifugal forces, for example, or continuum interference. In H–e$^-$ scattering calculations, introduction of a partial wave phase shift for potential scattering is used to describe this behavior. As the energy crosses a resonance, there is an accompanying rise in the phase shift by π radians. The energy where the total phase shift has risen by $\pi/2$ radians above the phase from interference-term scattering alone is called the central energy E_0.

The first clear experimental evidence of such resonant states appeared in 1959 in inelastic scattering of electrons by helium [6]. The data showed two asymmetric peaks which Fano [7] has attributed to the interference of the continuum with discrete, doubly-excited states. Inclusion of the continuum means that many different configurations can have the same energy, and perturbation theory is inadequate. The configuration interaction, which mixes a configuration of a discrete spectrum with the continuous spectrum, allows the doubly-excited states to "autoionize". The inner and outer electrons may exchange energy, resulting in escape of the more weakly-bound electron. Fano presented a functional form which describes the resonance profile (cross section vs energy) in terms of five parameters: the central energy E_0, the width Γ, an asymmetry parameter q, and two parameters describing the background, σ_b and σ_a. Here we develop his expression for the cross section near a resonance by considering

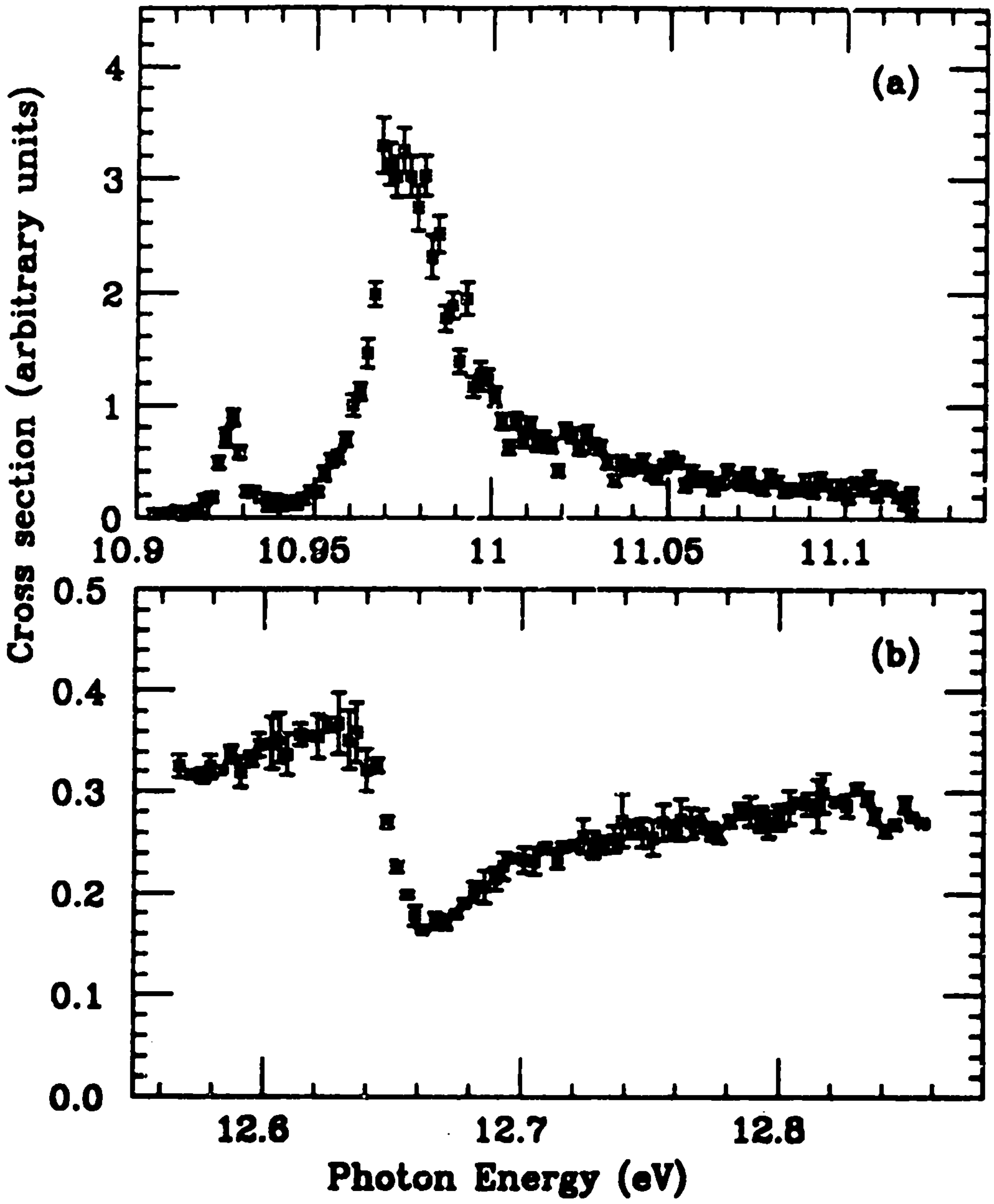

Figure 1.1: Resonance asymmetries vary. (a) $H^{-**}(2)$ Feshbach and shape resonances. (b) $H^{-**}(3)$ Feshbach resonance. (c) $H^{-**}(6)$ Feshbach resonances.

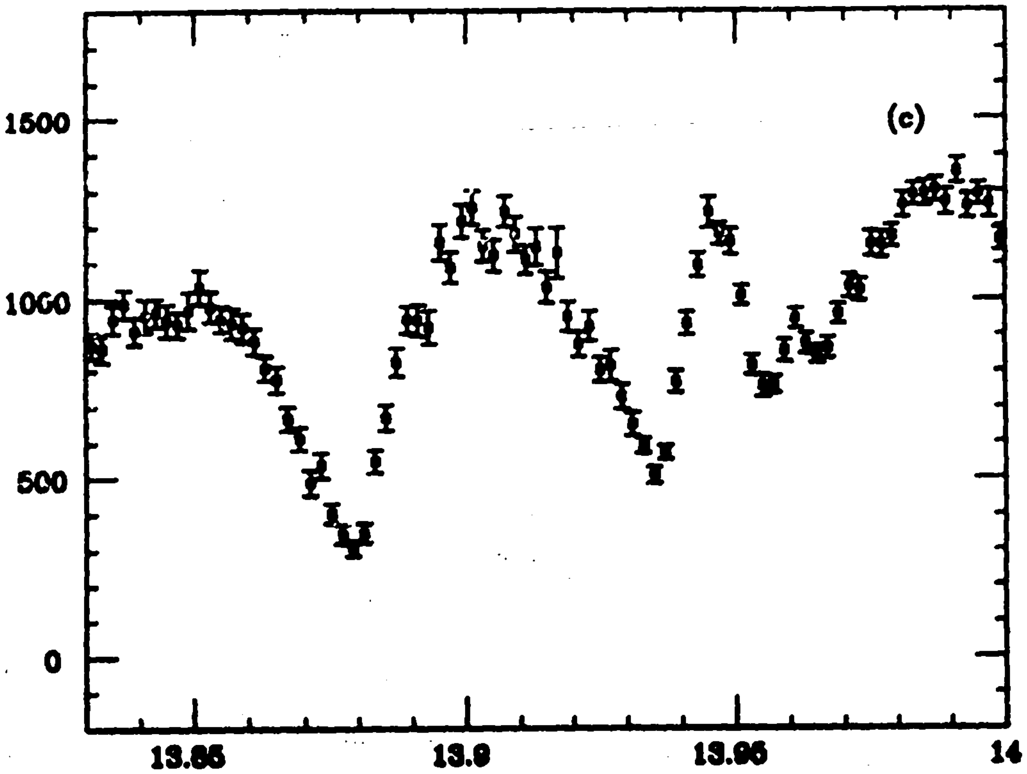
(c)
1500
1000
500
0
13.85
13.9
13.95
14

the time dependence of the amplitude of a decaying state,

$$\Psi_R(t) = A(r)e^{i\omega_o t}e^{-t/2\tau}\ , \tag{1.1}$$

where τ is the mean lifetime. Its amplitude in the frequency (energy) domain is

$$\Psi_R(\omega) = \int \Psi(t)e^{-i\omega t}dt = A\left[(\omega - \omega_o) + \frac{i}{2\tau}\right]^{-1} \tag{1.2}$$

or

$$\Psi_R(E) = A\left[(E - E_o) + \frac{\Gamma}{2}\right]^{-1} \tag{1.3}$$

where $E = \hbar\omega, \Gamma = \hbar/\tau$. Then

$$\Psi_R^*\Psi_R = A^2\left[(E - E_o)^2 + \frac{\Gamma^2}{4}\right]^{-1}\ , \tag{1.4}$$

a Lorentz-type profile. What happens if this resonance is embedded in a continuum? Say the amplitude of the continuum is $\Psi_C = B\ exp(i\phi)$. Then the intensity is

$$\Psi^*\Psi = (\Psi_R + \Psi_C)^*(\Psi_R + \Psi_C) \tag{1.5}$$

After much algebra this leads to the Beutler-Fano profile or "Fano function"

$$\sigma(\epsilon) = \sigma_b + \sigma_a\frac{(q + \epsilon)^2}{1 + \epsilon^2} \tag{1.6}$$

with $\epsilon = 2(\mathrm{E}-\mathrm{E}_0)/\Gamma$. The parameters σ_a, σ_b, and q are related in a complicated way to A, B, and ϕ.

In 1962 resonance structure appeared below the n=2 excitation threshold in close-coupling calculations of Burke and Schey [8] for electron-hydrogen scattering. The close-coupling method is briefly described in Chapter 2. In 1963 Madden and Codling [9] used the 180 MeV electron synchrotron at the National Bureau of Standards to photoionize helium. Many different photon energies were available, as the synchrotron has a range of wavelengths from the infrared down to 100 Å. A beautiful Rydberg sequence of eight ^1P resonances was observed converging to the $He^+(n=2)$ threshold.

Cooper, Fano, and Prats [10], in the same issue of Physical Review Letters as Madden and Codling's report, interpreted these resonances as belonging to the '+' series of

$$\Psi(2n\pm) = \frac{1}{\sqrt{2}}[U(2snp) \pm U(2pns)] \tag{1.7}$$

with n=2, 3, 4, ... That is, there are two symmetrized independent electron wavefunctions (U) that could describe the lowest double excitations. These authors proposed that they combined to give two series: '+' and '–'. One can picture the electrons as two balls or pendulums bouncing on opposite sides of a wall. The wall in our case is the infinitely massive proton. In the '+' mode, the balls approach the wall and bounce off simultaneously, oscillating in phase with each other (Figure 1.2). This is analogous to the electrons in the real atom simultaneously overlapping the same orbital. In the '–' mode, one approaches the wall while the other moves away, so the oscillation is out of phase. In both modes, the electrons are correlated, but more strongly in the '+' mode. Conceptually, this seems logical because the electrons come closer to each other, so the Coulomb force is stronger. For this reason, autodetachment from '–' states is quasiforbidden. They are more stable because the weaker long-range dipole potential produced by the polarized 'core' hydrogen atom controls the action.

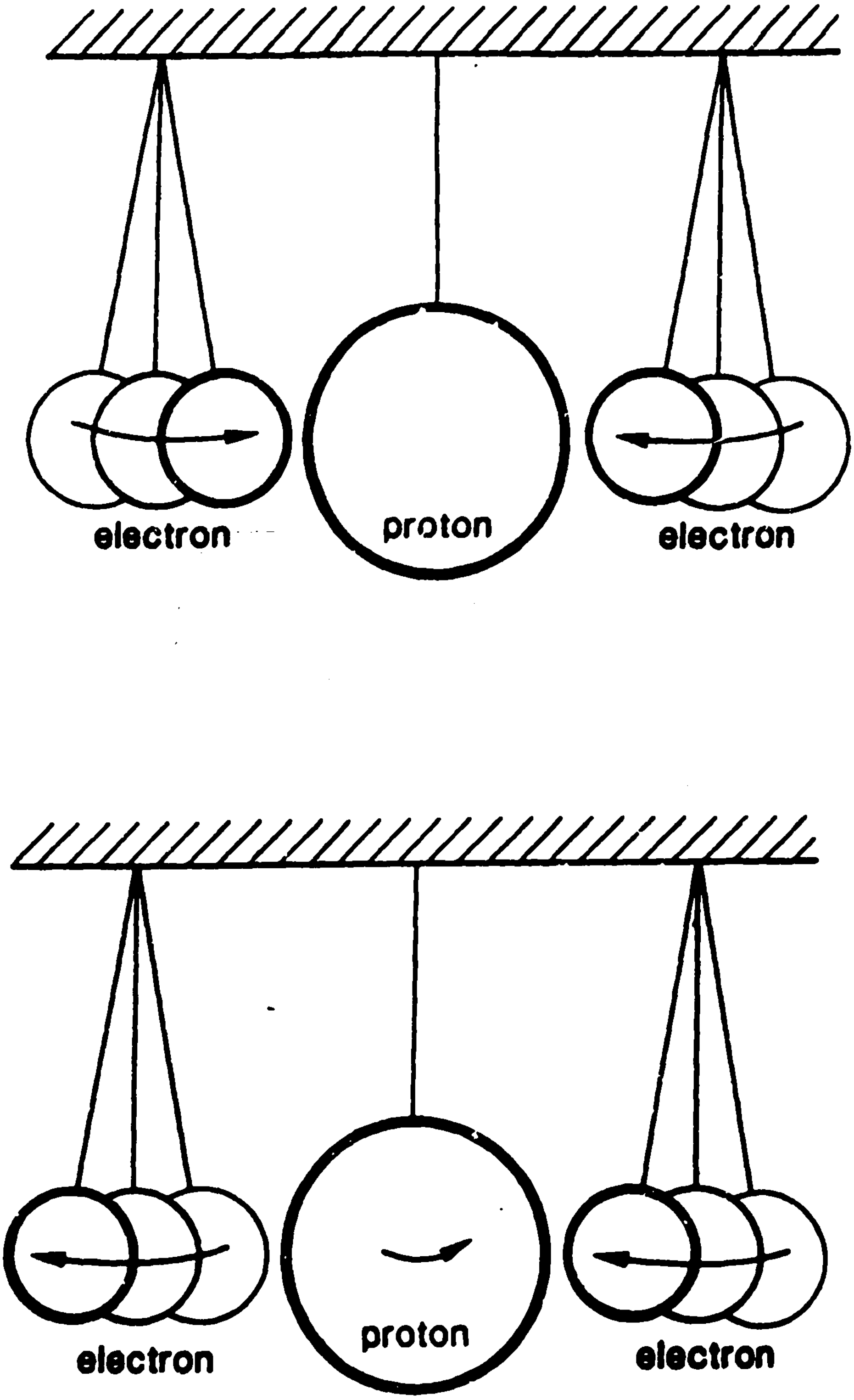

Figure 1.2: Heuristic idea of '+' and '–' states of H^-. Top picture is the '+' mode. Bottom picture is the '–' mode.

1.1.1 Two Very Different Types of Resonance: Feshbach and Shape

An explanation of the autoionizing or "quasibound" states may be adopted from Bohr's suggestion regarding observed nuclear resonances [11]. The idea is that a projectile such as an electron on a hydrogen target can transfer most of its energy to the proton and other electron, so that it cannot escape again until a fluctuation causes energy to be transferred back to it. The concept is the same for photoexcitation—a "half-scattering" process. Thus a doubly-excited state may be formed resembling an excited hydrogen atom with an extra electron also occupying an excited state. Because Herman Feshbach developed the quantum mechanical description of this phenomenon [12], these temporarily bound states are now called "Feshbach" resonances. Also known as "closed channel" resonances [13], they converge from below on each photodetachment threshold for production of H(n) for $n = 2 \rightarrow \infty$. Within each series the states become longer-lived as they approach the threshold. Feshbach resonances which approach the H(n) threshold are classified as $H^{-**}(n)$ resonances. They decay by autoionization to a fragment hydrogen atom plus an electron. The hydrogen atom may have principal quantum number ranging from 1 to n-1 for the resonances discussed here. In this text the principal quantum number of the fragment H atom is denoted by "N".

Resonances appearing above a threshold, but near to and associated with it, are labeled "shape" resonances, referring to the shape of the potential well in which they are temporarily bound. The potential is a combination of dipole and barrier potentials. In the H^- spectrum, only one ${}^1P^o$ shape resonance has been observed, that just above the $H(n = 2)$ threshold. R-matrix theory [1] has predicted another just above the $H(4)$ threshold; some evidence of this is presented in Section 7.3. According to Taylor [14], as ℓ increases, the states should become broader, and cease to exist when ℓ is high enough to effect centrifugal dissociation—when the potential is completely repulsive.

1.1.2 Convenient Coordinate Representations

The correlated behavior depends only on the relative lengths of the radii, $\vec{r}_1$ and $\vec{r}_2$, and the angle between them [15]. Thus, the correlations are invariant under rotations or scale changes. Hyperspherical coordinates seem to offer an appropriate representation for this situation, allowing the segregation of one coordinate, R, which represents the size of the system. The evolution of correlations can be followed as R increases. For a more complete description of the coordinates, consult Appendix B.

The Schrödinger equation in hyperspherical coordinates incorporates what is called a "grand angular momentum" Λ (Appendix B, Eqn. $A1.5$), which accounts for the pairwise structure of the total potential. It is the orbital angular momentum of a single particle in six-dimensional space, and is analogous to the usual orbital angular momentum ℓ of a particle in three dimensions.

The Schrödinger equation becomes separable if channel couplings are neglected in the adiabatic approximation, where the motion in R is assumed to be much slower than the motion in the angles. This is reasonable because for small R the centrifugal term dominates over the potential term. Tunneling becomes unfavorable in this scenario. Adiabatic "channel" functions Φ_μ and eigenpotentials $U_\mu(\mathrm{R})$ are obtained by integrating Schrödinger's equation with respect to the five hyperangles, but keeping R as a slowly varying parameter. Figure 1.3 displays all $^1P^o$ adiabatic hyperspherical potential curves converging to H(n=3 → 7). Weak couplings are neglected in order to make the equation separable, resulting in diabatic potentials. (See Appendix B.) The dominant $^1P^o$ potential curves for H^-(n=2 to 11) are shown in Figure 1.4. Only the lowest '+' channels within each n manifold are plotted along with the level positions in each potential [16].

Another less standard coordinate basis which obtains quasiseparability of the Schrödinger equation in an adiabatic approximation is the prolate spheroidal coordinate system. It also is useful for describing symmetries of doubly excited states, and is preferred by some because it reflects the nodal structure of the states. This is desirable because it has been found that interactions among hyperspherical coordinate channels with similar angular and radial nodal structure tend to dominate [17]. A description of prolate spheroidal coordinates is given in Appendix C.

Calculations of the magnitudes of channel couplings have demonstrated the soundness of the adiabatic approximation. An analysis of weak couplings between different adiabatic channels has shown that the lowest '+' channel in each hydrogenic series wields the controlling influence on the H^- resonant spectrum [16].

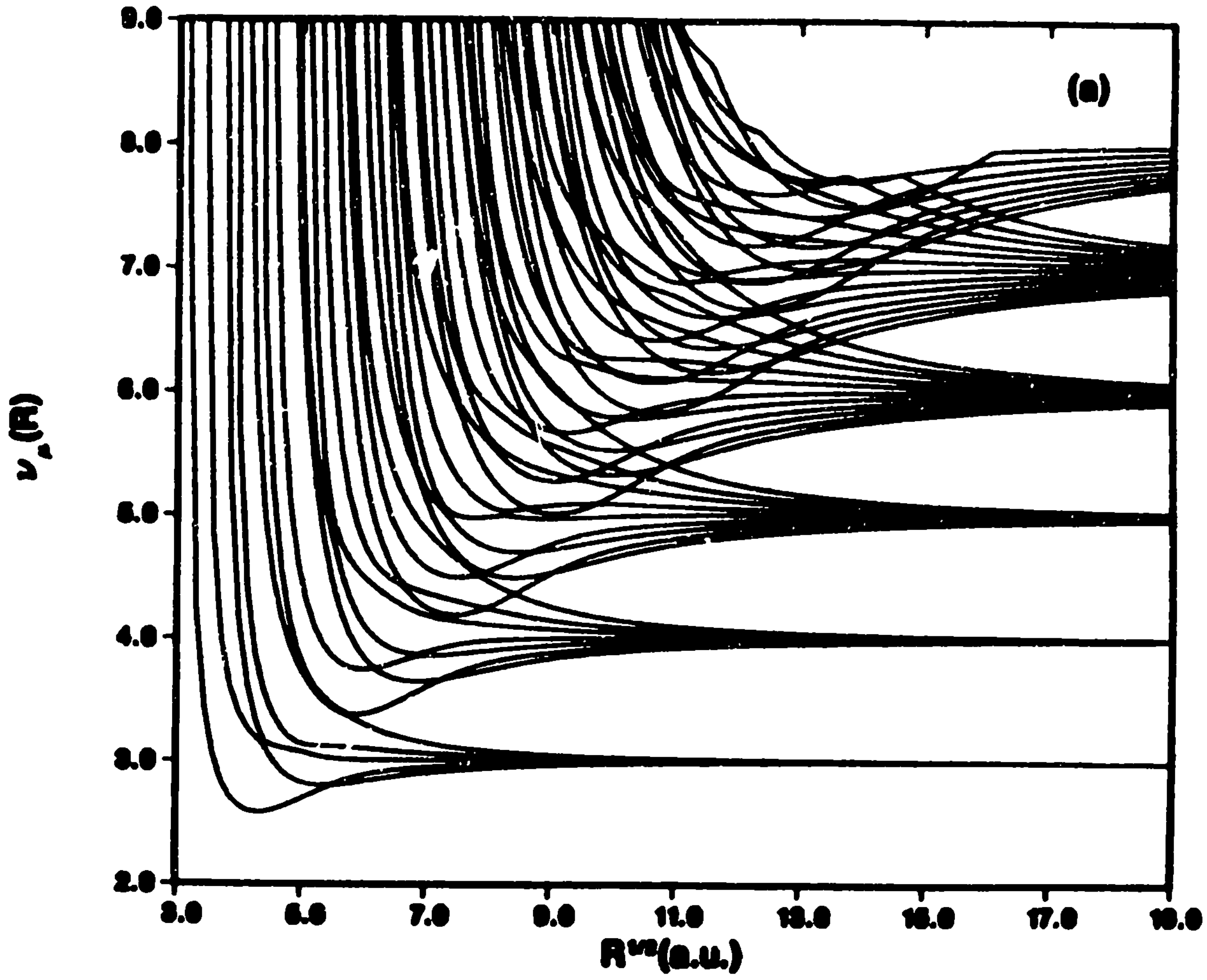

Figure 1.3: $^1P^o$ adiabatic hyperspherical potential curves converging to H($n=3 \rightarrow 7$).

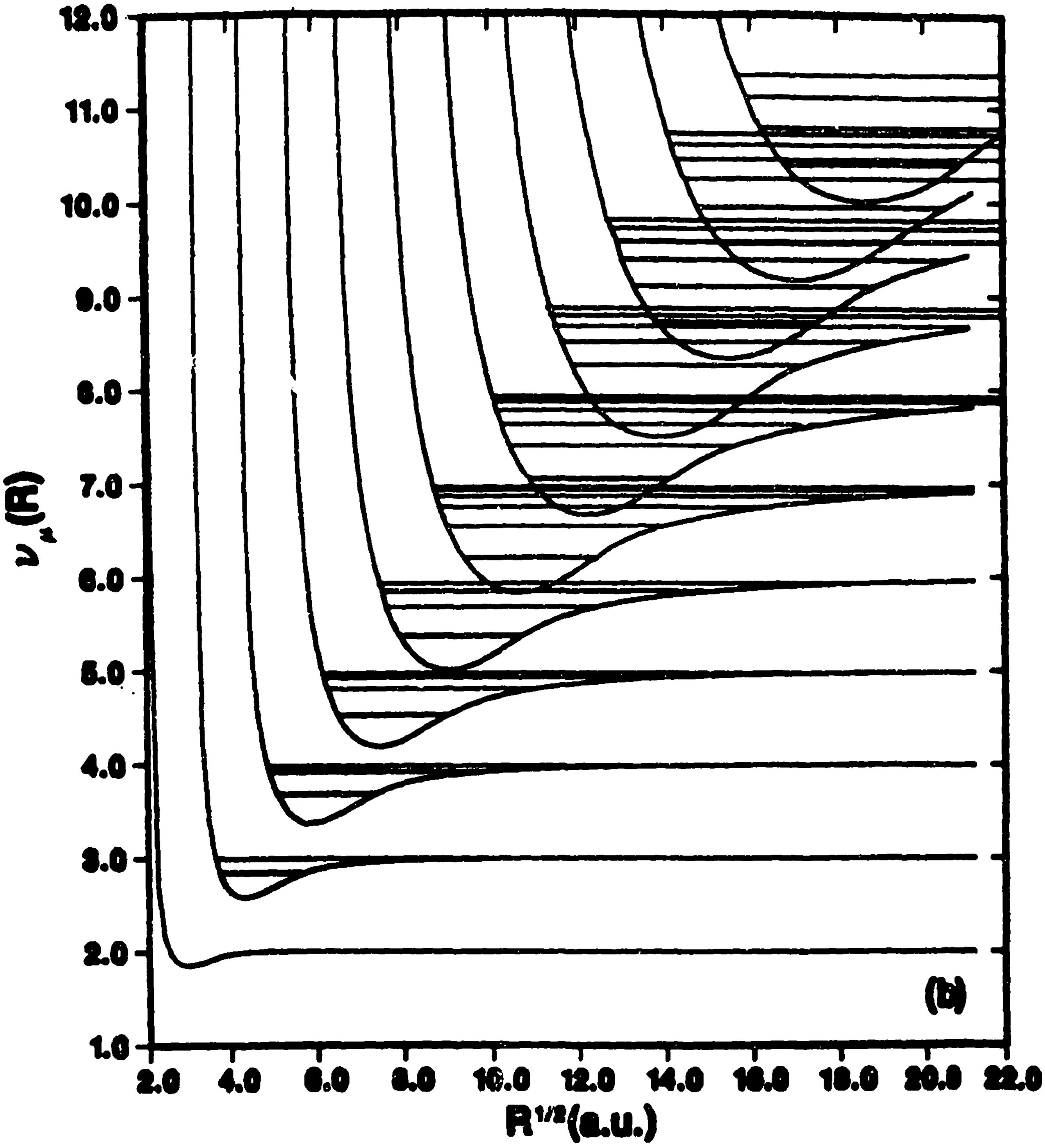

Figure 1.3: Dominant diabatic potential curves for ${}^1P^o$ H^- shown as effective quantum number vs $\sqrt{R}$.

1.2 H^- Resonances Observed in the Total Cross Section

The practicality of the hyperspherical coordinate treatment manifests itself in numerous very accurate theoretical predictions of these resonant states. The large H^- shape resonance lying just above the H(N=2) threshold was first predicted in 1967 by Taylor and Burke [18] for electron-hydrogen scattering, and by Macek [19] for photoionization of H^-. Subsequent total cross section measurements (that is, measurements where the trigger is from any fragment H atom, without regard to its N-value) confirmed its existence [20, 21, 22], as well as that of the narrow Feshbach resonance lying below threshold [23]. See Figure 1.1(a).

These rather spectacular successes led to the search for doubly-excited states near higher thresholds. The Doppler-shift method used at LAMPF (described in section 3.2) was uniquely qualified for this effort, and two resonances were soon observed below the H(3) production threshold [24]. See Figure 1.1(b). Energies and widths of the $H^{-**}(3)$ states were in good agreement with theory, and displayed interesting asymmetry as compared with the n=2 resonances. The profiles appeared as peaks blending into dips in the detachment cross section, indicating a seeming unwillingness of the state to part with electrons at energies in a small range above the central energy position. A result of interference by the continuum of free electrons, it is accounted for in theories by the introduction of an additional phase shift, as mentioned in section 1.1. Higher autoionizing states have been observed only in partial cross section measurements, where the experimental signal is from fragment H atoms in a specific excited state.

1.3 Observations of Partial Decay of Autoionizing States

A partial cross section is the probability for a photon to detach an electron from H^-, and leave the fragment hydrogen atom in a particular N-state. (Our detector design did not allow for discrimination among different angular momentum states.) By "partial decay" I mean the tendency of a doubly-excited resonance to decompose into a particular N-state of neutral hydrogen and a free electron.

In 1983 the first photodetachment partial cross section of an H^- resonance was measured at LAMPF [25]. In that experiment H^- was photoexcited to $H^{-**}(2)$. The decay to neutral hydrogen in its first excited state, H(2), was monitored via laser excitation of H(2) to H(7) with subsequent field-stripping of the H(7)s. The resulting protons were detected in a scintillation counter. The background was not well understood, so the partial cross section data were not compared with theory at that time, but that has been rectified in this thesis. We repeated the experiment in 1990, using a different detection scheme (Chapter 3.1). During the same LAMPF run cycle, we measured partial cross sections for $H^{-**}(n) \rightarrow H(2) + e^-$ with $=2$, 3, and 4. The details of this experiment comprise the bulk of this thesis.

Harris *et al* [26] also made partial decay measurements with and without applied electric fields in 1989. The cross sections, however, were measured for energies greater than the H(N=4) production threshold, for which theoretical partial cross sections are unavailable because of computational convergence problems. Observed resonance lineshapes were consistent with the Fano function, and central energies were found to obey a recently developed two-electron formula [27]. A rigorous analysis of the electric field effects and zero-field threshold regions—not performed at the time of the original experiment—has been carried out by this author, and the results are presented in Chapter 7 as a supplement to the more recent zero-field data acquired in 1990.

1.4 Threshold Behavior

Threshold behavior is discussed in a different context from the behavior of resonant cross sections. (See Section 2.3.1.) The observations recorded here, covering the thresholds for production of H(N)—where N=2, 4, 5, and 6—from photoexcitation and detachment of H^-, are the first of their kind. They show that the cross section near the N=1 threshold is much different from that near the N=2 threshold, which in turn differs greatly from the higher thresholds. In addition, when an electric field is applied to the interaction region, the cross sections near the higher-N thresholds show interesting structure, which has instigated recent theoretical activity [28].

1.5 Physical Motivation for Measurement of Partial Cross Sections

According to several theoretical studies [29, 30, 31, 32], the doubly excited states $H^{-**}(n)$ with $n < 9$ are expected to prefer a transition into the nearest lower H(N) level (i.e. $N=n-1$), but there had been no experimental verification before this work. Our first intention was to test the theory by measuring branching ratios for transitions into all available H(N) levels. Accelerator operational problems cut short our allotted beam time however, and in 1990 we were able to measure only the $H^{-**}(n)$ resonances decaying into H(N=2) for n=2, 3, and 4. Fortunately, these did provide us with some preferred channel information [33], as shown in Chapter 7.

Theory was not the stimulus for the experimental work done on high-lying resonances in static electric fields. No predictions were available before the experiment, but the results have already spurred new theoretical work. Unexpected threshold shifts, threshold structure, and the appearance of at least one new resonance (described below) in the presence of fields less than 100 kV/cm demonstrate that there is still much to learn about the H^- ion and its internal correlations. In applied fields, the threshold regions are extremely rich in structure that is not yet completely understood, but is probably related to field-assisted tunneling of the zero-field resonances, a process which has never before been monitored. This process could allow Feshbach resonances to decay to their parent state, effectively modifying the branching ratios. It is hoped that the results presented here will stimulate further theoretical work to assist in their interpretation, and to suggest future experiments.

Chapter 2

Theory of Partial Decay

2.1 Shape Resonance Partial Decay in Zero Field

The autoionizing $n=2$ shape resonance is the largest resonance in the H^- photodetachment spectrum and a key feature in understanding electron correlations. Unique in that its potential has three classical turning points, it is well-known as the only resonance of its type yet observed in the H^- photodetachment spectrum (or equivalently in electron-impact excitation of H atoms). The shape resonance results from a centrifugal barrier potential, and appears above the threshold for excitation of the H(N=2) state. It can therefore autodetach to either the H(2) or H(1) continuum. Its slightly-lower-lying neighbor—the ^1P $n=2$ Feshbach resonance at 10.9264 eV [5]—is energetically capable of decay only to the ground state of neutral hydrogen, the N=1 channel. Since the shape resonance is the only H^- resonance which has been observed to decay to its parent state, the measurement of its branching ratio, which demonstrates the substantial effects of electron correlation, confirms the important dynamical differences between shape and Feshbach-type states. Details of the parameters such as widths and asymmetries (Sec. V) may be especially useful in current theoretical studies of static electric field effects on the shape resonance.

Macek's 1967 work [19] on the photoionization of H^- provided partial cross section as well as total cross section predictions for the shape resonance. His three-state close-coupling calculations did not include correlations, however, making his predicted width about five times too large, but the central energy at 11.00 eV turned out to be fairly close to the eventually measured value of 10.975 eV [34].

In 1972 Hyman *et al* [35] computed the cross sections for the $H^{-**}(2)$ shape resonance to evolve to either $H(2s) + e^-$ or $H(2p) + e^-$, using Hyleraas bound state wave functions in a $1s$-$2s$-$2p$ close-coupling calculation. In this, as in all H^- approximation methods, the proton is assumed to carry infinite mass, so the wave function is solely dependent on the electrons' coordinates. In close-coupling all neutral hydrogen eigenstates corresponding to the level under study, as well as continuum states, are included in the expansion of the wave function, and the integration is performed numerically. Like Macek, these authors predicted a width that was quite large compared to the experimental result.

A more detailed theory using multichannel J-matrix calculations was prepared by Broad and Reinhardt [36] in 1976. Their method solves the pseudostate many-channel close-coupling equations for H^- photodetachment using standard configuration interaction methods and square integrable (L^2) basis functions. In this formulation, the one-electron photodetachment cross section is

$$\sigma_{vel}(E) = \frac{4\pi^2}{\omega c} \left|\left\langle {}^{\Gamma}\Theta_{-}(E)|\nabla|\Phi_{gnd}\right\rangle\right|^2 \tag{2.1}$$

in the dipole velocity form, or

$$\sigma_{length}(E) = \frac{4\pi^2\omega}{c} \left|\left\langle {}^{\Gamma}\Theta_{-}(E)|\ r\ |\Phi_{gnd}\right\rangle\right|^2 \tag{2.2}$$

in the length form. The derivation using the length form of the dipole moment has generally been considered to be more accurate for the H^- case because the wave function is most accurate at large values of r. This region is more heavily weighted in the length form than in the velocity form [37]. In (2.1) and (2.2) ${}^{\Gamma}\Theta_{-}(E)$ is the incoming scattering wave function and Φ_{gnd} is the ${}^1S$ ground state calculated using configuration interaction technique. Our data is compared with σ_{length} for the n=2 resonances in Chapter 7.

The bound-free photodetachment σ_{length} near the N=2 threshold was also calculated by Wishart [37] in 1979. The wavefunctions were found using close-coupling expansion plus Hyleraas-type correlation terms. The method differs from that of reference [35] mainly through its inclusion of these correlations, which are assumed to depend explicitly on r_{12}. The correlation coefficients were determined variationally. The shape resonance profile from this calculation does not match the experimental data as closely as profiles from other theories.

In 1982 Callaway published a close-coupling–variational study of the scattering of electrons by hydrogen atoms at energies near the shape resonance. The results were not useful for comparison with our photodetachment data because, in electron scattering, many final angular momentum states are allowed, whereas in our case, according to electric-dipole selection rules, the final state is always ${}^{2S+1}L^{\pi} = {}^{1}\mathrm{P}^{o}$, where π is the parity and S is the total spin. Callaway's method, however, was capable of providing the ${}^{1}\mathrm{P}$ partial cross sections for $1s$–$2s$ and $1s$–$2p$ excitation, and he supplied these unpublished results to us in February 1992 (included in Appendix I). The energy dependence of his profiles agrees well with our measurements.

In 1991 Liu *et al* [38] published one- and two-photon detachment cross sections for the shape resonance to decay to the $2s$ or $2p$ states of neutral hydrogen with emission of an electron. These were calculated within an adiabatic hyperspherical representation, but diabatic potentials replaced adiabatic near the sharply avoided crossing of the ${}^{1}\mathrm{P}$ '+' and '–' curves. (See Appendix B for further description of diabatic and adiabatic potentials.) As seems to be the case for most hyperspherical coordinate treatments of the shape resonance, the predicted central energy is about 20 meV too high, and the width is somewhat exaggerated.

2.2 Partial Decay of n=3 and 4 Resonances

It wasn't until 1990 that the implementation of R-matrix theory was sufficiently advanced to be able to supply cross sections for decay of the higher-lying resonances (n=2, 3, 4) into different fragmentation channels. The R-matrix approach represents a simplification over the standard reaction-matrix method in that only interactions within a confined volume are considered when forming a basis set of wavefunctions. The complication of including continuum states is thus obviated. The specified volume has a radius R_0, defined as the reaction box size. This is usually chosen to be larger than the radius at which '+' and '-' channels experience a diabatic crossing, where channel-coupling is most significant. (See Appendix B.) In these *ab initio* calculations, Sadeghpour and coworkers [1] incorporate an analytic description of electron motion in a dipole field with the eigenchannel form of R-matrix theory. Their analysis of the time-delay matrix, which accounts for the delay a particle undergoes upon penetration and reemergence from a potential well, confirms the predominance of fragmentation to the closest energetically-available channel. The advent of these R-matrix predictions coincided with the 1990 data reported here, which measured the relative partial cross sections for $H^{-**}(n=2, 3, \text{ or } 4)$ to autodetach into an electron and a hydrogen atom in its first excited state, H(N=2). The favorable comparison between this theory and the experimental data is encouraging.

Recent work of Chrysos *et al* [39], carried out within the framework of the so-called Wannier two-electron ionization ladder (TEIL), and including interchannel coupling, presents predictions for partial and total widths of the $^1P^o$ H^- resonances for n=3, 4, and 5. The resonance wavefunctions are described as

$$\Psi = \Phi + X_{loc} + X_{as} \,, \tag{2.3}$$

where Φ is the zeroth-order form of the multiconfigurational wavefunction and includes all configurations of $^1P^o$ symmetry for the particular n state, X_{loc} is the localized correlation embodying single- and pair-correlation functions, and X_{as} is the asymptotic part of the wavefunction which includes information from continuum channels and contributes to autoionization. Energies and widths from this theory are comparable to experimental values, but cross sections are not supplied by these authors. Branching ratios are calculated, but we have been unable to verify these, because the allotted beamtime was shortened by circumstances beyond our control. The proclivity for the lowest $H^{-**}(3)$ resonance to decay to H(2) + e, as predicted by Chrysos' group and others, was demonstrated however in the 1990 experiment.

2.3 Partial Cross Sections in Static Electric Fields

Experiments investigating the effects of static electric fields on H^- photodetachment thresholds have been limited to energies near the one-electron detachment threshold at 0.7542 eV [40, 41]. No resonances are known to exist in this region, and field-induced ripples observed in the cross section near threshold have been described in terms of a time-dependent autocorrelation in the outgoing wavefunction. Semiclassical closed-orbit theory [42] and frame transformation methods [43, 44] have also been successfully applied to this problem, but not to the study of the higher thresholds.

Prior to the 1989 experimental studies of high-lying resonances exposed to static electric fields, the only theoretical work in this area was confined to studies of the resonances near the H(N=2) photodetachment threshold [41]. However, the rather surprising results of the 1989 observations (large threshold shifts and unexpected structure development) stimulated theorists to come up with explanations.

2.3.1 Thresholds

Zero-Field Thresholds

According to Gailitis and Damburg [45], when no external electric field is present the amplitude A of a cross section at threshold is given to first order by

$$A \propto k^{\lambda+1/2} \tag{2.4}$$

where λ is the effective angular momentum of the electron pair, $k = \sqrt{2M(E - E_{thr})}$, and M is the reduced mass. The influence of the long-range dipole ($V_D = -a/(2r^2), a < 1/4$) from the excited "core" H atom results in an imaginary exponent, $\lambda + 1/2 = i\nu$, so that the cross section σ at threshold is a constant to first order. Higher-order terms do exist, and should cause oscillations in the cross section immediately above threshold [45]. Greene and Rau, however, show that the modulating factor is modified by $\exp(-\pi\alpha)$ where $\alpha = \sqrt{a - 1/4}$ and a is the dipole moment [46]. They calculated α for the dominant photodetachment channels, and found that the $\exp(-\pi\alpha)$ factor makes the amplitude of the expected oscillations extremely weak—too small to be observable with our current experimental method. See Table 2.1.

Thresholds in Applied Fields

When H^- is photodetached to H(N)+e, in the presence of a field, the energy onset of detachment may decrease by field-lowering of the potential barrier seen by the outer electron. In zero applied field, the departing electron feels the dipole potential V_D of

Table 2.1: **Dipole parameter α relevant to H^- photodetachment accompanied by excitation of $H(n)$ [46].**

n	α (a.u.)	$\exp(-\pi\alpha)$
4	4.2671	$1.5(10^{-6})$
5	6.1191	$4.5(10^{-9})$
6	7.9184	$1.6(10^{-11})$

the degenerate states of the excited H atom it leaves behind.

$$V_D = \frac{-a}{2R^2} \tag{2.5}$$

where

$$a \approx 3n^2 - \frac{23n}{3} + \frac{2}{3n} + 1 \tag{2.6}$$

is the dipole moment for the lowest '+' channel in each manifold (expected to be the dominant channel) [16].

When a field is applied, the outgoing electron also feels the potential from the external field

$$V_F = -eFz \tag{2.7}$$

(See Figure 2.1). The total potential is $V(R) = V_D + V_F$. Letting $z = R$ and setting the derivative with respect to R of $V(R)$ equal to zero obtains

$$V(R)_{max} = -\frac{3}{2}a^{1/3}F^{2/3}. \tag{2.8}$$

If barrier-lowering is the only reason for the threshold shift, we expect Eqn. (2.8) to be the magnitude of the shift. It is shown in Chapter 7 that this is close to

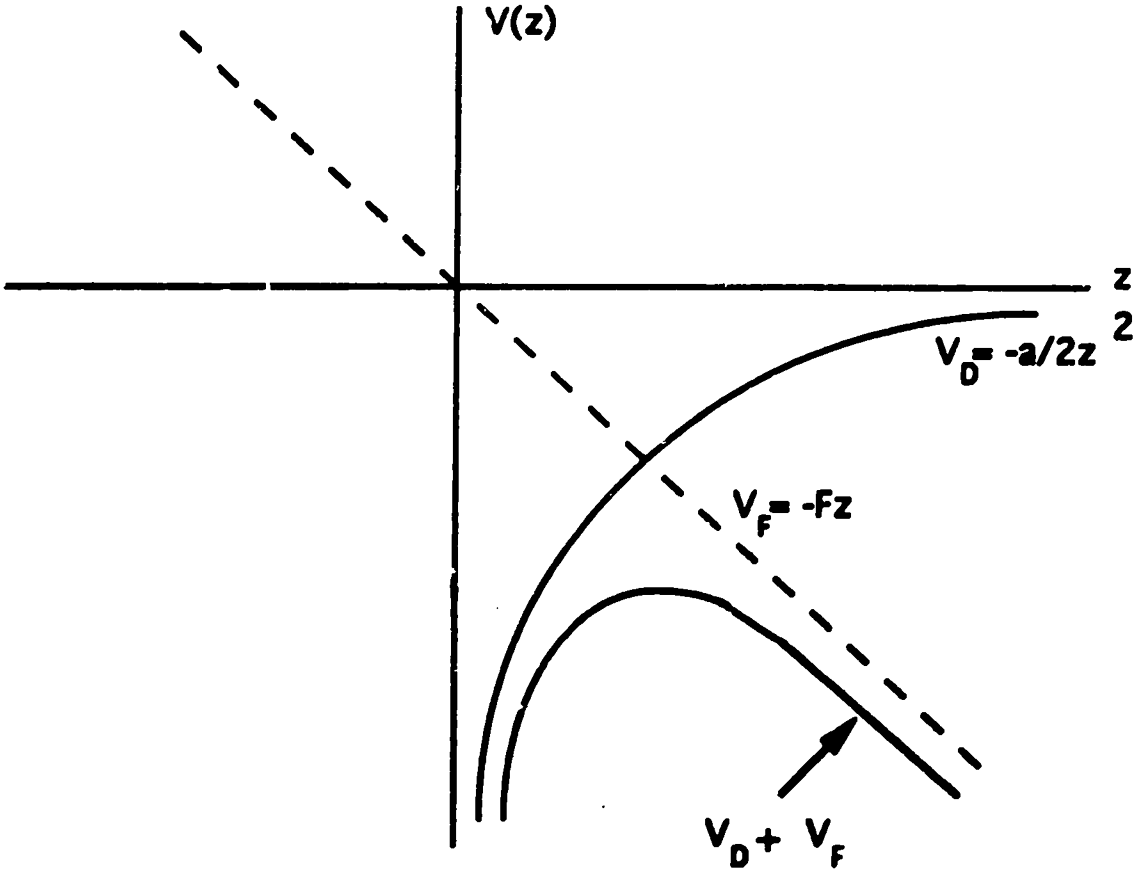

Figure 2.1: Dipole potential barrier lowered by applied-field potential.

the experimental value, but not within error bars.

After examining our data, theorists undertook hyperspherical coordinate calculations in hopes of understanding the discrepancy. Field-deformation of the H$^-$ eigenpotential curves was suspected to be involved.

Hyperspherical coordinate potential curves for the N=4 threshold were calculated by H. R. Sadeghpour [47] for a field of 87 kV/cm, but an interpretation in terms of threshold shift was unrealizable owing to the large number of available channels that can exist in a field.

A similar approach was taken by Bin Zhou and C. D. Lin [28], but only a few presumably dominant channels were included, making for fewer complications in the analysis. See Figure 2.2. In (a) F=0: The two solid lines are diabatic $^1P^o(+)$ (lower line) and $^1P^o(-)$ (upper line) potentials; the two dashed lines are diabatic $^1F^o(+)$ (lower line) and $^1F^o(-)$ (upper line) potentials; the dotted lines, from the bottom, are $^1S^e$, $^1D^e$, $^1G^e$, and $^1H^o(+)$ potentials. In (b) F=87 kV/cm: the dotted curves are adiabatic potentials; the lower [upper] solid line is the diabatic curve which converges to the zero-field $^1P^o(+)$ [$^1P^o(-)$] potential at small R.

These theoretical investigations show that a weak residual coupling between the $^1P^o$ '+' and '–' channels allows the states associated with the '+' channel to decay through the '–' channel. The effect is to shift the threshold downward by an amount comparable to the measured value. The comparison may be seen in Chapter 7.

When a field is present the '+' and '–' channels no longer converge to the same asymptotic ($R \rightarrow \infty$) limit. Figure 2.3 shows that for the case of H(4) production,

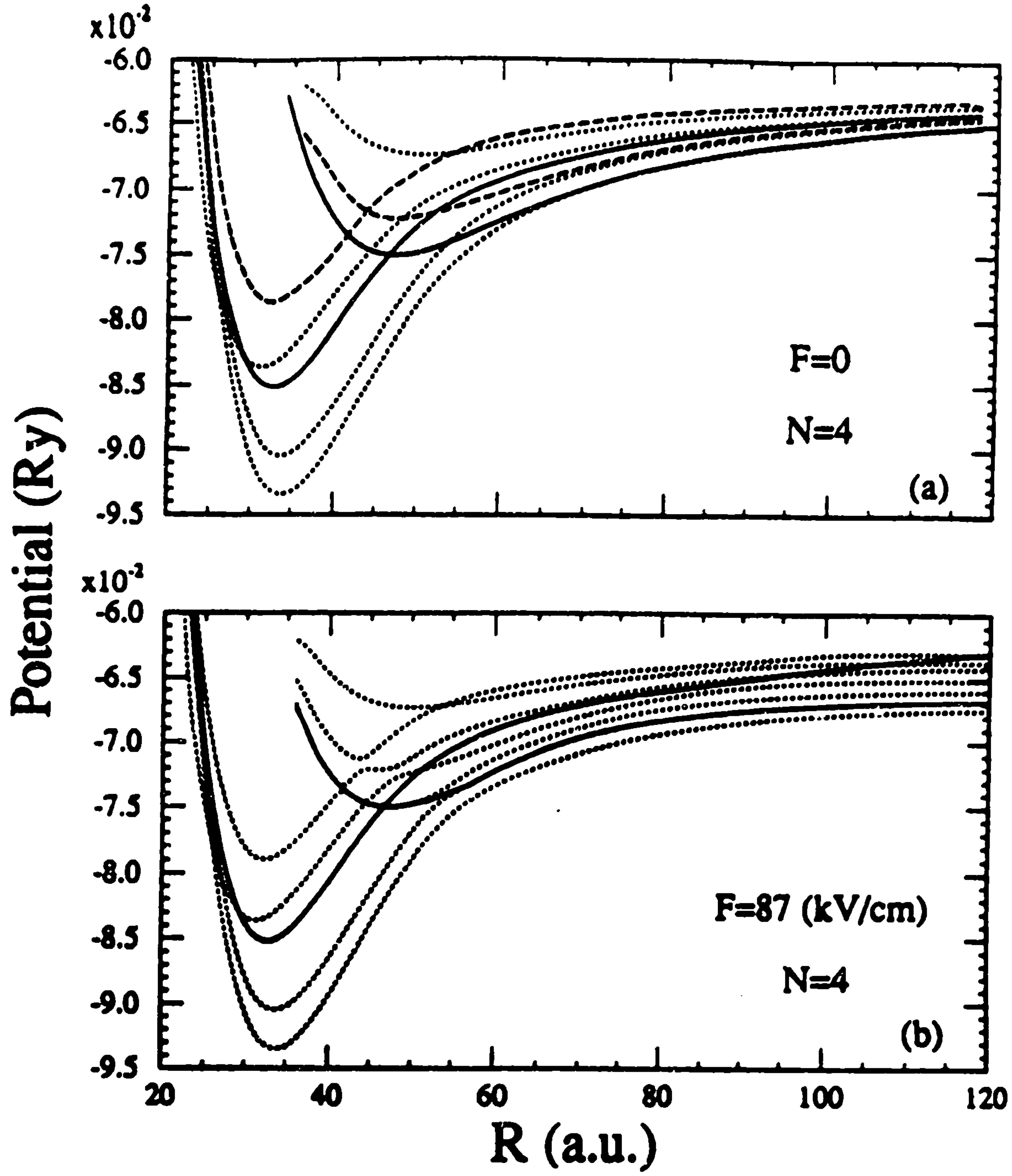

Figure 2.2: Hyperspherical potential as a function of R for the N=4 manifold [28]. (a) F=0 kV/cm. (b) F=87 kV/cm. Curves are described in the text.

the '–' curve is lowered in a field F=87 kV/cm while the '+' curve is raised. The arrow indicates the position of the zero-field threshold. The energy positions of the three lowest resonance states in the ${}^1P^o(+)$ potential at F=87 kV/cm are shown by the horizontal bars. The channel coupling—most significant near the crossing point at abour R=45 au—allows the outer electron in the '+' state populated by photoabsorption to excape or tunnel through the potential barrier of the '–' channel. The new detachment threshold is thus determined by the barrier height of the '–' curve, rather than the '+' curve [28]. This explains why the 'a' value of Equation 2.6 does not give the correct result.

As the thresholds shift downwards from their zero-field positions, structures (peaks, dips, steps) are observed in the shifted-threshold region. This structure may be partly attributable to field-assisted tunneling of H^{-**}(n) doubly-excited autodetaching resonances which converge from below to each H(n) threshold. (A detailed description of these states can be found in in reference [26].) In zero-field these can be observed only in the H(N$\leq n-1$) continuum [48] because the inner electron must exchange energy with the outer electron if autodetachment is to occur. As suggested by Lin [49], however, the field may supply the outer electron with enough energy to allow autodetachment without affecting the principal quantum number of the inner electron. It would therefore remain in the n level, and the resonance would be observable in the H(n) channel. The following order-of-magnitude calculation shows that fields used in this experiment are of sufficient strength for this process to occur.

Consider for example the H^{-**}(5) state with n=5 and m=7 below the H(5)

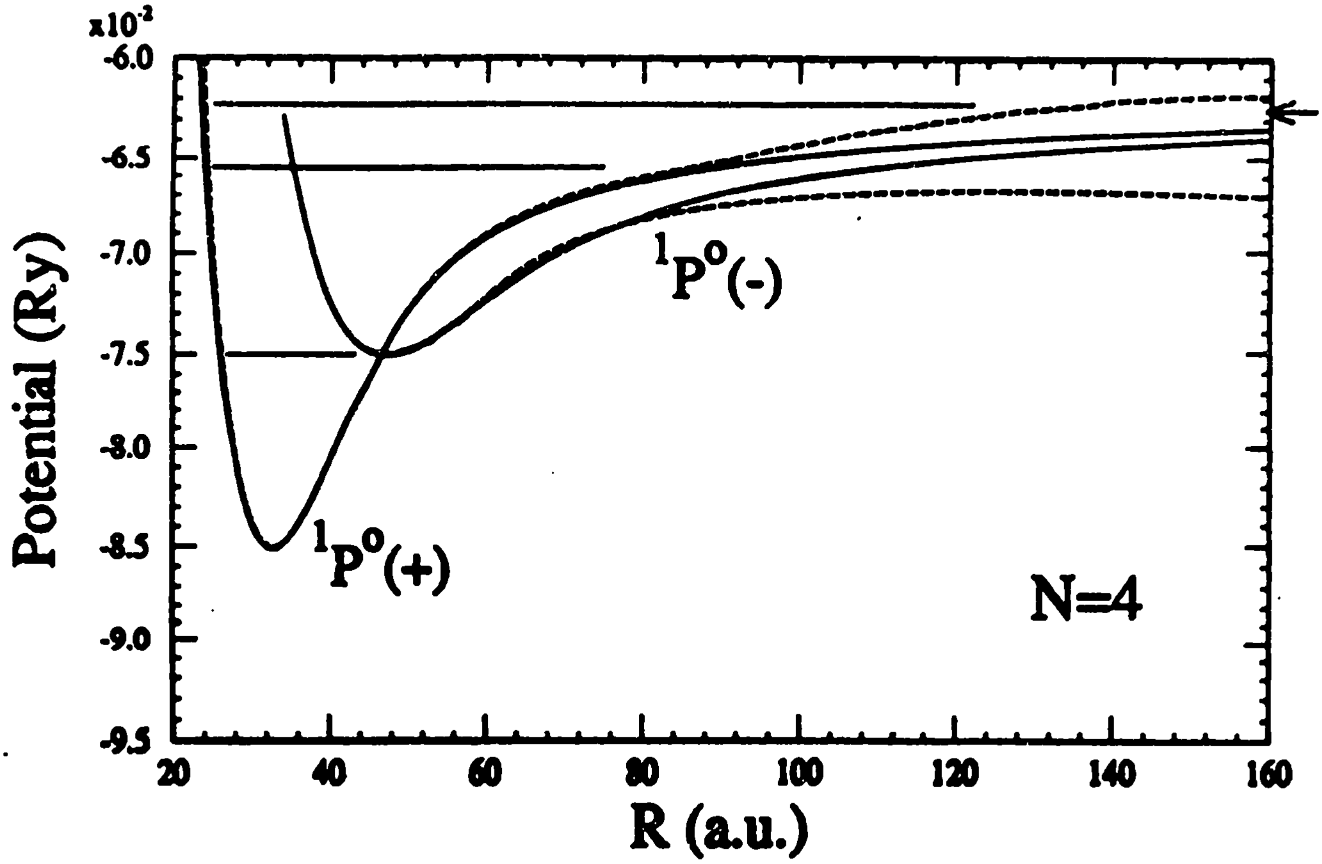

Figure 2.3: $^1P^o$ diabatic potentials in F=0 (solid lines) and F=87 kV/cm (dashed line) for the N=4 manifold. [28]

threshold. The distance from the inner (outer) electron to the proton is d (s). Take $d = 5^2 a_o$ (typical H(5) atom) and $s = 77$ a.u. (from hyperspherical calculations of Sadeghpour). The field seen by the outer electron is the dipole field of the "core" hydrogen atom

$$F = \frac{ed}{(s + d/2)^3} \approx 30 \ \frac{\text{kV}}{\text{cm}}. \tag{2.9}$$

So an external field $\gtrsim 30$ kV/cm should be able to strip the outer electron, making the resonance observable in the H(5) channel.

More detailed calculations of Zhou and Lin explain this behavior in terms of the changing shape of the potential curves in a field [28]. While it is also true that ℓ=0 and 2 states may be mixed in by the field, these were not included in the calculations, but those which should appear above the shifted thresholds are probably too narrow to be resolved anyway [50, 51].

2.3.2 Resonances in Applied Fields

The same theoretical investigation [28] offers an explanation of the change in the H(N=4) cross section appearing in a field of 87 kV/cm, where a dip which is not seen in lower field strengths develops near 13.51 eV. It is suggested that a '+' potential, which supports a Feshbach-type resonance in zero-field, can develop into a centrifugal barrier when a field is applied, giving rise to a shape resonance *above* the zero-field threshold. The dip is interpreted as the third lowest resonance associated with the $^1P^o$ '+' potential curve converging to the H(4) threshold. Cross section calculations prove too computer-intensive, but the field-shifted energy of this state (13.511 eV) calculated by Zhou and Lin using the WKB approximation compares favorably with the central energy of the observed dip. (See Chapter 7).

Although no rigorous theoretical work has been done on the effect of fields on states for $n > 2$, qualitative statements may be made on the subject. The zero-field $H^{-**}(n)$ states—here observed in the $H(n-1)$ channel—should decrease in amplitude when a field is applied, simply because the outer electron can tunnel through the lowered barrier. Since the higher-lying states in each resonant series are more loosely-bound, they should deplete and disappear in smaller field strengths than the ones that lie lower in energy.

Resonances which do not completely "disappear" should become asymmetric in fields strong enough to cause visible mixing of the $^1P^o$ states with even parity states, such as $^1D^e$ and $^1S^e$. Spectral repulsion is also expected, wherein the Stark states may move away from each other. A shift in the central energy may be taken as evidence of this behavior.

Using R-matrix methods, Greene and Slonim [52] have predicted that the width of the H^- shape resonance should change with field strength in an oscillatory manner (See Appendix J). Feshbach resonances are expected to exhibit the same type of width-oscillation. This aspect, as well as quenching and asymmetry of high-lying resonances, has been examined and reported in Chapter 7.

Chapter 3

Experimental Method

3.1 The LAMPF H^- Beam

The LAMPF external beam has been used for the study of H^- physics since the early 1970's. The highest energy negative hydrogen beam in the world at the time of this writing, it offers unique opportunities to study high-lying structures in the H^- photodetachment spectrum, as discussed in Section 3.2.

The H^- ions are produced in an optically-pumped polarized ion source (OPPIS). A schematic diagram is shown in Figure 3.1. Protons from an electron-cyclotron-resonance source pick up spin-polarized electrons from a sodium vapor which is optically pumped by titanium-doped sapphire (Ti-Saf) lasers. The resulting electron-polarized H atoms then traverse a magnetic-field-reversed region. This stimulates a Sona transition whereby the electron-spin aligned atomic beam is transformed into a proton-spin aligned beam [53]. H^- ions are formed in a second unpolarized sodium vapor chamber, yielding a proton-polarized H^- beam, called P^-. Our experiments

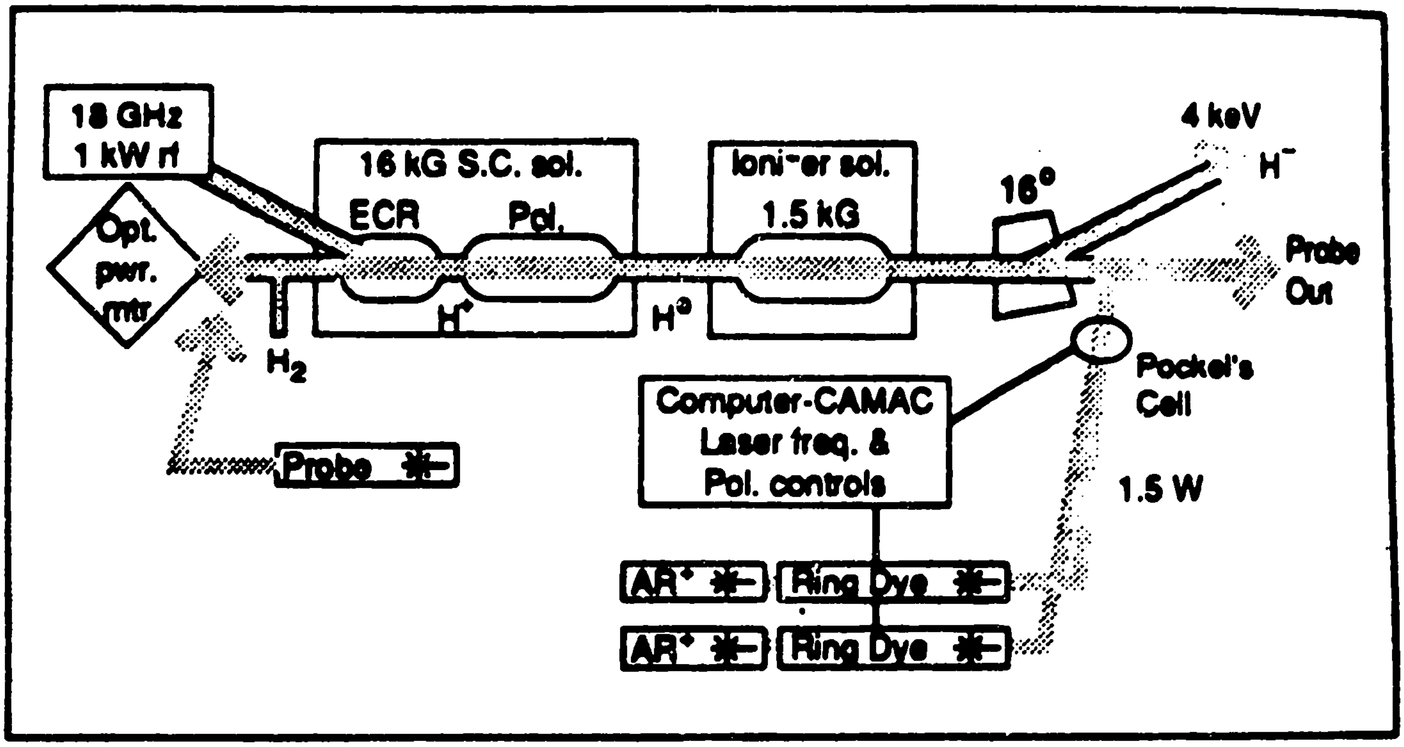

Figure 3.1: Optically-pumped polarized ion source.

are such that the polarization of the proton contributes no discernible effect. We accepted polarized and unpolarized beam in 1990.

From the source the ions are field-accelerated by a Cockcroft-Walton (CW) type accelerator. On exiting the CW columns, they enter a 200 foot drift-tube linac which uses a 201.25 MHz alternating electric field for acceleration. The ions then enter a side-coupled-cavity linac which accelerates them to a very high energy in a relatively short distance as compared with the drift-tube method [54]. The H^- final beam energy achieved in this manner is 8×10^8 electron volts, which means the ions move faster than 4/5 lightspeed.

The negative ion beam is directed towards HIRAB (in Area B) by a pulsed magnet at the beam switchyard (See Figure), and arrives in the experimental area in pulsed form at repetition rates up to 120 pulses per second. These macropulses, normally a few hundred microseconds in duration, themselves have a micro-time-structure comprised of 1/4 nanosecond (ns) pulses spaced anywhere from 5-100 ns apart, depending on the chopping used during a particular run cycle. The duty cycle, or fraction of time that the accelerator delivers particles to the experiment, can thus range from about 1.5×10^{-4} to 5.4×10^{-3}, subject to the macropulse length and micropulse spacing. For the 1990 run, the macropulses were 800 μs long with 100 ns micropulse spacing.

The beam currents used in the experiments discussed here varied from about 100 picoamps to 1 nanoamp. The typical diameter of the beam spot on arrival in our experimental area is 2 ± 1 mm, measured using a fluorescent screen (See section 3.6).

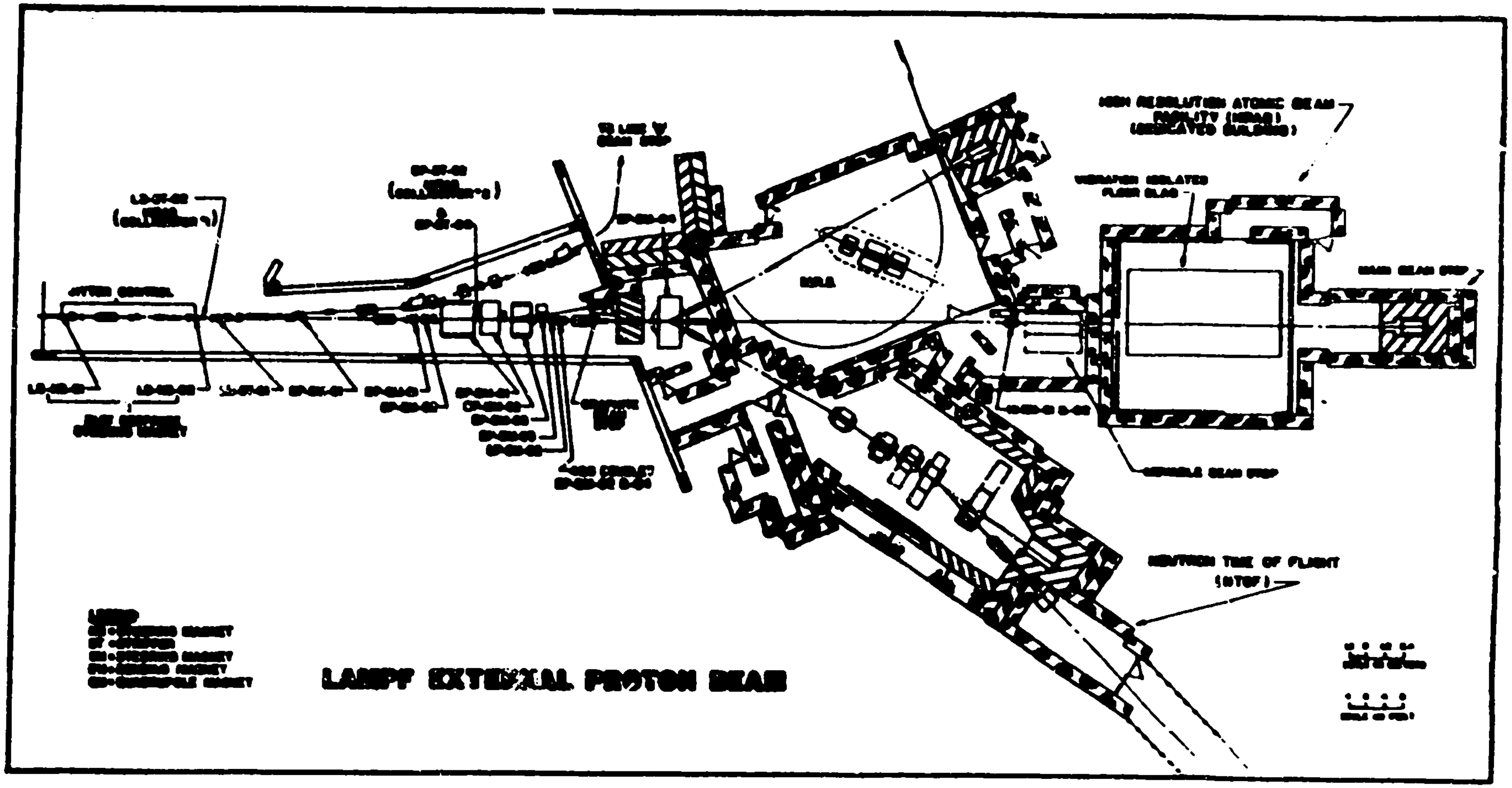

Figure 3.2: The LAMPF beamline.

3.2 Relativity's Role

Relativistic ion beams provide the opportunity to study photodetachment over a continuous range of photon energies. The range depends on the ion beam velocity v. For $v \approx 0.8c$ one obtains energy tunability over about an order of magnitude.

The energy E_{CM} of a laboratory photon as viewed from the ion's frame is given by the Lorentz transformation,

$$E_{CM} = \gamma E_{lab} - \beta\gamma p_z \ , \tag{3.1}$$

where p_z is the z-component of the photon's lab momentum vector, and β and γ are the usual relativistic quantities. Using $p_z = -p_{lab} cos\ \alpha$ and $E_{lab} = p_{lab}$ for photons, we have (See Appendix A)

$$E \equiv E_{CM} = \gamma E_{lab}(1 + \beta\ cos\ \alpha) \ , \tag{3.2}$$

where α is the angle of laser–ion beam intersection, taken to be zero when the beams meet head-on. Thus, rotation of the laser beam with respect to the ion beam effectively tunes the photon frequency $\nu = E/h$ seen by the moving ions. This process is accordingly called "Doppler tuning". Using a variety of lasers (Nd:YAG, CO_2, ArF), photon energies in the barycentric frame may be produced ranging from 1.16 to 14.4 eV for an 800 MeV beam. In contrast, dye laser photon energies are tunable only from about 1.1 to 4.1 eV and Ti-Saf lasers from about 1.3 to 1.8 eV.

The relativistic transformations also induce an enhancement in the intensity of the laser. The intensity is proportional to the magnitude of the Poynting vector $|\vec{E} \times \vec{H}|$ [55]. Transforming $\vec{E}$ and $\vec{H}$ according to the Lorentz field transformation formulas [56] obtains

$$\frac{I_{CM}}{I_{lab}} = \gamma^2(1 + \beta \cos \alpha)^2 \,. \tag{3.3}$$

So for β=0.842 and α=0, an order of magnitude is also gained in laser intensity. Figure 3 displays intensity vs intersection angle for our lasers.

3.3 Energy Resolution

The energy resolution is dictated by the energy spread and divergence of both the laser and the H^- beam. The equation for the energy resolution is found by taking partial derivatives with respect to the parameters α, p, and E_L of the Doppler-shift equation for the center-of mass energy E (Eqn. 3.2).

The quantities $\delta E_L, \delta\alpha$, and δp are considered to be uncorrelated, so that the energy resolution $\delta E/E$ may be taken as a sum in quadrature of the partial derivatives. Neglecting all but the lowest order term obtains

$$\frac{\delta E}{E} = \sqrt{\left(\frac{\delta E_L}{E_L}\right)^2 + \left(\frac{\beta \sin \alpha \; \delta\alpha}{1 + \beta \cos \alpha}\right)^2 + \left(\frac{\beta^2 + \beta \cos \alpha}{1 + \beta \cos \alpha}\right)^2 \left(\frac{\delta p}{p}\right)^2} \,, \tag{3.4}$$

where $\delta E_L/E_L$ is the linewidth of the laser, $\delta\alpha$ is the combined angular divergence of the laser and ion beams, and $\delta p/p$ is the momentum spread of the H^- beam. The energy spread of the laser beam (linewidth) is in our case negligible (≈ 1 μeV).

The dominant contributors to $\delta E/E$ are the $\delta p/p$ term and the $\delta\alpha$ term. These are plotted vs α along with $\delta E/E$ in Figure 3.3 using the relevant values for our experiments. The value of $\delta p/p$=5(10^{-4}) is attainable using momentum bunching of the 716 MeV H^- beam [57]. For 800 MeV beam the momentum spread is greater

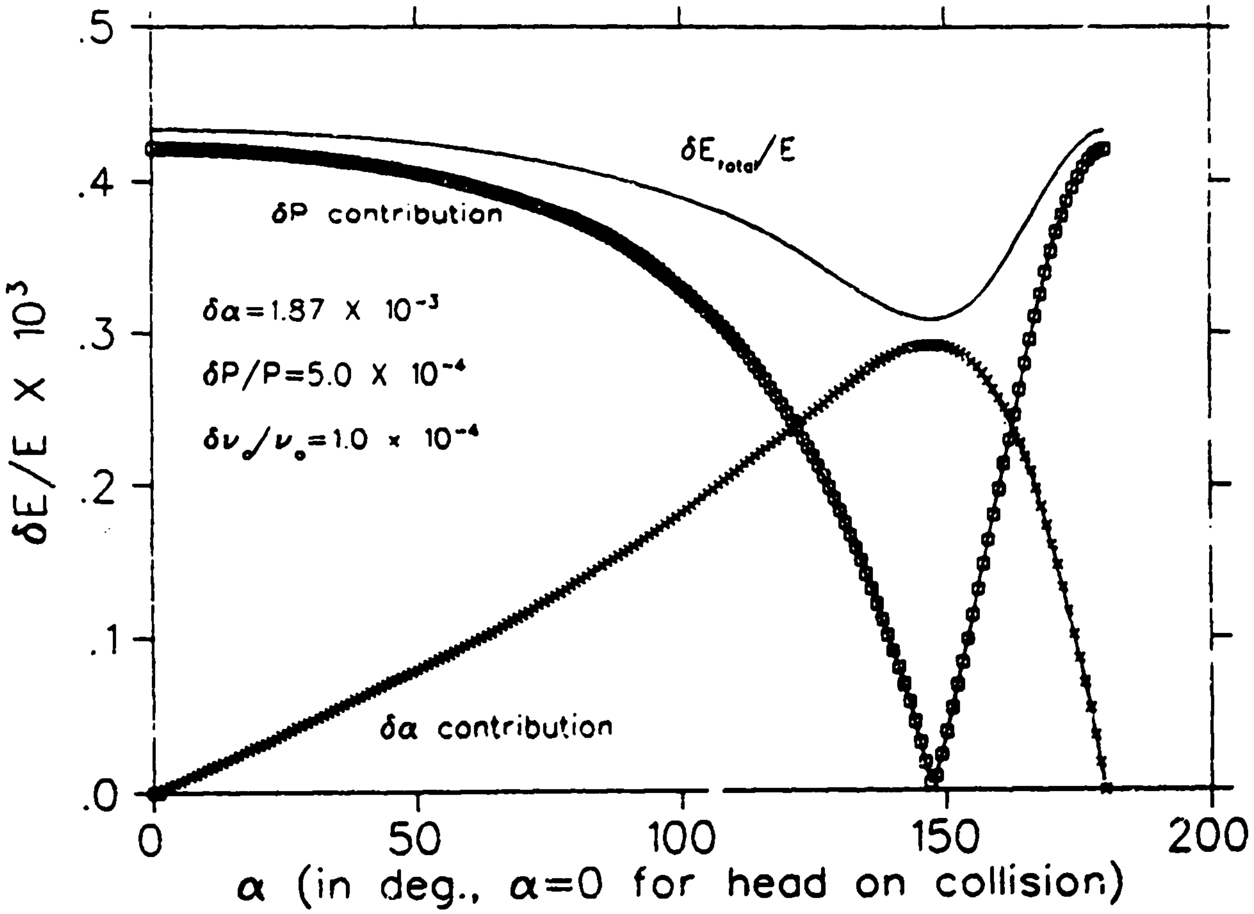

Figure 3.3: $\delta\alpha$ and δp contributions to the energy resolution.

by about a factor of five.

The actual energy resolution was measured in several runs, by scanning the $H^{-**}(2)$ Feshbach resonance. Theoretical values for the full width at half maximum (FWHM) of this feature are generally around 30 μeV [58], so its measured width is a good determination of our experimental resolution, found to be 7±1 meV.

3.4 1990 Apparatus

The 1990 basic setup is sketched in Figure 3.4. On entering the HIRAB experimental area in an evacuated 6″ beam tube, the 800 MeV H^- beam provided by LAMPF first passes through a vertical steering magnet which is used to direct the ion beam to the center of the interaction region. Next it passes through a chamber whose main function is to introduce foils by remote control into the beam's path in foil transmission experiments, but which also contains a slide of fluorescent material which can be inserted in the beam line to aid in location and steering of the beam for all experiments.

A sweep magnet, just downstream of the sliding foil chamber is set to sweep free electrons out of the beam before they reach the interaction region. (It may also be used to selectively field-ionize Rydberg states created in foil-transmission experiments.) Any neutral particles which may be present are not a problem, since electrons are the signal of interest in this experiment.

Next the H^- beam enters the first interaction region (the big chamber, region 1 in Figure 3.5) where it intersects the fourth harmonic of our Nd:YAG laser (YAG)

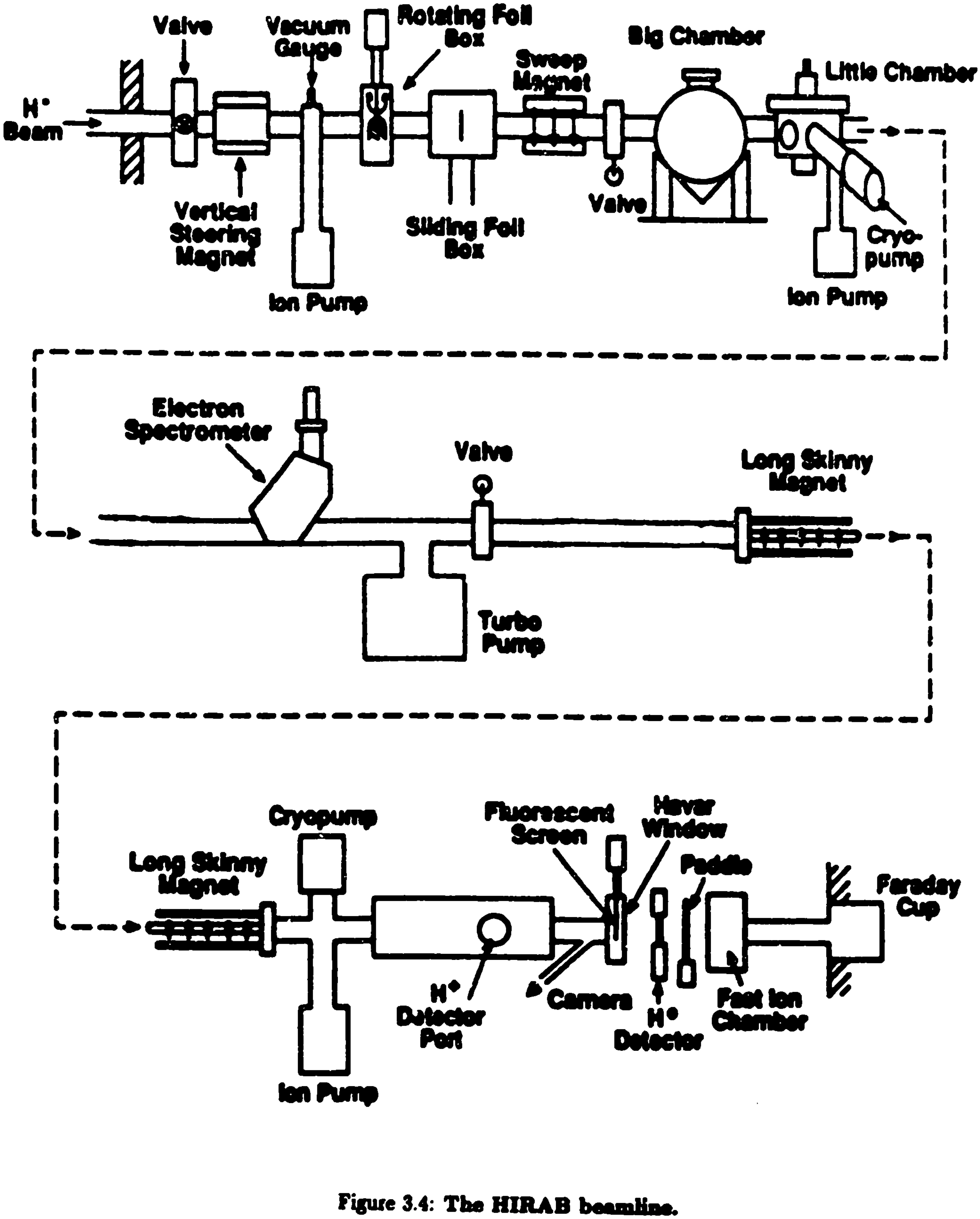

Figure 3.4: The HIRAB beamline.

at a series of angles α which provide the center-of-mass (CM) energy needed to span the particular state we choose to excite (See section 3.2) by the reactions

$$H^- + h\nu \longrightarrow H(N) + e^- \tag{3.5}$$

and

$$H^- + h\nu \longrightarrow H^{-**}(n) \longrightarrow H(N) + e^-, \tag{3.6}$$

where $h\nu = E_{CM}$ and $H(N)$ is the neutral hydrogen atom in either its ground state or an excited state with $N < n$ if $n > 2$. (For n=2, the H^{-**} shape resonance can decay to its "parent" state H(2). More on this later.) The doubly-excited state H$^{-**}(n > 1)$ thus produced then decays to H(N) + e$^-$ before leaving the chamber (H^{-**} lifetimes $\leq 10^{-12}$ seconds).

About one and a half nanoseconds later the H atoms, some in the N=2 excited state, encounter the second laser beam in the "promotion" chamber. The neutral atoms and freed electrons then pass through the second interaction region (little chamber, region 2 in Figure 3.5). In the case of the partial decay experiments, they are intersected by the first harmonic of the YAG. By rotating the mirror arrangement (Figure 3.6) in the little chamber, the intersecting laser beam is moved to the angle which provides the CM photon energy necessary to excite H(N=2) to H(11).

When detecting electrons, the H(N) partial decay state we wish to observe must be promoted to H(11) because the spectrometer is incapable of stripping lower-N states while still maintaining the proper electron trajectory. The process in the

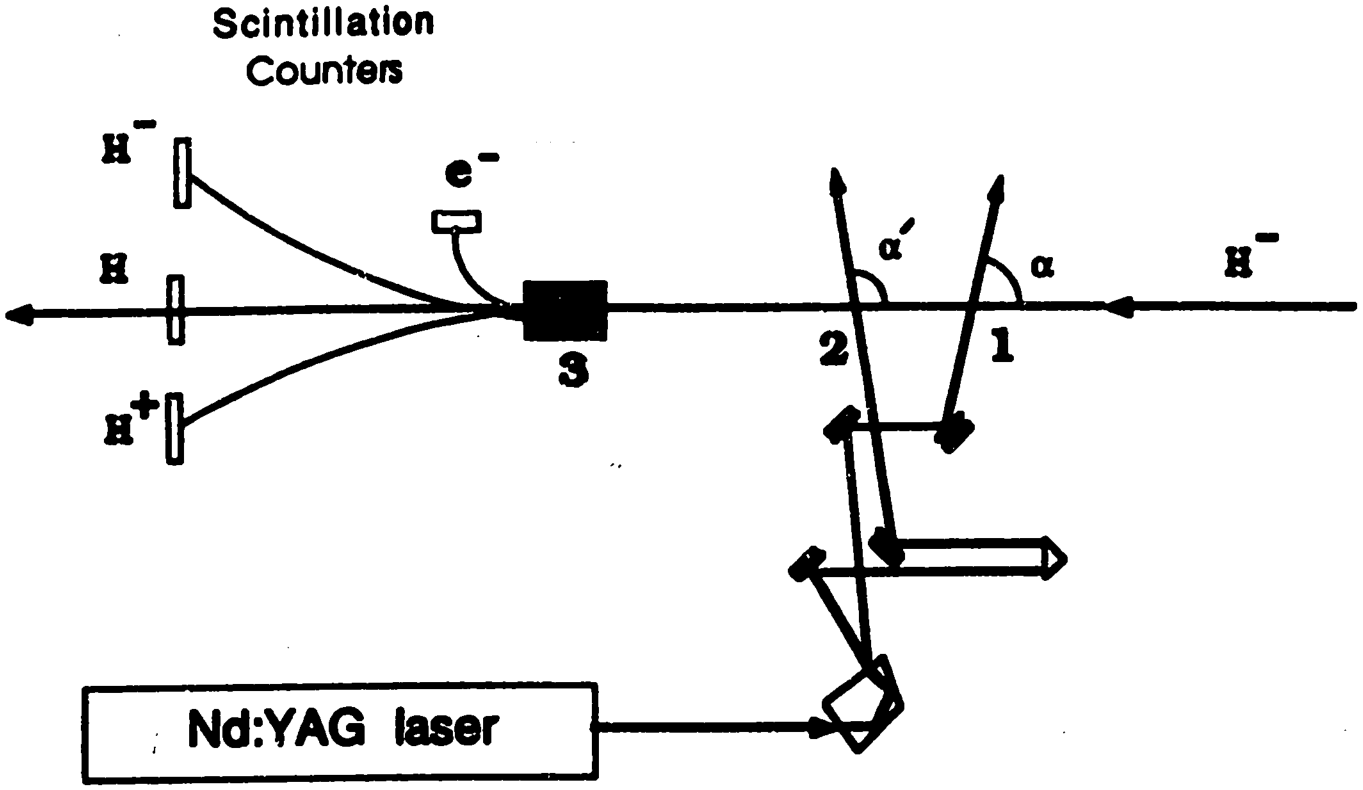

Figure 3.5: The interaction regions.

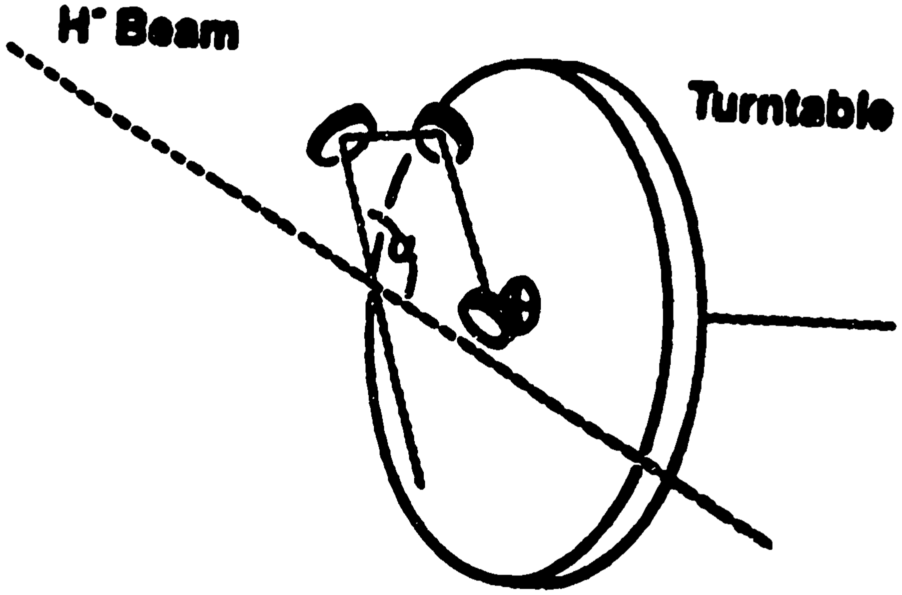

Figure 3.6: The mirror arrangement or "spider".

promotion chamber is

$$H(N=2) + h\nu' \longrightarrow H(N') \Longrightarrow H^{+} + e \tag{3.7}$$

where N'=11 and the double arrow indicates that the second step proceeds in an electric field. The H(11)s are then stripped of their electrons by our electron spectrometer (region 3 of Figure 3.5). These electrons, when detected in coincidence with a laser pulse and an H$^-$ beam pulse, constitute our signal for production of H(2).

The experimental procedure described above can, in principle, also be used to detect autodetachments that leave the atom in its ground state H(1), if the fourth harmonic of the YAG is used in the promotion chamber. This method was not practicable, however, because the two interactions

$$H^{-} + h\nu \longrightarrow H(1) + e \tag{3.8}$$

and

$$H(1) + h\nu \longrightarrow H(N') + e \tag{3.9}$$

can occur in sequence within the second interaction region. The H$^-$ single photon photodetachment cross section is large near the energy of the second laser. There are many more H$^-$ ions in the beam at the second laser than there are H(1) atoms from shape resonance autodetachment. The net result is that far more protons are produced from (3.8) plus (3.9) than from decay of the shape resonance, making the measurement of the cross section for H^{-**}(2) → H(1) unfeasible.

For the total cross section measurement of the shape resonance described in Chapter 7 the second laser beam was not used, and the spectrometer magnet was set to detect convoy (free) electrons from photodetachment and photoexcitation by the first laser with subsequent autodetachment.

The beam itself must also be monitored for normalization and timing purposes, so additional detectors are placed further downstream of the scattering chambers. Before reaching these detectors, the beam is separated into its four different charge components (H^-, H, p, and e^-) by a long magnet. This magnet allows the different charge species to be separated, but not by too much, so that scattering by the heavy particles off the beampipe walls is minimized. About $11\frac{1}{2}$ feet downstream from the long magnet the three heavy components of the beam exit through a thick stripping foil into air in our beam dump area, creating three separated proton beams whose trajectories depend on the charge species from which they originated. A thin scintillation detector placed immediately downstream of the foil is remotely moved across the exit region to intercept any of the three beams. We call this the "proton detector".

In previous runs a paddle scintillator just downstream of the proton detector was used to monitor the timing structure of the beam, as well as relative amplitude of the micropulses, but had been found to saturate. Therefore, I designed and installed a Čerenkov detector to monitor the pulses, and placed it just behind the paddle scintillator. Because the beam current was lower than in other years, the paddle in fact had no saturation problems in 1990, but the Čerenkov detector worked well and served as the beam monitor. In the case of beam structure with micropulses separated by only five ns, the Čerenkov detector, with a response of about 1 ns, will be essential, as the paddle scintillator response is about 20 ns.

A fast ion chamber, located between the Čerenkov detector and a Faraday cup located at the furthest downstream position of the beam, was not used in the experiment. The Faraday cup, however, embedded in the beam dump, played an important role in that it signaled when a predesignated quantity of charge had entered, so that the laser angle should be changed. Details on the use of this signal appear in Section 6.1.

Our beamline vacuum was maintained by three ion pumps. The first was between the vertical steering magnet and the foil chamber, the second pumped the promotion chamber, and the third was just downstream of the long magnet. In addition, two cryogenic pumps and a turbopump were used. One cryopump was attached to the promotion chamber and one opposite the furthest-downstream ion pump. The turbopump pumped on the beampipe just downstream of the electron spectrometer.

A nude ion gauge on the promotion chamber indicated a pressure of about $4(10^{-6})$ Torr throughout the run, in agreement with the currents measured in the ion pumps. This is not a very good vacuum by most standards, and could have caused high background if protons had been the signal of interest, as in the 1989 run [57]. It did cause a small problem in 1990 because some laser-detached electrons from the residual gas seem to have made their way into the electron spectrometer (See Section 6.1).

3.5 1989 Apparatus

The 1989 experimental configuration for the electric field studies shown in Figure 3.7 differed somewhat from the 1990 situation. The resonances of interest were those converging on the H(N=5,6, and 7) thresholds. These were excited as in the 1990 experiment description—by scanning the YAG fourth harmonic through the necessary range of α. Two parallel steel capacitor plates separated by one centimeter supplied the electric field to the interaction region in the big chamber. The field seen by the ions is $F_{CM} = \gamma F_{lab}$, where F_{lab} varied from 0 to 50 kV/cm and γ=1.85, so $F_{CM} \approx 0 \rightarrow 90$ kV/cm.

In the 1989 experiment the photon energy ranged from 13.4 to 14.2 eV, encompassing the H(N=4, 5, and 6) thresholds. Measured partial decay cross sections display large downward shifts in the threshold energy in response to applied static electric fields ranging from 0 to 90 kV/cm. The term "threshold", which is not well-defined in the presence of fields, is here taken to mean the apparent threshold or onset of electron detachment.

The excited neutral hydrogen atoms H(N>1) formed by the photodetachment of H^- are field-stripped and detected as protons downstream in a scintillation counter. An ionizing magnet located between the scattering chamber and the detector allows the selection of the specific N state to be monitored. For example, at CM energies between 13.50 and 13.80 eV, only H atoms with principal quantum number N$\leq$4 are produced. The ionizing magnet is set to a field which strips H(4), but leaves lower states unaffected. The resulting protons are deflected by a charge-separating

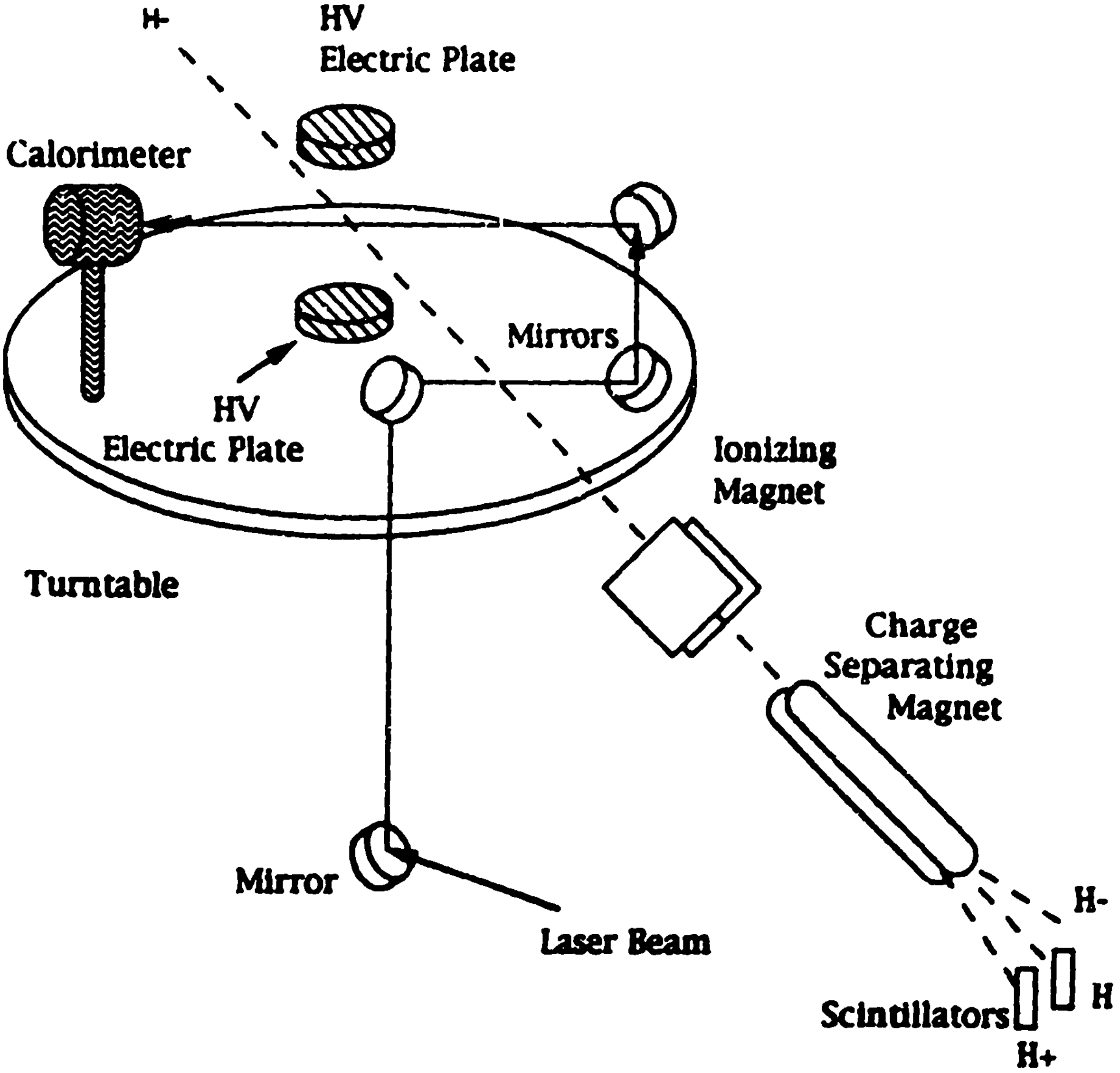

Figure 3.7: The 1989 setup for electric field studies. Electric field plates were retracted for the zero-field work.

magnet into a separate counter from the neutral atoms, and constitute the signature for photodetachment when observed in coincidence with a laser pulse. At higher photon energies, atoms with N = 5 and 6 were counted in a similar manner.

The dominant decay channel, expected to be H(n-1), was monitored by setting a stripping magnet to a field which detaches electrons from H(n-1) while leaving lower levels intact. Protons were then the event signal, detected downstream in a scintillation counter. Background was a bigger problem than in the electron detection scheme of 1990, but was carefully monitored and subtracted. Details of the process are given in reference [57].

3.6 Beam alignment aids

To assist the accelerator operators in steering the H^- beam along a straight line through the beampipe in the HIRAB experimental area, four remotely-insertable phosphorescent screens have been installed in vacuum. The furthest upstream phosphorescent screen ("fluor"), holds a slot in the sliding foil chamber. The second fluor is attached with Torr-Seal to the electric field plates which may be moved in and out of the beam line using a voltage-dependent actuator. The third fluor is attached to the same type of actuator in the little chamber, and a fourth actuator, in the beam dump area, moves a larger fluor in and out of the beam. All these regions are monitored with TV cameras, whose signals may be sent to the central control room of the accelerator and the HIRAB counting house. Usually the first (foil chamber) and last fluors are sufficient to align the beam.

Chapter 4

Gadgets

The devices used in 1990 for detection and control along the beam line in our experimental area are described here. For 1989 devices, see reference [57].

4.1 Laser and Optics

For both the 1990 and 1989 studies, the fourth harmonic (E_L=4.66 eV) of a Spectra Physics Q-switched DCR-2A Nd:YAG laser (Figure 4.1) was intersected with the H^- beam. The laser's active medium (triply-ionized neodymium) is optically pumped by a flash lamp whose output matches principal absorption bands in the red and near-infrared. Excited electrons quickly deexcite to the upper level of the lasing transition ($F_{3/2}$) as shown in Figure 4.2 [59]. The dominant laser transition to the $I_{11/2}$ state emits a 1064 nm photon (fundamental). The frequency conversion to the fourth harmonic was accomplished by separating the harmonics in a quartz Pellin-Broca prism. The DCR-2 prism harmonic separator is pictured in Figure 4.3,

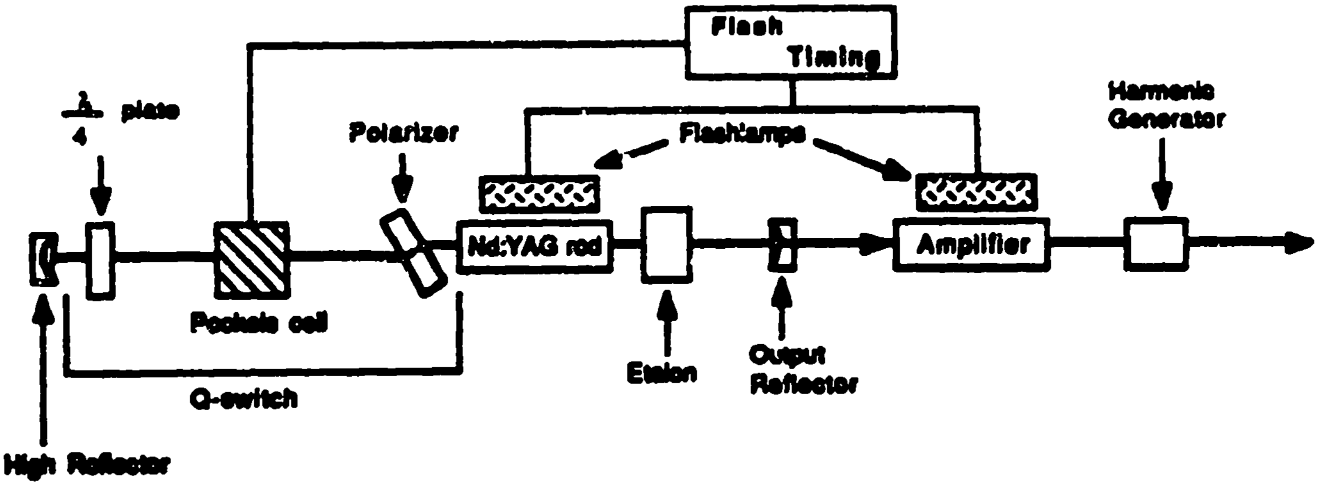

Figure 4.1: Schematic diagram of the Nd:YAG laser.

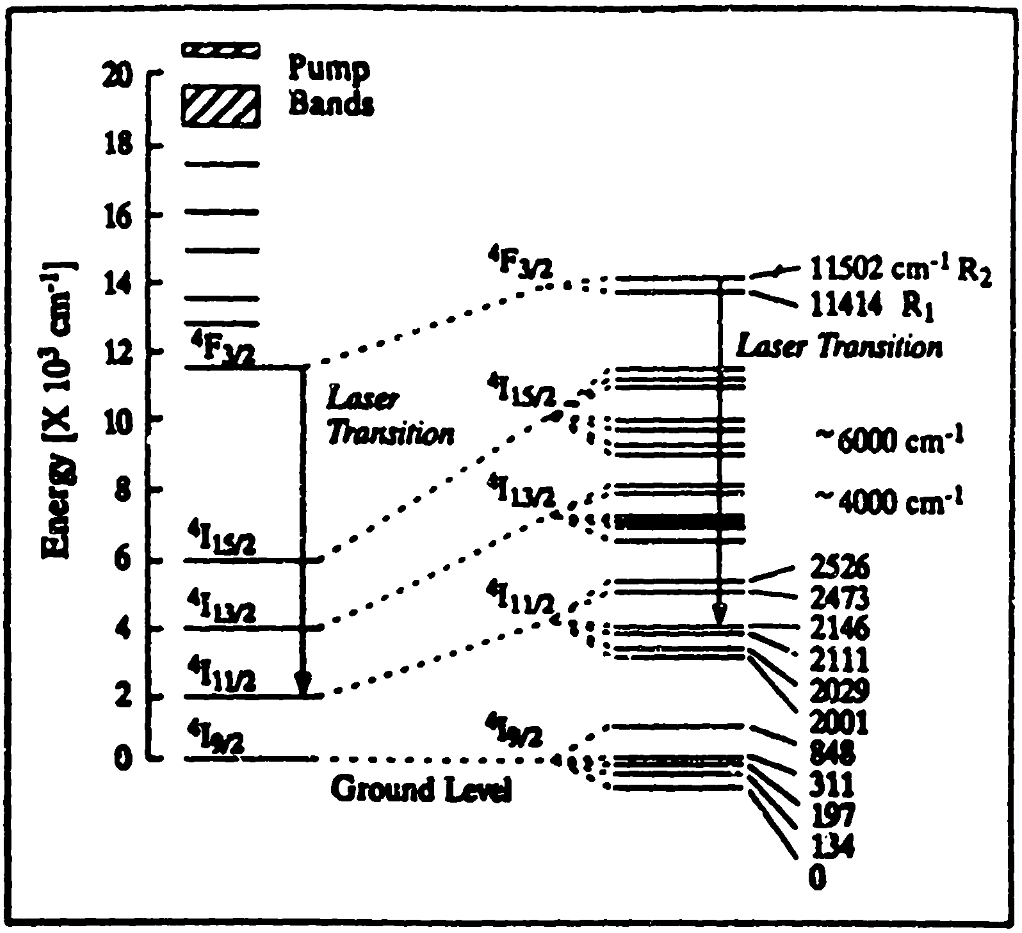

Figure 4.2: YAG energy levels of interest.

where rectangular optics are half-wave plates, and triangular optics are prisms which are translated to intercept and direct the different harmonics.

After passing through the prism, the fourth (first) harmonic beam is directed to the big (little) chamber by two dielectric mirrors (reflectivity $\approx$ 99.9%). The laser beam enters the chamber through a quartz window. Inside the chamber it encounters the mirror arrangement or "spider", which holds three mirrors connected to an encoder-equipped stepping motor, allowing the change of laser-H^- intersection angle.

The pulse repetition rate was 10 pps, with an output-pulse time-jitter of less than 1/4 ns and a divergence of about 1 mr. The laser delivered 50 mJ/pulse with a pulse length of 9 ns. The laser beam in the chamber measured 0.1 cm by 1 cm, yielding an intensity

$$I = \frac{Power}{Pulse\ length} \times \frac{1}{Beam\ area} \approx 6(10^7)\frac{\mathrm{W}}{\mathrm{cm}^2} \tag{4.1}$$

with an intensity in the center of mass of about $5\times(10^8)$.

4.2 Detectors

4.2.1 Electron Spectrometer

Our most important detector, the electron spectrometer, was designed and built in 1986 [60]. Figure 4.4 depicts the basic characteristics. The main working component is the wire-wrapped solenoid cavity which is in direct contact with the evacuated beamline. The magnetic field B of the solenoid is seen in the frame of the H^- ions

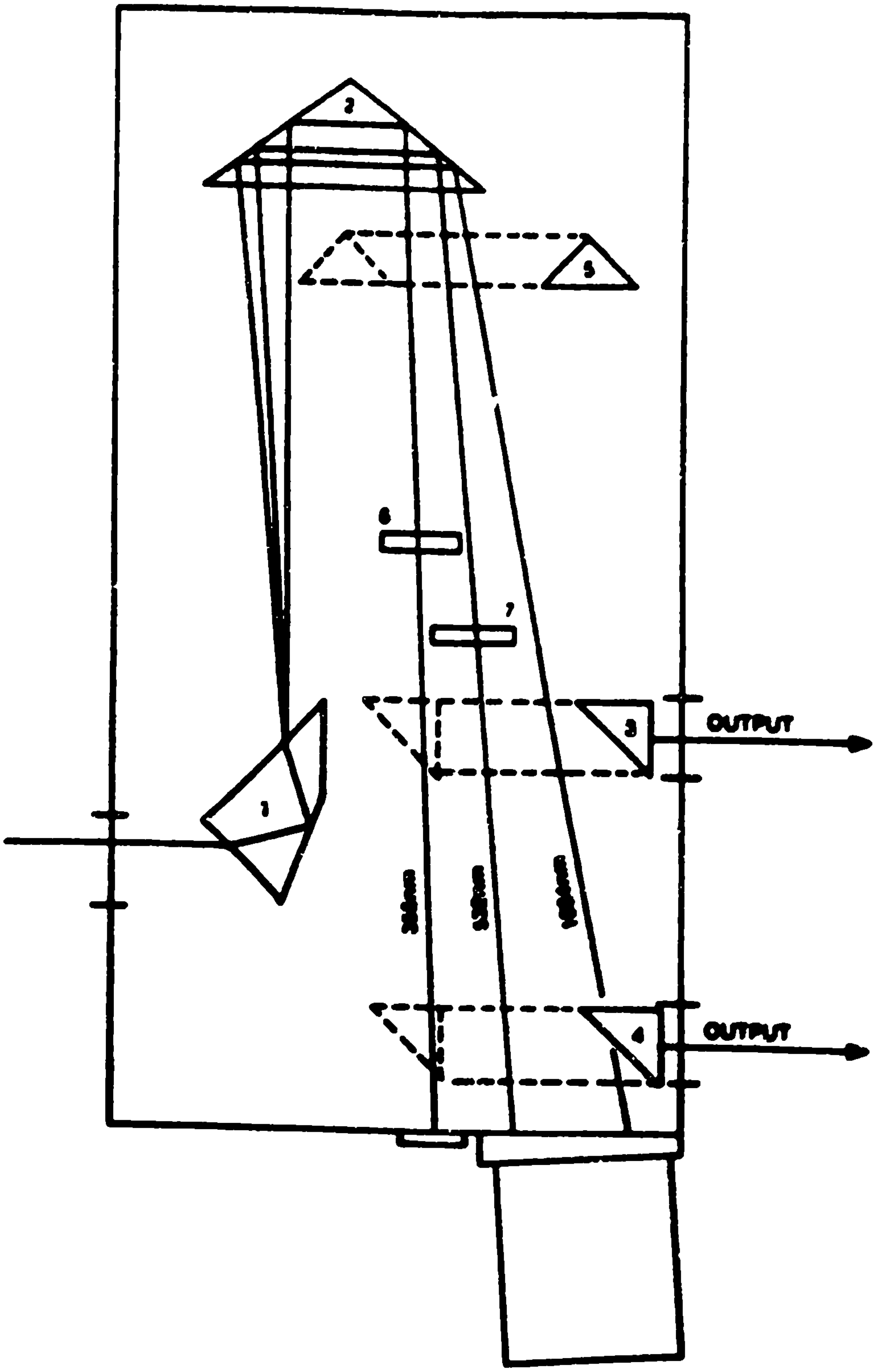

Figure 4.3: Prism harmonic separator used to generate first and fourth harmonics of the YAG.

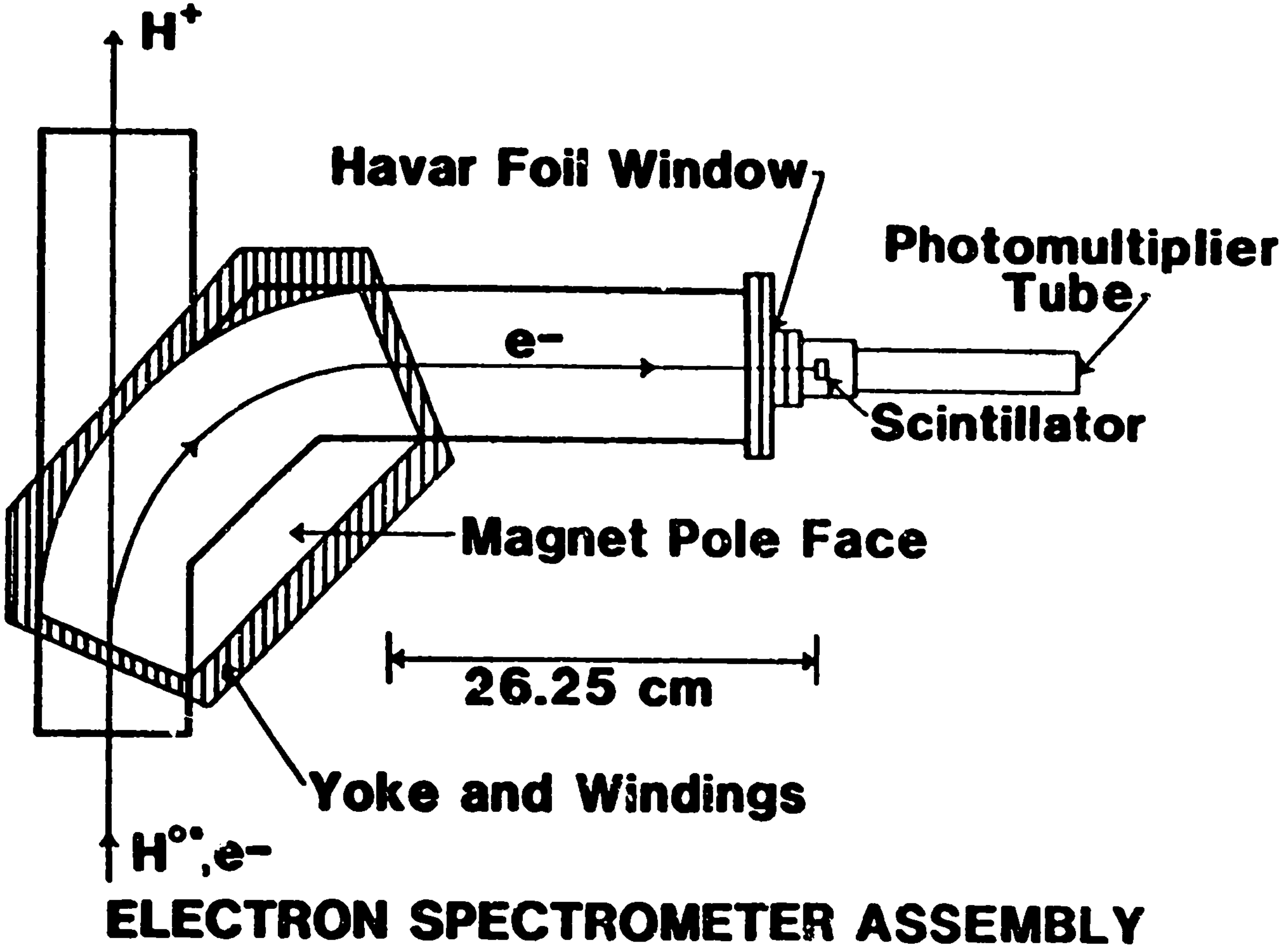

Figure 4.4: The electron spectrometer.

and fragments (protons and electrons) as an electric field F, given by the Lorentz transformation $F = \gamma\beta cB$ in S.I. units (See section 3.2). This means that changing B—by changing the current supplied to the solenoid—changes the electric field. This ability to choose electric field strength allows us to selectively strip electrons from neutral hydrogen in different excited states that result from autoionization of the H^- doubly-excited state.

The device is capable of stripping and detecting electrons from H atoms having $n \geq 10$ (momentum resolution $\approx 1.5\%$). To detect remnants for $n < 10$, we must either detect the H^+ fragment, or promote the atom to a higher level before it reaches the spectrometer. The former method was used for the 1989 electric field experiment, while the latter was used for the 1990 partial decay experiment.

The stripped electrons pass through a thin (0.5 mil) mylar foil after traversing a 180 degree bend in the spectrometer, and are detected in a scintillator–photomultiplier-tube combination. Only electrons which arrive (after a suitable timing delay) in coincidence with a laser pulse intersecting a beam pulse are recorded by our data acquisition system (See Section 6.1).

4.2.2 Čerenkov detector

In the summer of 1990 I designed and installed a mineral oil Čerenkov counter (built at the University of New Mexico machine shop) in the HIRAB beam line between the paddle scintillator and the fast ion chamber. The counter was intended to replace the paddle-shaped scintillation detector because there were problems with

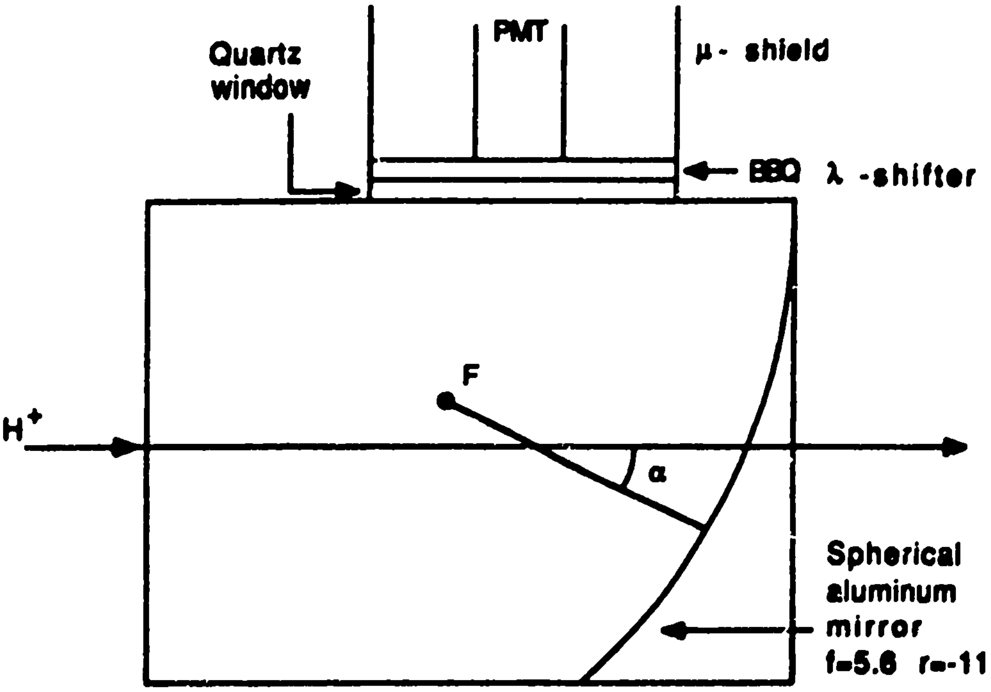

Figure 4.5: The Čerenkov detector.

scintillator saturation in the past, which made relative amplitude information for the micropulses unobtainable.

A diagram of the counter is shown in Figure 4.5. With β=0.842, the Čerenkov angle θ_c is 36°, as give by the formula [61]

$$\theta_c = arccos \frac{1}{n_r\beta} \tag{4.2}$$

where the index of refraction n_r is 1.47 for mineral oil. A spherical aluminum mirror was mounted at an angle of θ_c below the particle track to reflect into the window Čerenkov photons from 800 MeV protons, but can also be mounted at different angles for different beam energies or Čerenkov media. I initially designed the detector for water as medium, but tests showing rapid mirror corrosion by hydrolysis prompted the change to mineral oil.

Three Amperex XP2262 photomultiplier tubes detected the Čerenkov light exiting the 5″ diameter ultraviolet (uv) transmitting window. (Actually one of the tubes went bad, but the counter still worked quite well with only two, or even one.) To enhance ultraviolet light detection, BBQ wavelength shifter was inserted between the photomultiplier tubes and Čerenkov box window, which was made of uv transmitting plastic.

We are interested in the relative amplitudes of the micropulses, so we do not need to know the absolute efficiency of the detector, but we must resolve the micropulses. The detector worked well for 100 ns micropulse spacing in 1990. For 5 ns spacing, however, we must use different wavelength shifter windows, as the time resolution is limited by the 18 ns decay time of fluorescence in BBQ. For this reason I replaced the BBQ with BC–480 fluorescent converter from Bicron, which has an excitation wavelength of 300 nm and peak emission at 425 nm. It ostensibly has a resolution time of about 2 ns, but our detector has not yet been tested with this new wavelength shifter due to lack of beam delivery to the HIRAB area. The time resolution of the counter itself is just the time it takes the photon to travel the path in the mineral oil, about 1 ns.

4.2.3 Faraday Cup

The 700 kg Faraday cup installed at the end of our beamline is depicted in Figure 4.6. The 800 MeV proton beam stops in half a meter of lead surrounded by a graphite

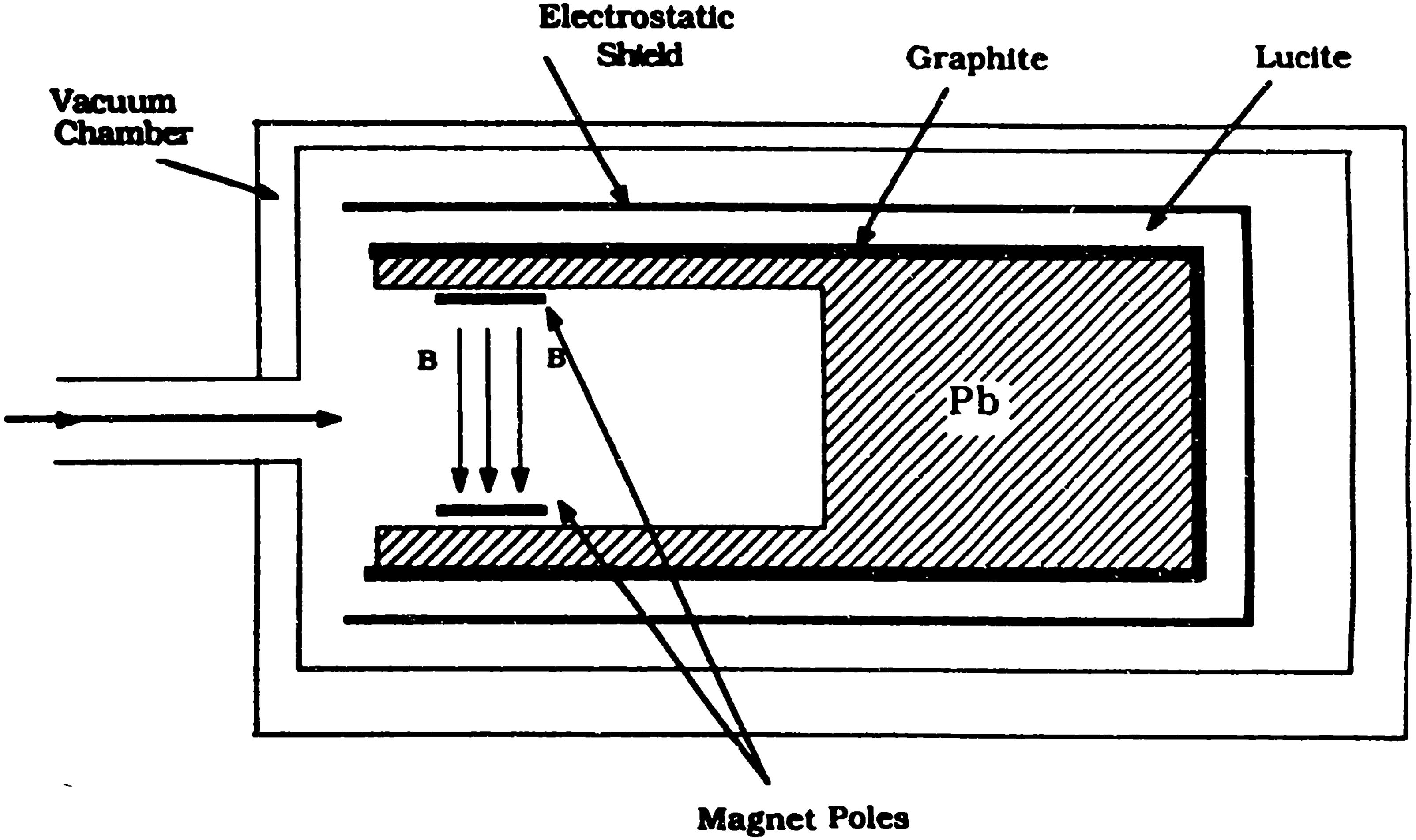

Figure 4.6: The Faraday cup.

shell. The magnet schematically shown in the figure reduces current lost through secondary electron emission [62]. The charge collected in the cup migrates through a teflon-coated wire to a current digitizer that transmits pulses to a visual scaler. These are used for trigger information and normalization purposes. (See Section 5.1) Tests have shown that absolute proton beam intensities may be measured with an accuracy of better than one percent for 800 MeV protons [62].

Chapter 5

Data Acquisition

5.1 Hardware

We used Nuclear Instrumentation Modules (NIM) and Computer Automated Measurement and Control (CAMAC) for the digital electronics interfacing the experimental equipment (lasers, detectors, gaussmeters etc.) with a Digital Equipment Corporation μVAX computer system. The NIM units—such as discriminators, gate and delay generators, linear and logic fans, qVt, amplifiers, coincidence units—sorted and shaped the signals to be fed into the CAMAC modules (ADCs, TDCs, trigger modules, hex scalers, etc), which are interfaced with the computer via a microprogrammable branch driver (MBD). A listing of CAMAC modules (from the HIRAB.QAL file) is given in Appendix F.

The circuits for the 1990 experiment are shown in Figures 5.1 through 5.6. The experimental trigger was a coincidence among five conditions (Figure 18(a)). First, the Faraday cup must be acquiring counts and must not have reached a preset number

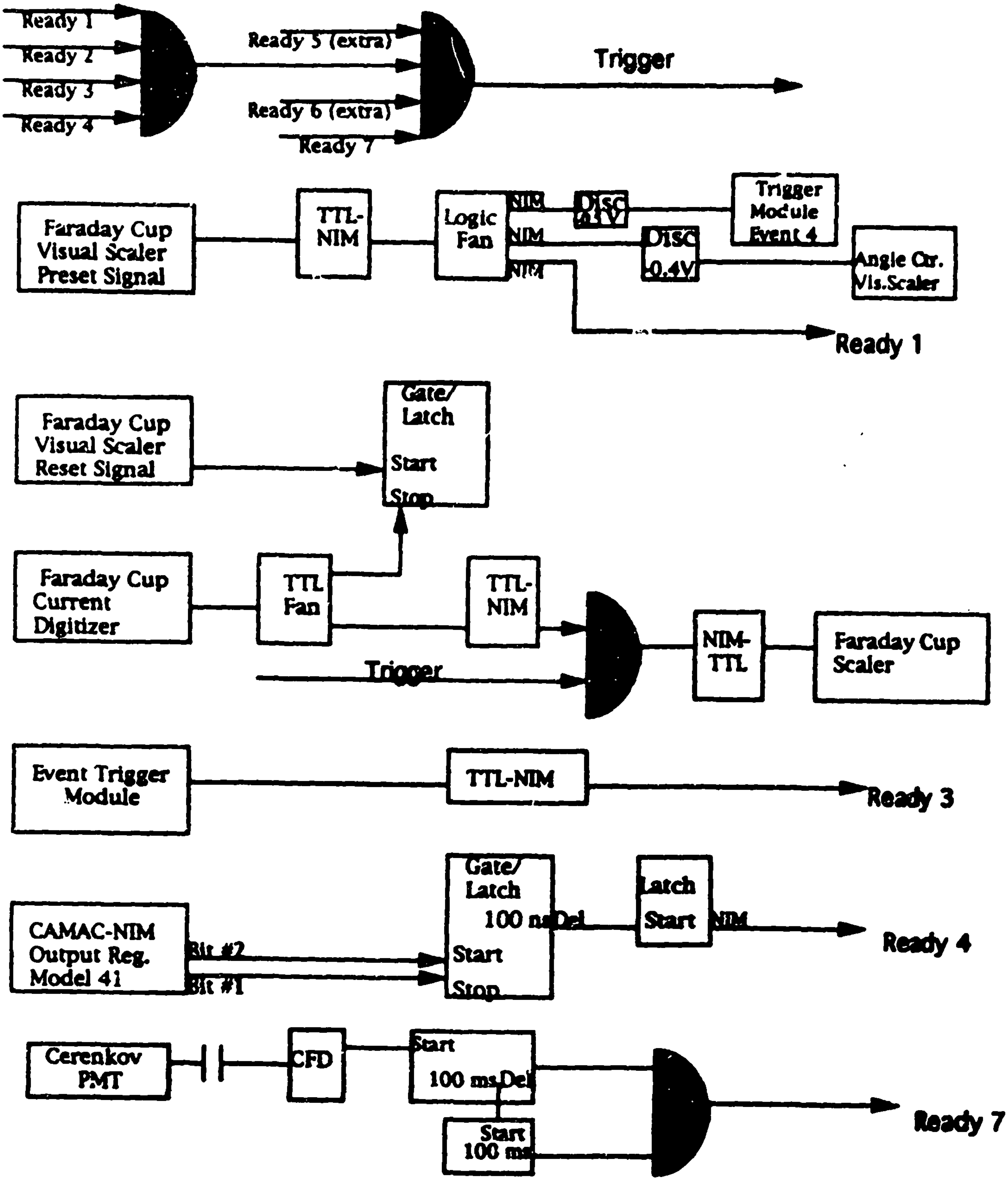

Figure 5.1: Digital electronics circuits.

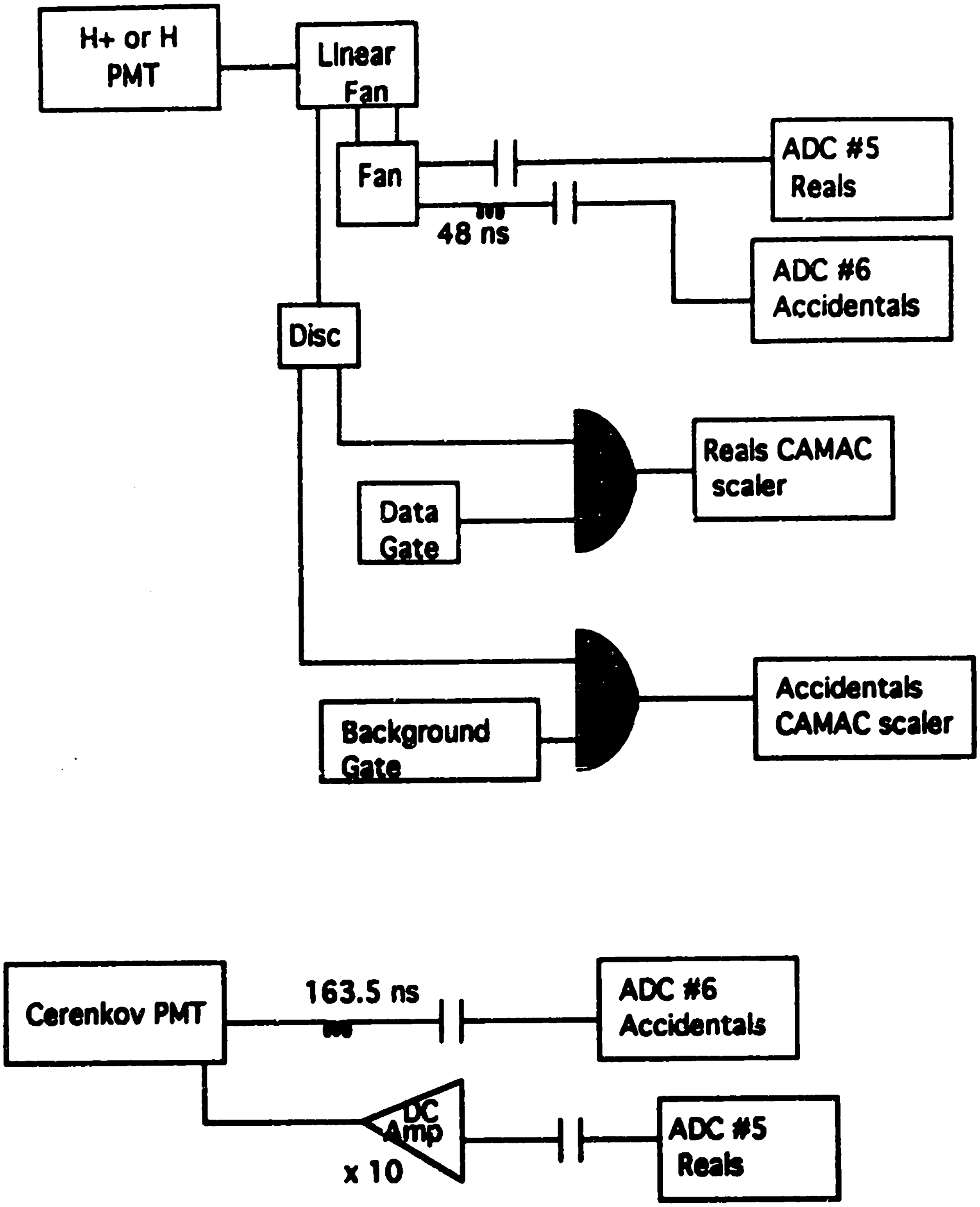

Figure 5.2: Digital electronics circuits.

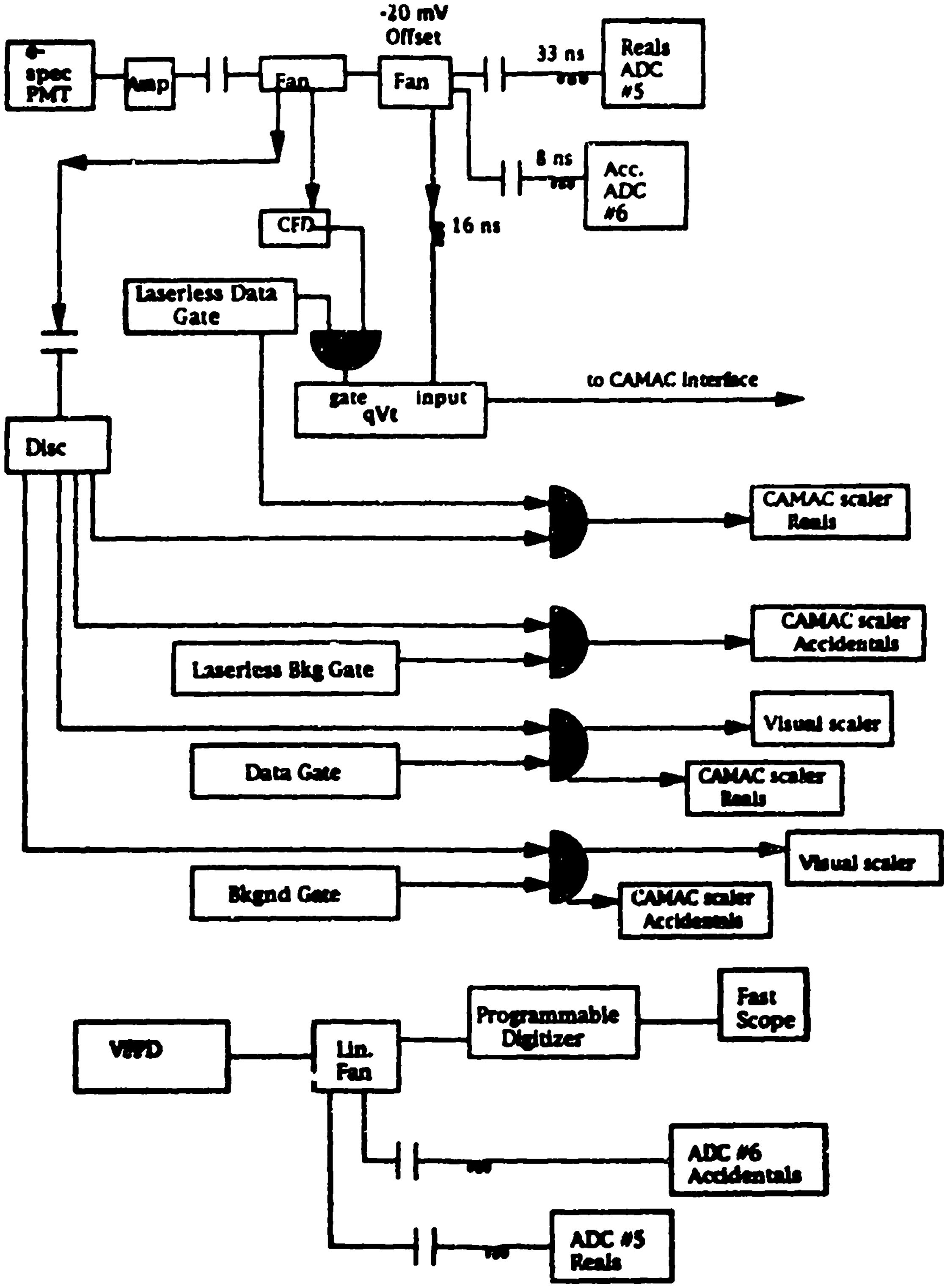

Figure 5.3: Digital electronics circuits.

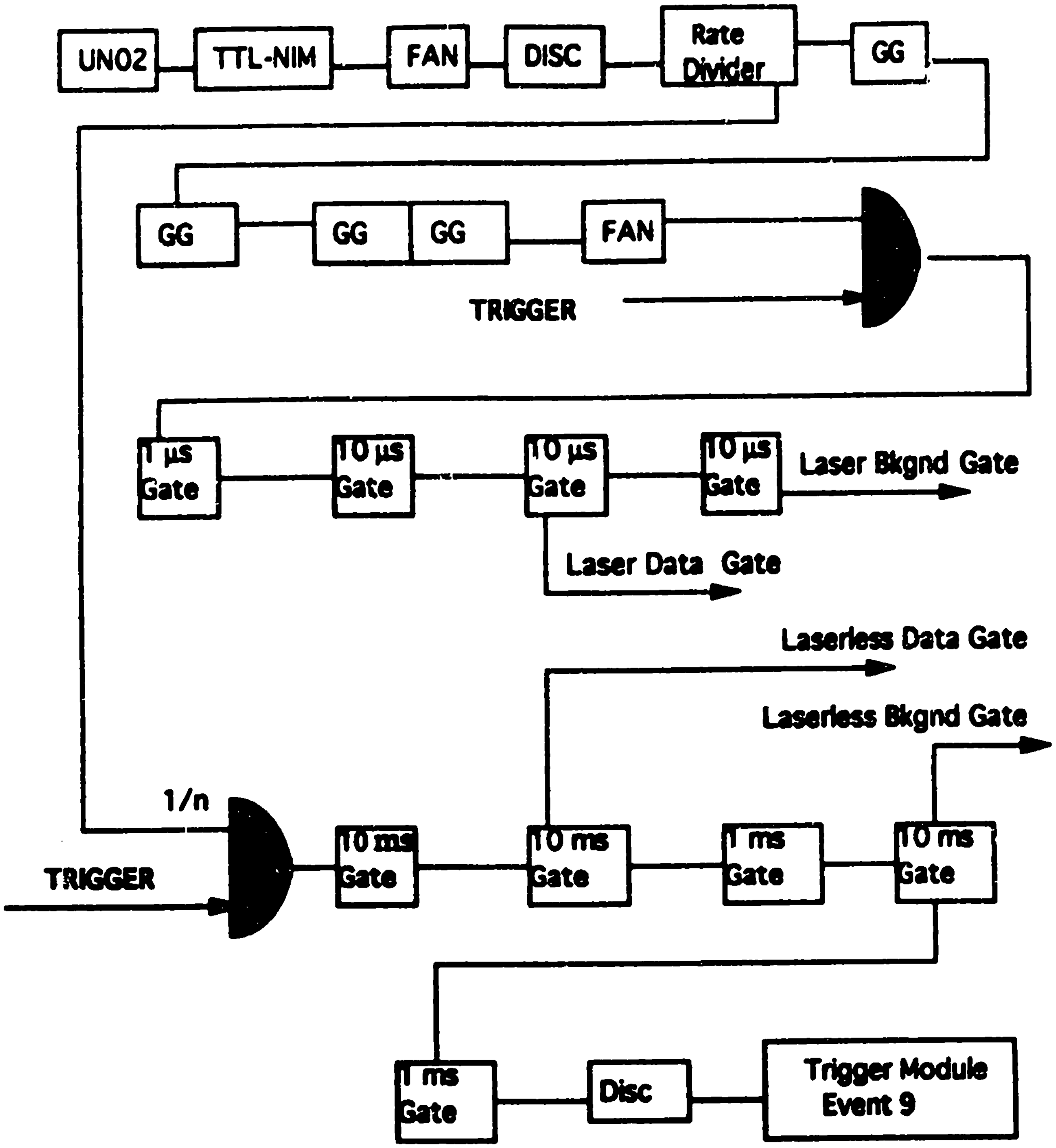

Figure 5.4: Digital electronics circuits.

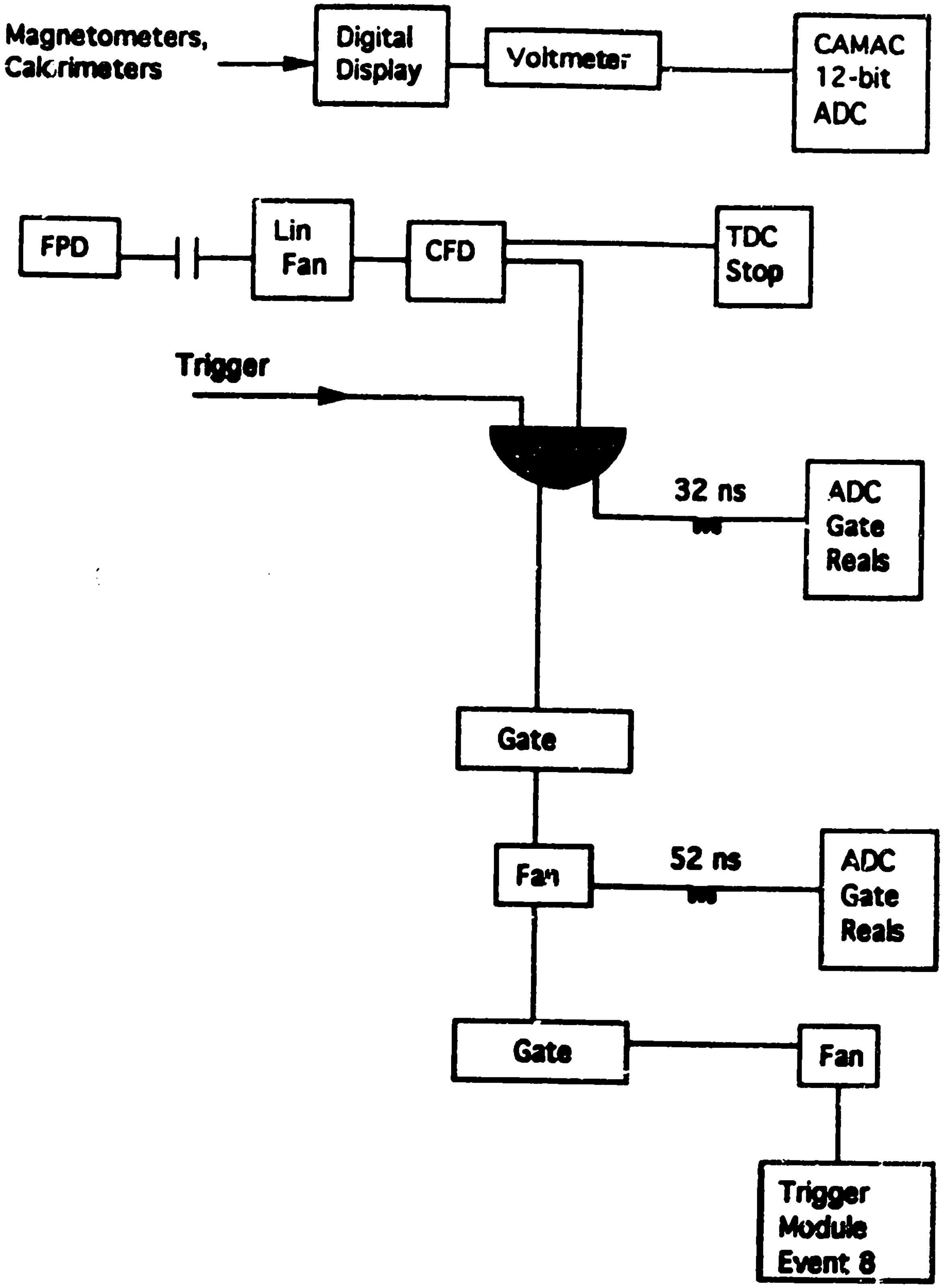

Figure 5.5: Digital electronics circuits.

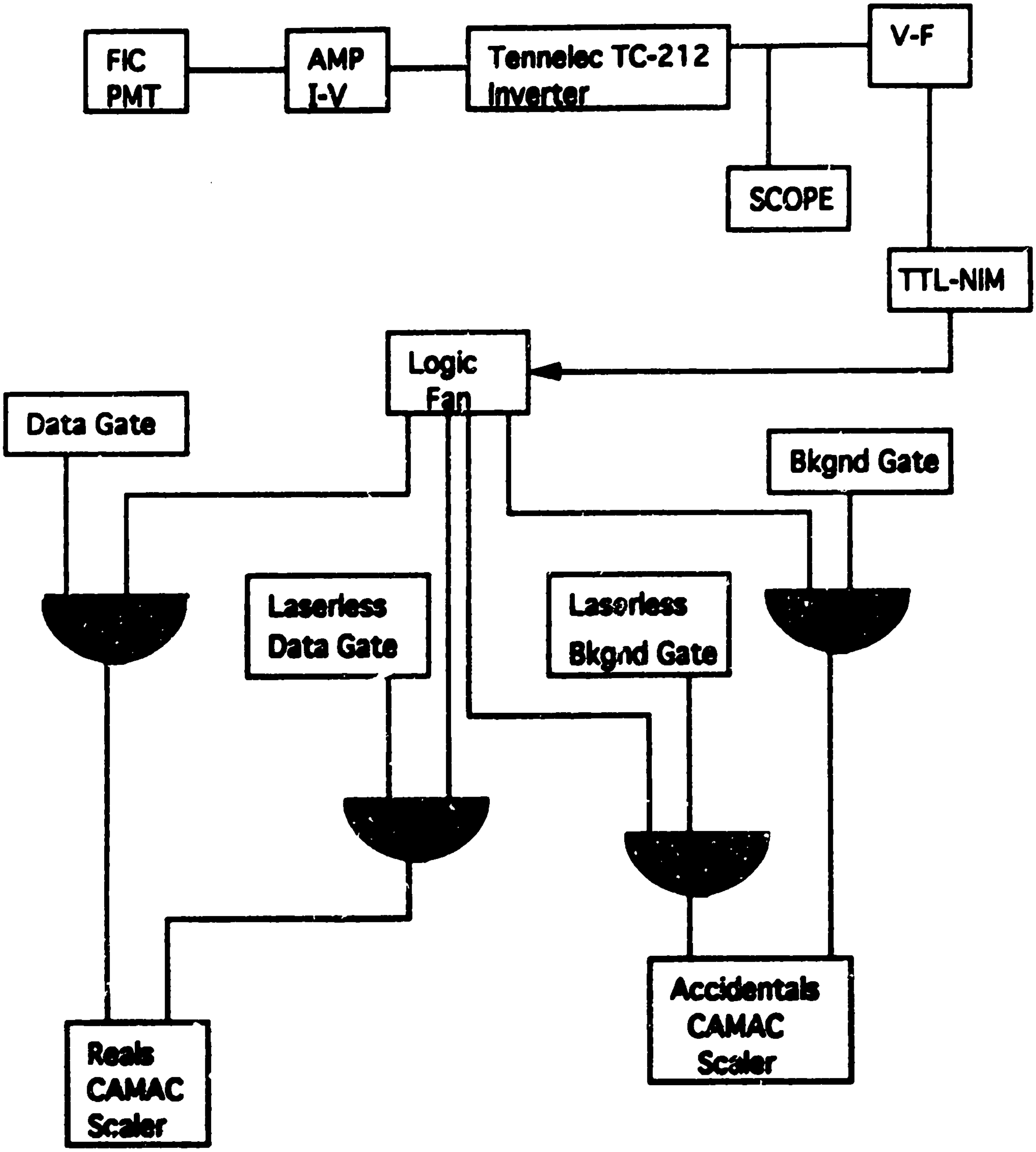

Figure 5.6: Digital electronics circuits.

of counts (set by the user on a NIM timer/counter unit). Second, the computer must not be busy processing a previous event. This is checked by a Q-busy output on the LAMPF trigger module (a CAMAC unit). Third, the spider stepper motor may not be busy, as monitored through the computer by a CAMAC stepper motor controller (SMC-11). Fourth, an H^- beam pulse must be in progress (UN02 signal from the central control room). Fifth, a fast photodiode signal must be present, indicating that the laser has fired. If these five conditions exist, a start gate exists, and the computer collects event data from ADCs, TDCs etc. Background data is collected under similar conditions except that the laser must *not* be firing. The start gate for the background-data-collecting ADCs was simply delayed a sufficient amount of time as shown in Figure 5.7.

The laser flash lamp must be fired 3 ms before the Q-switch allows the release of the laser light. A signal (UN02) from the accelerator operators tells us approximately when the H^- pulse is expected to arrive. This permits time for the firing of the flash lamps. The actual arrival of the H^- macropulse is signaled by the Čerenkov detector. A signal is then sent to the Q-switch to fire the laser in time to intercept the H^- beam while the macropulse is still passing.

By setting the rotating mirror assembly to an angle where the photodetachment cross section is high, the large number of neutral hydrogen atoms produced gives a distinctive laser-related signal in the proton detector. The timing of the laser may then be optimized, insuring that the interaction takes place well inside the macropulse and away from any parts of the macropulse that may be unsteady.

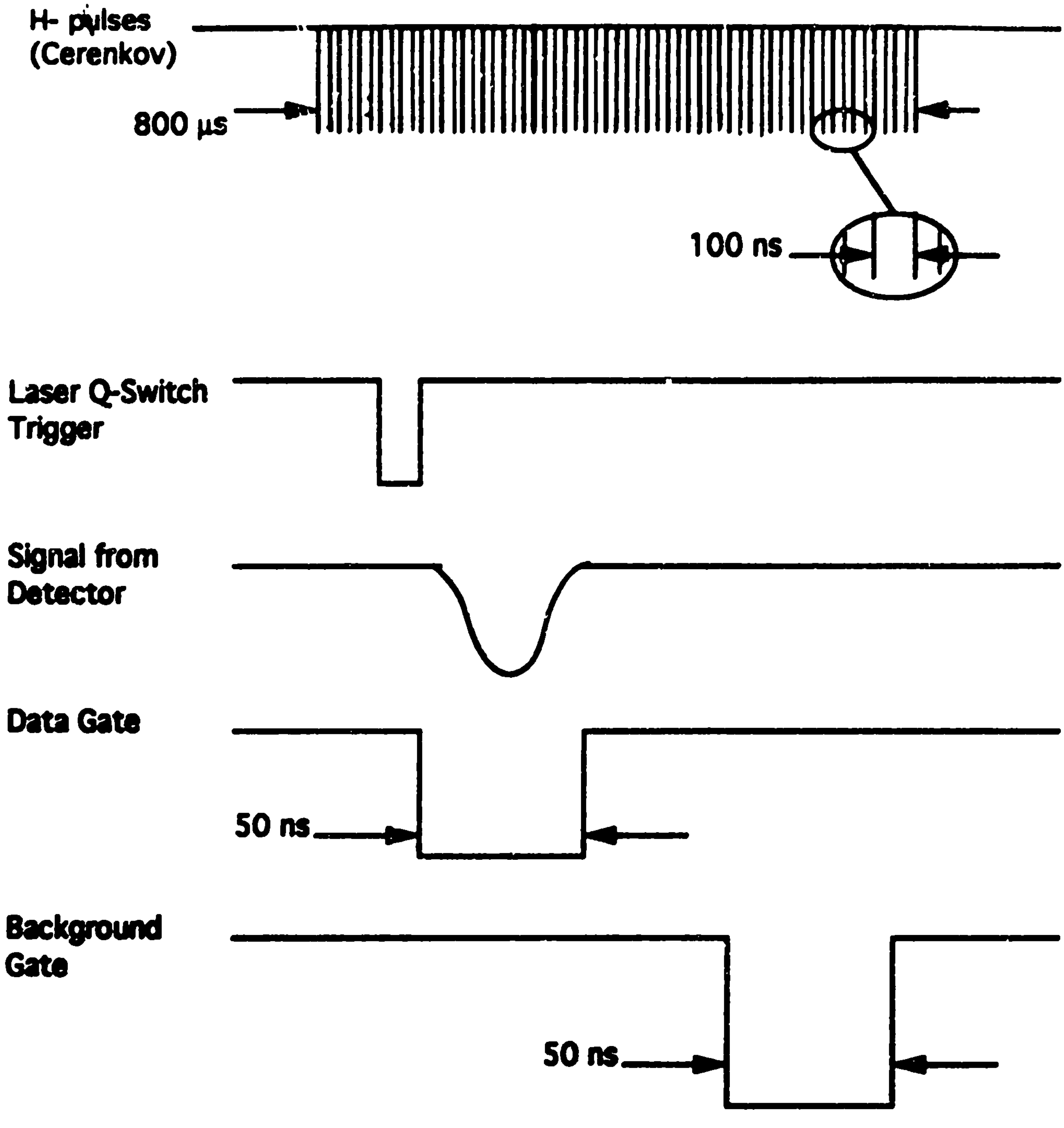

Figure 5.7: Laser event and background timing diagram.

This optimization is more difficult, however, without a friendly beam structure. In the 1990 run, the micropulse separation was 100 ns and the laser pulse duration 9 ns at 10 Hz. Adjusting the laser timing to intercept a micropulse was touchy. Jitter of the laser or any small timing drift can cause a significant signal loss. In the future, 5 ns micropulse spacing would insure that there would always be some overlap of micropulse and laser pulse within a macropulse.

5.2 Software

The event signals acquired by the CAMAC trigger module are stored in a microprogrammable branch driver (MBD) until a software command is given to retrieve the data from the MBD and store it in an array. The "Q" data acquisition code [63] developed at LAMPF was used in this experiment. In this code the data is read into the MBD buffer using "read" (RCn) commands in a file called HIRAB.QAL. From this file different modules are read or written to, depending on which event is specified. The commands are related to typical CAMAC 'FCNA' commands by a database if the particular CAMAC module (specified in the DEVICE command) is contained in the Q database QMODULE.DAT. If not, a 'TFCNA' command is used to perform functions on a module.

Change of laser–ion-beam intersection angle, change and check of spectrometer field, and resetting of the Faraday cup charge counter are a few of the functions performed by the computer system. During a run (begun by the user typing "QRU"), whenever a predetermined amount of charge is reached in the Faraday cup (Event

4), the computer closes the run gate, discontinuing data acquisition. If a laser experiment is in progress (Configuration 1), the intersection angle is then changed in the appropriate chamber via a stepper motor controller, unless the number of angle changes already performed has reached a preset number (100 in this experiment). In that case, the computer signals the user to stop the run by typing "QFI" at the terminal. If a spectrometer scan is in progress (Configuration 2), the field of the spectrometer is stepped after each Event 4, until a preset number of steps is reached. ADCs and TDCs are read after each laser shot and magnetometers are read after each macropulse (Event 9).

The acquired signal data is retrieved from the MBD using the command AGETEV, which stores the data in the specified arrays in the order named in the COMMON/EVENTn/ARRAYS...EOA statement in the PROCn.FOR subroutines.

The Q data acquisition code incorporates many files and subroutines, and can be quite confusing to the user. A detailed description of the data flow may be found in reference [64].

For the 1990 data analysis I modified the code to print "shot-to-shot" information. That is, rather than have just sums or averages of events with pedestals and slopes included, as normally written to the data file, I wanted to examine the raw data of events seen during each laser shot. To this end, I entered a new EQUIVALENCE parameter called SHOT in HIRAB.INC. If SHOT is set to unity by the user, then raw data will be printed to the data file in the subroutine PROC8.FOR. The modified PROC8.FOR is included in Appendix E. The results of this modification are discussed in Section 6.1.

Chapter 6

Data Analysis

6.1 1990 Analysis

The experiment to measure H(n=2) production printed to the data file the number of electrons detached from H(2) per intersection angle. Each run covered 100 angles in step sizes chosen by the user before each run. In our data acquisition system pedestals may be subtracted, and the tendency for the very intense laser to detach electrons from more than one ion taken into account. These functions are accomplished using shared parameters in the dynamic parameter array. The user must input these parameters (pedestal and inverse of slope) in order to see the "correct" count of detached electrons in the on-line histograms. To find these parameters, one must histogram electron counts vs pulse height for the electron spectrometer detector, fit the peaks for at least single-electron and two-electron hits to a Gaussian profile, and fit the peak positions to the polynomial

$$PH(n) = m * n + p \,. \tag{6.1}$$

$PH(n)$ is the pulse height of the peak, n is the peak number (peak number=n for n-electron hits), and p is the pedestal (essentially ADC pedestal). After finding the slope m and pedestal by this fit, they are manually entered in the PRM file. The computer then writes to the data file and histograms the number of electrons detected by calculating

$$n = Nearest\ integer \left[\frac{1}{m}(PH - p)\right] . \tag{6.2}$$

A detailed explanation is given in Reference [64].

As mentioned in the data acquisition chapter, the computer actually acquired the number of electrons per laser shot (≈ 300 laser shots per angle) from the CAMAC modules. The original program used during the experimental run calculated the average number of electrons per laser shot and wrote that value to the data file, so that the file held one value per angle. Similarly, average values were recorded for the detectors whose signals were used for normalization (Čerenkov, fast photodiode signal, etc.). As described in Section 5.2 and Appendix E, I modified the code to output raw data to the data files, so comparisons could be made for each laser shot. The results showed some spurious events (cause unknown) where a value of zero was read from the electron detector ADC. This means that the ADC pedestal was not even recorded. I modified the PROC8.FOR so these events would not be included in the averaged data. In the shot-to-shot data file the pedestal from the ADC port counting real electron-spectrometer events was seen to match that found by fitting the multiple-hit peaks. The ADC pedestal from the address used for background collection was not the same as that used for real event collection. In our case this was not important, as laser-off background was essentially nonexistent in our detection method, but it might be beneficial for future experiments to set all ADC pedestals equal before a run.

6.1.1 Cross Section Calculations

The data from different runs were combined after normalization to H^- beam current and laser intensity. The cross section at each angle α is given by

$$\sigma = GR \frac{\beta \sin \alpha}{IJ(1+\beta \cos \alpha)} , \tag{6.3}$$

where I and J are the H^- and photon currents, and R is the rate of H production. The $\beta \sin \alpha/(1+\beta \cos \alpha)$ factor accounts for the changing CM photon flux and beam overlap with change in angle α. G is a geometrical factor which depends on the spatial and temporal overlaps of the beams. Since we are as yet unable to determine these overlaps in our experiments, G is treated as an arbitrary constant, and cross sections are relative.

The cross sections from runs with the same conditions were combined and binned. For the 1990 shape resonance data, bins are two meV wide. Bins are four meV wide for the $H^{-**}(4)$ data, and the $H^{-**}(3)$ data was unbinned.

6.1.2 Background Subtraction

Although our background-count detectors showed no counts when the laser was not firing, our shape resonance data indicates that we should also have counted background with the laser firing between macropulses. This is evident in the H(N=2) channel data where a non-zero cross section was observed below the n=2 threshold. For these runs, a constant found by fitting to the level below threshold was subtracted from the data.

In subtracting the background for the total shape resonance cross section measurement I made the assumption that the N=2 partial cross section accounts for 75% of the total at a photon energy of 11.1 eV. The theoretical predictions for this ratio are 77% by Broad and Reinhardt, 76% by Sadeghpour *et al*, and 72% by Hyman *et al.* I further assumed that that the background was flat.

For the n=3 and 4 cross sections, background subtraction was not necessary, as only relative cross sections (and not branching ratios) are reported for this energy region.

6.1.3 Energy Calibration and Resolution

For total cross section calibration the energy region of the n=2 Feshbach peak was scanned. In off-line analysis, energies were calibrated to this narrow peak whose energy is well known from experiment [23]. Since the profile is effectively a delta function ($\Gamma \approx 30$ μeV) [58], its observed width demonstrates our energy resolution of 0.007±0.001 eV (Figure 6.1). For partial decay cross sections, calibration was to the

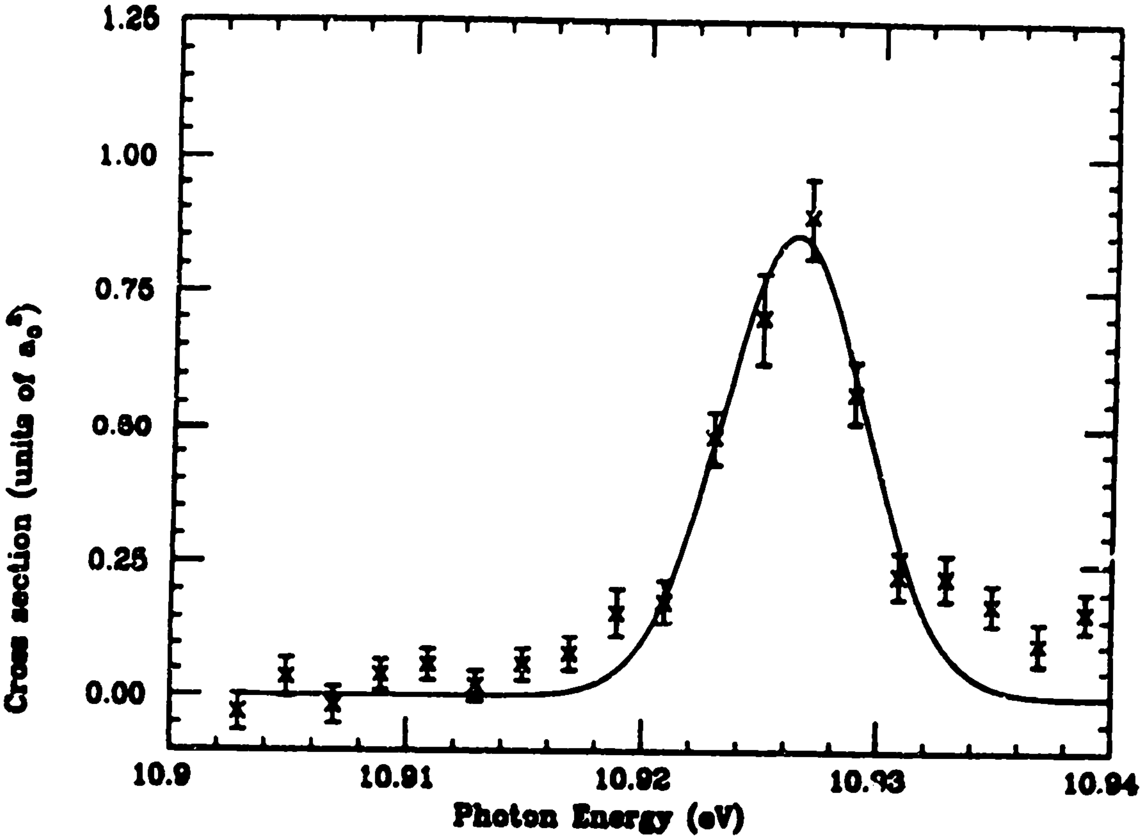

Figure 6.1: The width of the $n=2$ Feshbach resonance defined our experimental resolution.

H(N=2) threshold at 10.953 eV.

6.1.4 Fitting the Data

All fits were convoluted with a Gaussian function to correct for experimental resolution.

$H^{-**}(n=3$ and $4)$ Fits

These resonances were fit to the Fano function (Eqn. 1.6)—the usual procedure for Feshbach-type resonances. The results are displayed in Section 7.1.

$H^{-**}(n=2)$ Shape Resonance Fits

In order to establish the width, central energy, and asymmetry of the shape resonance, a function is needed which coincides well with the experimental data. Traditionally the function formulated by Fano (Eqn. 1.6) has been used to fit the observed H^- resonant cross sections. The formulation requires, however, that parameters such as width Γ and asymmetry q be constants with respect to energy across the width of the resonance. This may not be the case for the shape resonance.

Other functions have been suggested whose parameters from MINUIT [65] fits are listed in Table 7.2 along with the Fano parameters. Broad [66] suggested letting that part of the continuum (σ_a) which interacts with the resonance vary linearly with energy across the range of the fit. Thus I replaced σ_a in (1.6) by $\sigma_a + \epsilon(\partial\sigma_a/\partial\epsilon)$ with $(\partial\sigma_a/\partial\epsilon)$ as an extra fitting parameter. The results of fitting to this form are listed in the table as Fit "B".

I also tried the extension of the Fano-type treatment proposed by Starace [29] to fit partial decay cross sections in the vicinity of a resonance. In this approach a new complex variable $\alpha(\mu E)$ is introduced to account for the boundary condition satisfied by the wave function for an outgoing electron in a particular observable channel μ. The fit using equation (26) of reference [29] incorporates two new parameters, the imaginary and real parts of α, in addition to the regular Fano parameters. As with the usual Fano function, however, this form is actually meant to be applied to narrower resonances whose parameters have no energy dependence.

Part of the difficulty in fitting to these functions may be that the low energy shoulder of the shape resonance lies on the threshold for production of H(2). I therefore tried fitting to a cross section formula that is a product of the Wigner threshold law and the usual Breit-Wigner resonance formula, as suggested by Peterson [67]. Neither the partial nor the total shape resonance cross section is a good fit to this function ($\chi^2/\nu \geq 10$). A variation of width with energy, or the $n=2$ Feshbach resonance lying very near threshold, may explain the poor correspondence of our data with this formulation.

6.1.5 Systematic Errors

The H(2) detection scheme is flawed in that the angular momentum content of the observed H(2) atoms is not well characterized. That is, we don't know how many of those arriving at the electron spectrometer are in the 2*s* state and how many in 2*p*—for two reasons.

First, the promotion chamber is located 27.75 inches downstream from the laser-H^- interaction chamber. This means that, in the frame of the moving atom, 1.5 ns elapses before it reaches the second laser. The lifetime of the $H(2p)$ state is only 1.6 ns, so that approximately 60% of the $H(2p)$ atoms decay to $H(1s)$ before reaching the promotion region. Second, a stray field in the lab could cause Stark mixing of the $2s$ and $2p$ levels. The *maximum* laboratory field possible along the flight path is estimated to have been one gauss (an electric field of ≈ 470 V/cm in the CM frame of the atoms and ions). Given this field strength and assuming dipole oscillations only, the probability that a $2s_{1/2}$ ($2p_{1/2}$) atom leaving the interaction region will still be in the same state after traveling 28 inches was calculated to be 0.51 (0.36). Regarding the transition probabilities in the second interaction region, the fraction of $2s$ atoms promoted to the N′ state by the second laser is equal (±5%) to the fraction of $2p$ atoms promoted [2], and small differences here may be disregarded.

Since I report relative cross sections only, the above effects would not be problematic if the $2s$ and $2p$ profiles had exactly the same shape. According to calculations of Sadeghpour [68] and Callaway [69], however, the shape resonance cross sections probably differ above about 11 eV, with the $2s$ cross section falling off faster than the $2p$. Figure 6.2 shows $2s$ and $2p$ profiles for the $H^{-**}(2)\ {}^1P^o$ shape resonance from R-matrix calculations of H. R. Sadeghpour for photodetachment [47] and variational calculations of Callaway for electron impact excitation [69]. The $2s$ profile has been normalized to the $2p$ cross section at its peak in both cases to emphasize the comparative drop-off in the high energy region.. For that reason, the

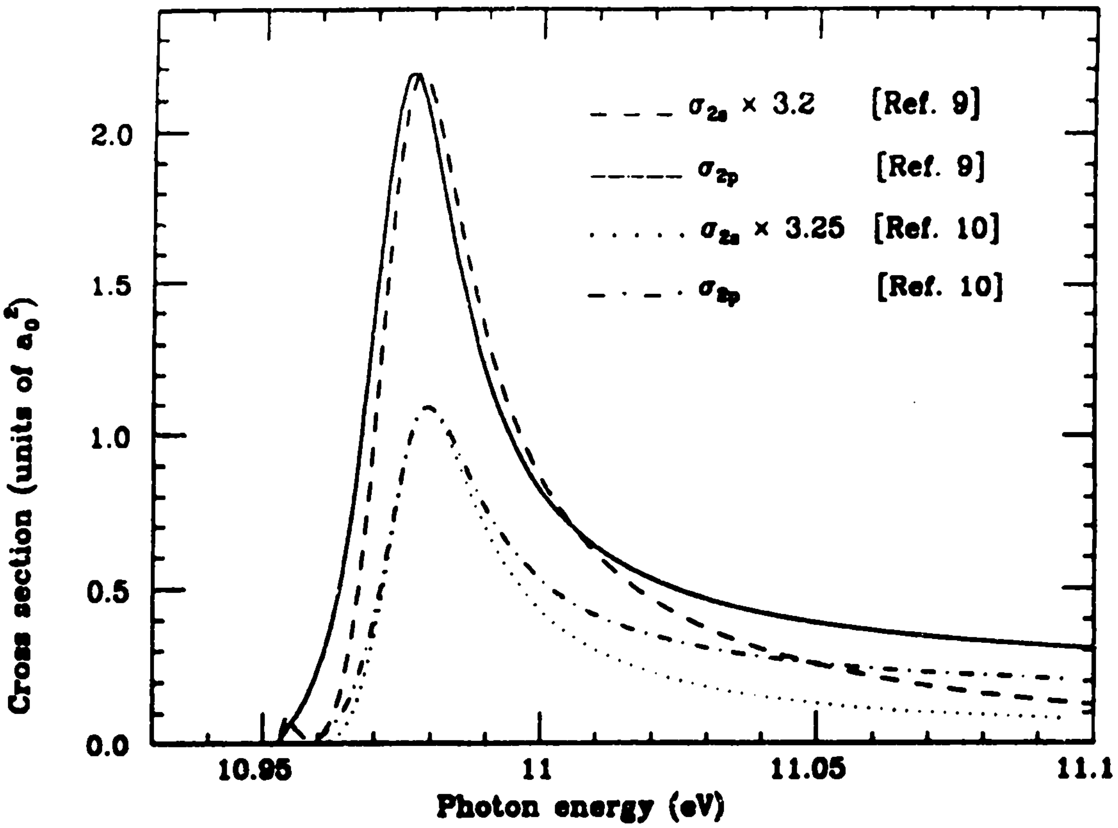

Figure 6.2: 2*s* and 2*p* profiles for the $H^{-**}(2)\ {}^1P^o$ shape resonance.

experimental cross sections and branching ratios below this energy are considered more reliable than those above it.

Theoretical partial cross sections for $H^{-**}(3)$ and $H^{-**}(4)$ to decay to either $2s$ or $2p$ are unavailable. These resonances are much narrower than the shape resonance, however. Since the shape resonance $2s$ and $2p$ profiles have the same contour up to about 25 meV above the central energy, I speculate that, over the narrow region of the $n=3$ and 4 Feshbach resonances, the $2s$ and $2p$ profiles may hold the same shape. It should be stressed, though, that I know of no other justification for this assumption.

Other possible systematic errors such as fluctuations in the ion beam energy and slipping of the encoder belt, which could induce error in the intersection angle α, have been assumed negligible when compared with statistical error.

6.2 1989 Analysis

Cross sections for each 1989 run were calculated by Harris [57]. Energy calibration was accomplished by monitoring laser-effected transitions between excited states of neutral hydrogen [26]. 1989 experimental resolution was determined from the width of the hydrogen lines to be 0.008 eV. I combined the runs, binned the data in two-meV-wide bins, and fitted the cross sections to the appropriate functions.

6.2.1 Fitting the Data

The $n = 4$, 5, and 6 zero-field thresholds were fit to a step function (See Section 2.3) with three parameters: E_0, B, and C, where E_0 is the threshold energy, B the cross section below threshold, and C the cross section above threshold. Results are shown in Chapter 7.

The changing shape of the cross section in response to a field made it impossible to ascertain the photon energy for the onset of production by fitting the applied-field data to any known function. Therefore, each field-induced threshold energy was chosen to be where the cross section is 13% of its value at 40 meV above the zero-field threshold. The 13% level was selected because it gives values which are consistent with theoretical zero-field thresholds. The reference energy 40 meV above zero-field threshold was chosen in order to avoid field-generated structure. The error in this method was assumed to be ±5 meV—probably an overestimate, as noted in the following chapter.

The Feshbach resonances were fit to the Fano function (Eqn. 1.6) and the parameters compared from fits to data taken at different field strengths. Field-induced asymmetries were examined in the light of Stark-mixing. Results are shown in the next chapter.

Chapter 7

Results and Conclusions

7.1 Partial Decay into H(2) by Excited H^- near the n=3 and 4 Thresholds

Two resonances in the photodetachment spectrum of H^-, one just below the n=3 threshold and the other just below the n=4 threshold, were observed decaying into H(N=2) + e.

The resonance profiles (cross-sections vs. photon energy) were fit to a Fano function [7], giving central energies of 12.652±.003 eV for $H^{-**}(3)$ and 13.338±.004 eV for $H^{-**}(4)$. Positions and widths are in good agreement with recent R-matrix calculations by Sadeghpour, Greene, and Cavagnero [1] (Figures 7.1, 7.2, and 7.3) as well as other theoretical calculations. Table 7.1 compares the experimental parameters with theoretical predictions. E_0 is the central energy, q is the asymmetry parameter, and Γ the width.

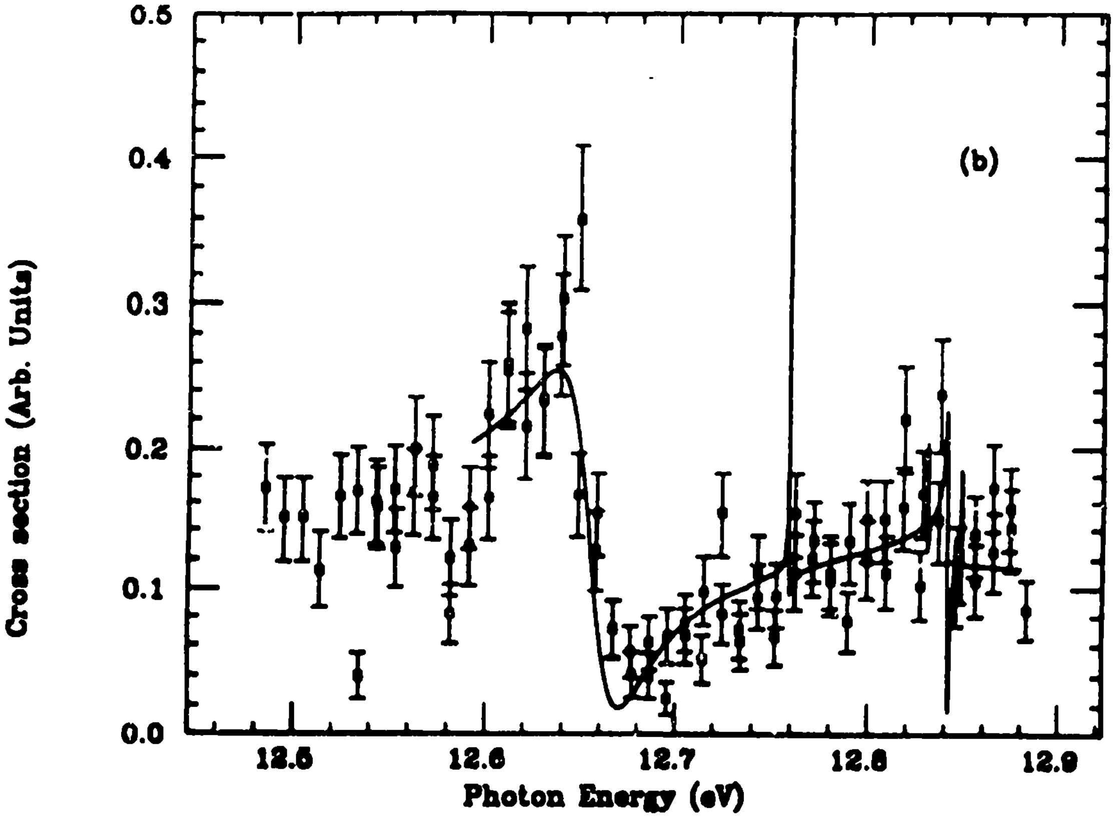

Figure 7.1: The lowest $H^{-**}(3)$ resonance, observed in the H(2) continuum.

Table 7.1: Predicted and experimental Fano line-shape parameters for the first resonances near $n=3$ and $n=4$ thresholds.

n	Parameter	Theory	This Exp't.
3	E_0(eV)	12.6494[27], 12.6605[71], 12.6623[72]	12.652 ± .003
	Γ(eV)	0.0325[73], 0.0316[50]	0.030 ± .003
	q		-1.6 ± .2
4	E_0	13.3448[27], 13.3502[71], 13.3435[72]	13.338 ± .004
	Γ	0.0275[50], 0.0339[51]	0.015 ± .006
	q		0.7 ± .3

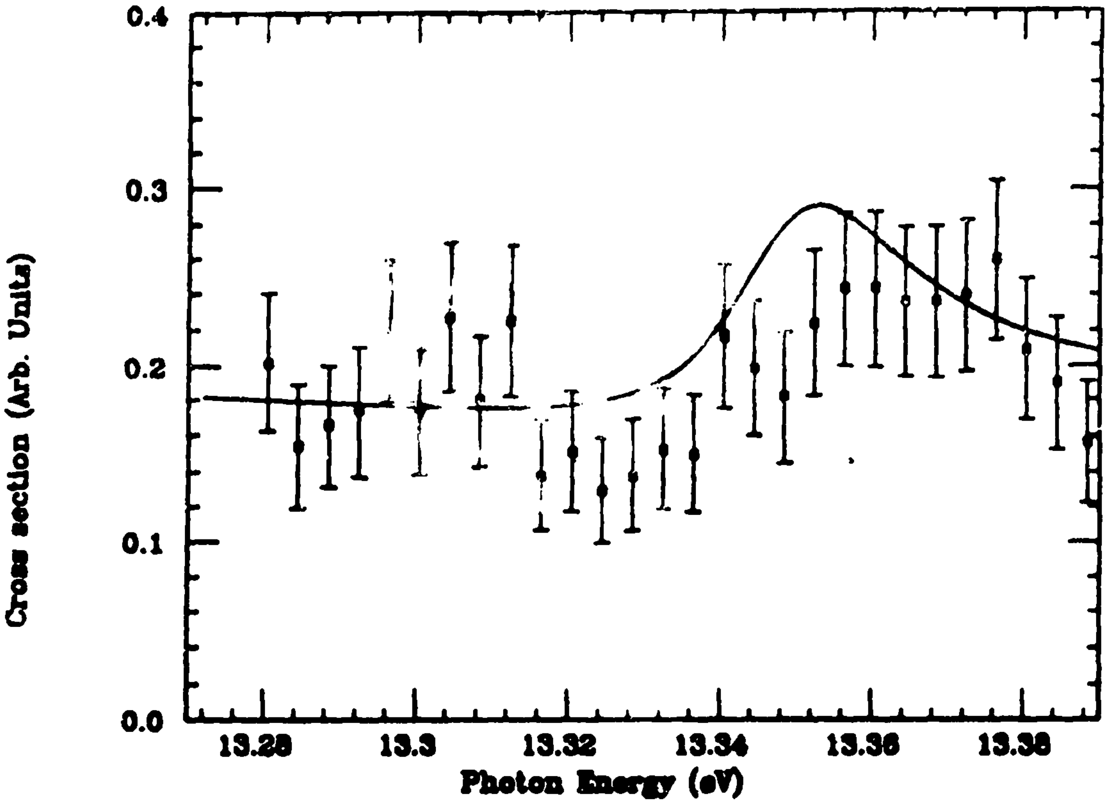

Figure 7.2: The lowest $H^{-**}(4)$ resonance, observed in the $H(2)$ continuum.

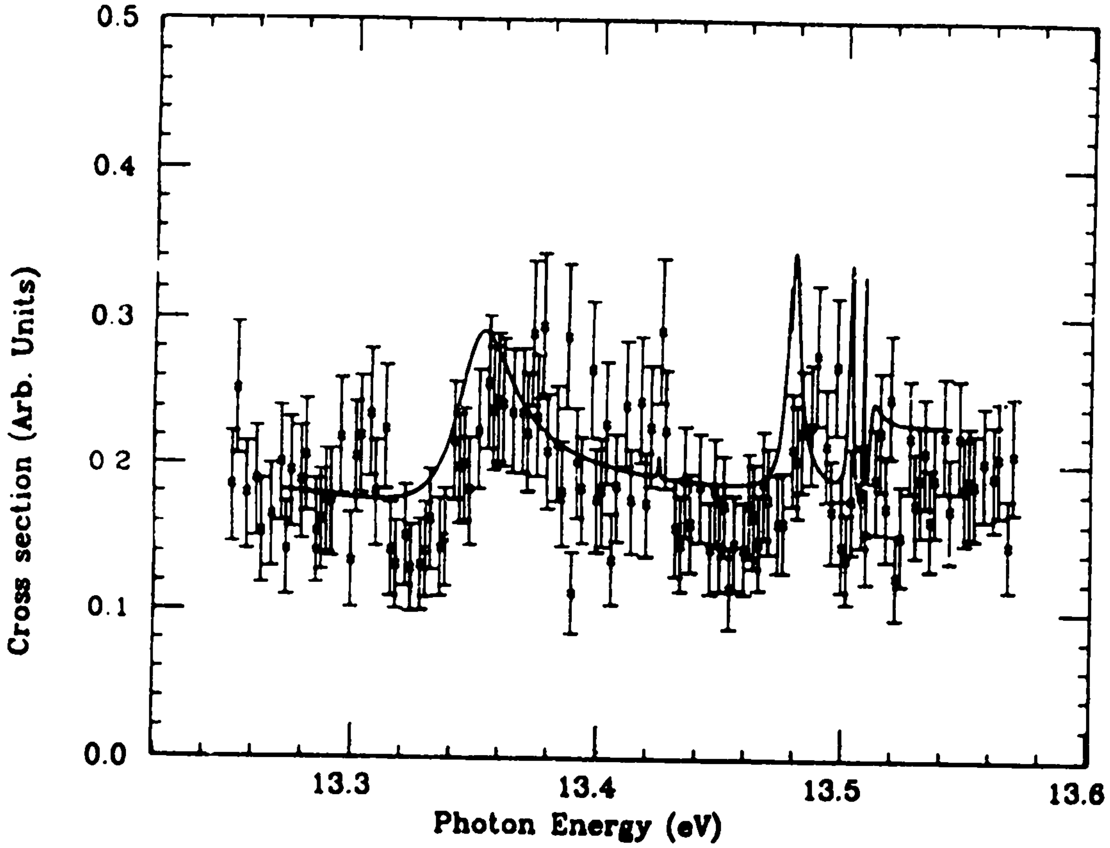

Figure 7.3: **Entire $H^{-**}(4)$ resonance region measured in H(2) channel compared with R-matrix theory [1].**

In particular we note that the line-profile asymmetry for the $n=4$ resonance is as predicted in reference [1] (Figure 7.2). That is, in the profile of the $n=4$ resonance the dip occurs at a lower energy than the peak, whereas the $n=3$ profile is just the opposite. Theoretical cross sections for decay to each continuum are shown in Figure 7.4 for $n=4$.

Figure 7.5 shows that the $n=3$ peak is enhanced over the dip in this channel, which is not the case in previous total cross-section measurements [70]. The magnitude of the line profile parameter q for the $n=2$ channel is more than twice that for total decay and the peak-to-valley amplitude is about $1\frac{1}{2}$ times as large, indicating that the channel is preferred (effective strength $\propto q^2 + 1$). Figure 7.6 displays theoretical cross sections for individual continuum channels. Note the difference in asymmetry between profiles for decay to N=1 and N=2. When adding to get the total cross section profile, the dip in N=1 partially cancels the peak in N=2, resulting in a smaller amplitude for the total cross section profile. (The narrow peak near 12.752 eV in the theoretical cross section is a long-lived '−' resonance with a FWHM of about 0.25 meV. We are unable to resolve this peak under current experimental conditions.) As the first experimental evidence of such preferential autoioniztion channel-selection, this work has been cited by Rau as partial justification for his analogy between quark families and H^- family-type groupings [74].

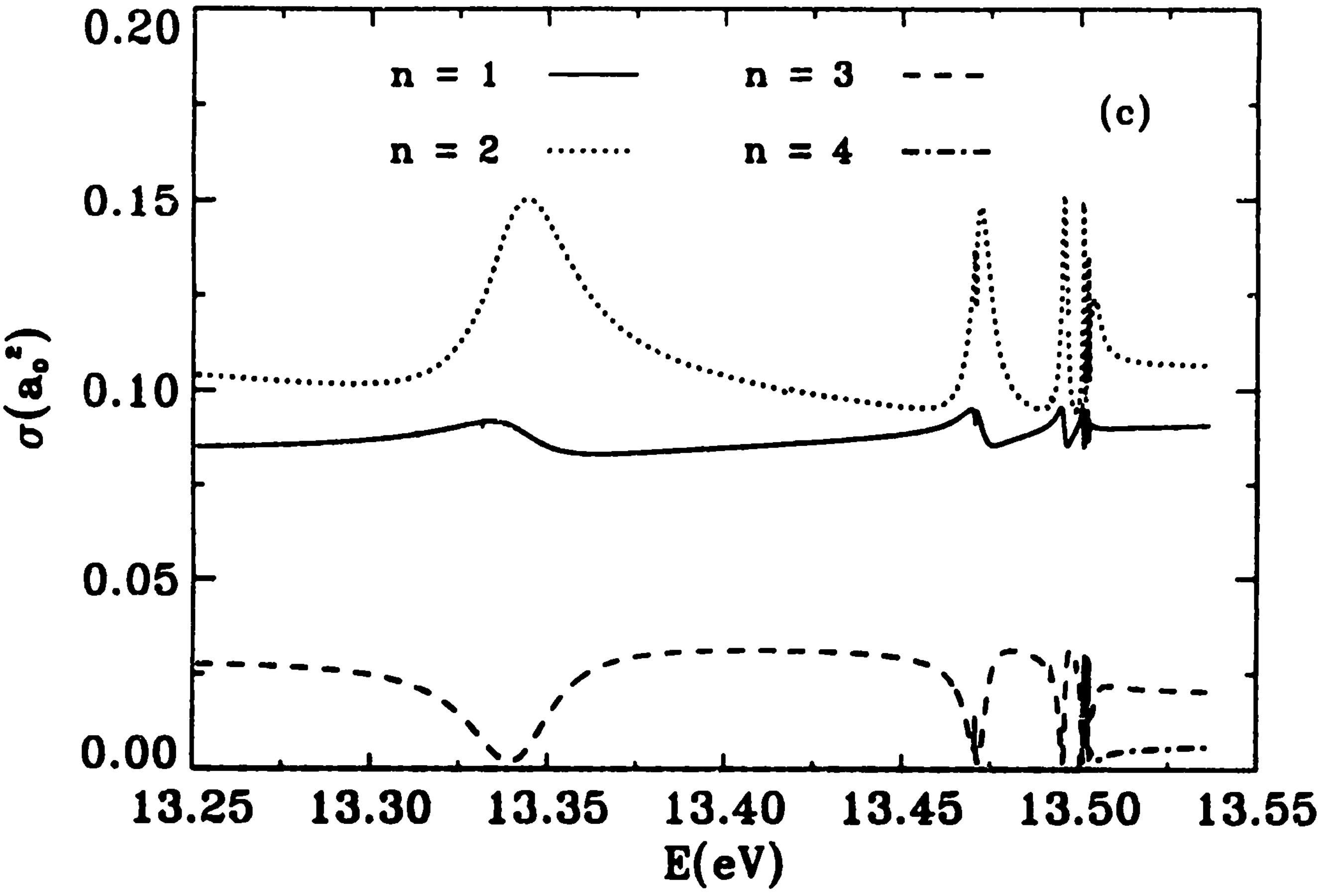

Figure 7.4: R-matrix theory partial cross sections for the production of individual states of hydrogen at energies near the n=4 threshold [1].

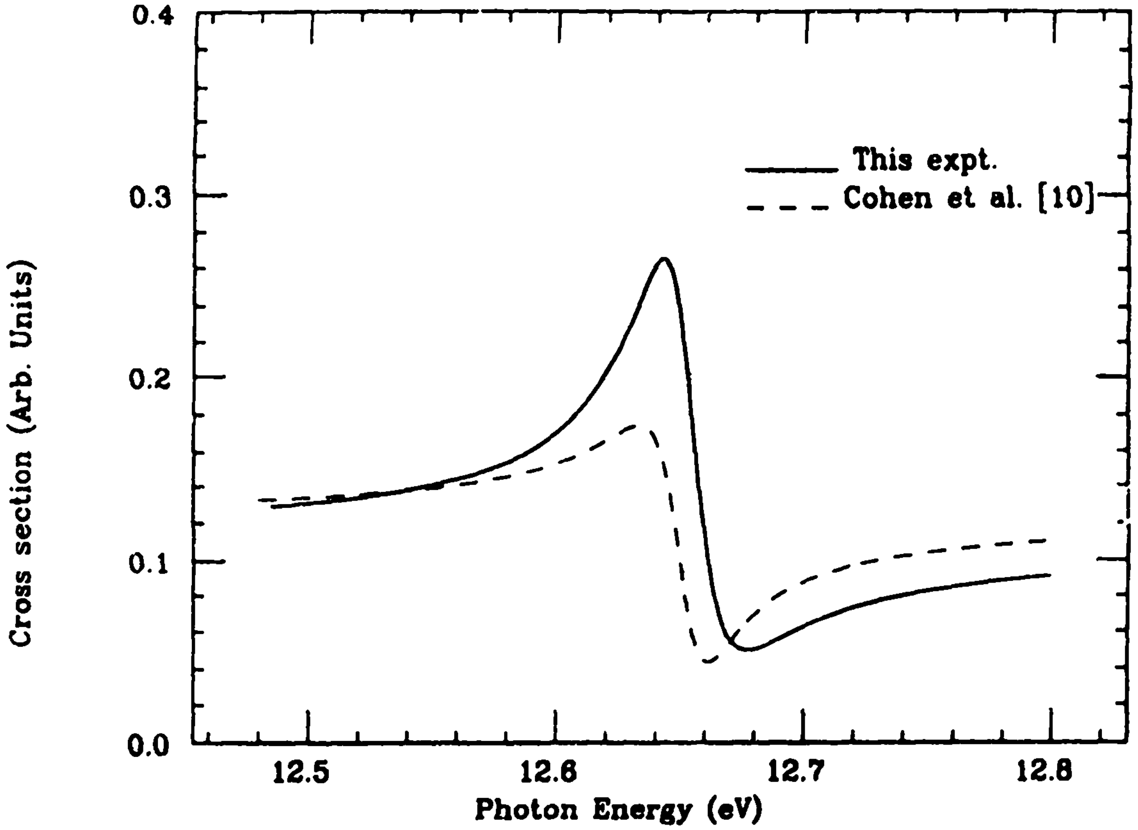

Figure 7.5: **Comparison of Fano lineshapes for total decay channel (dashed line) and $n=2$ decay channel (solid line). Continuum levels on left have been matched to aid the eye in profile comparison.**

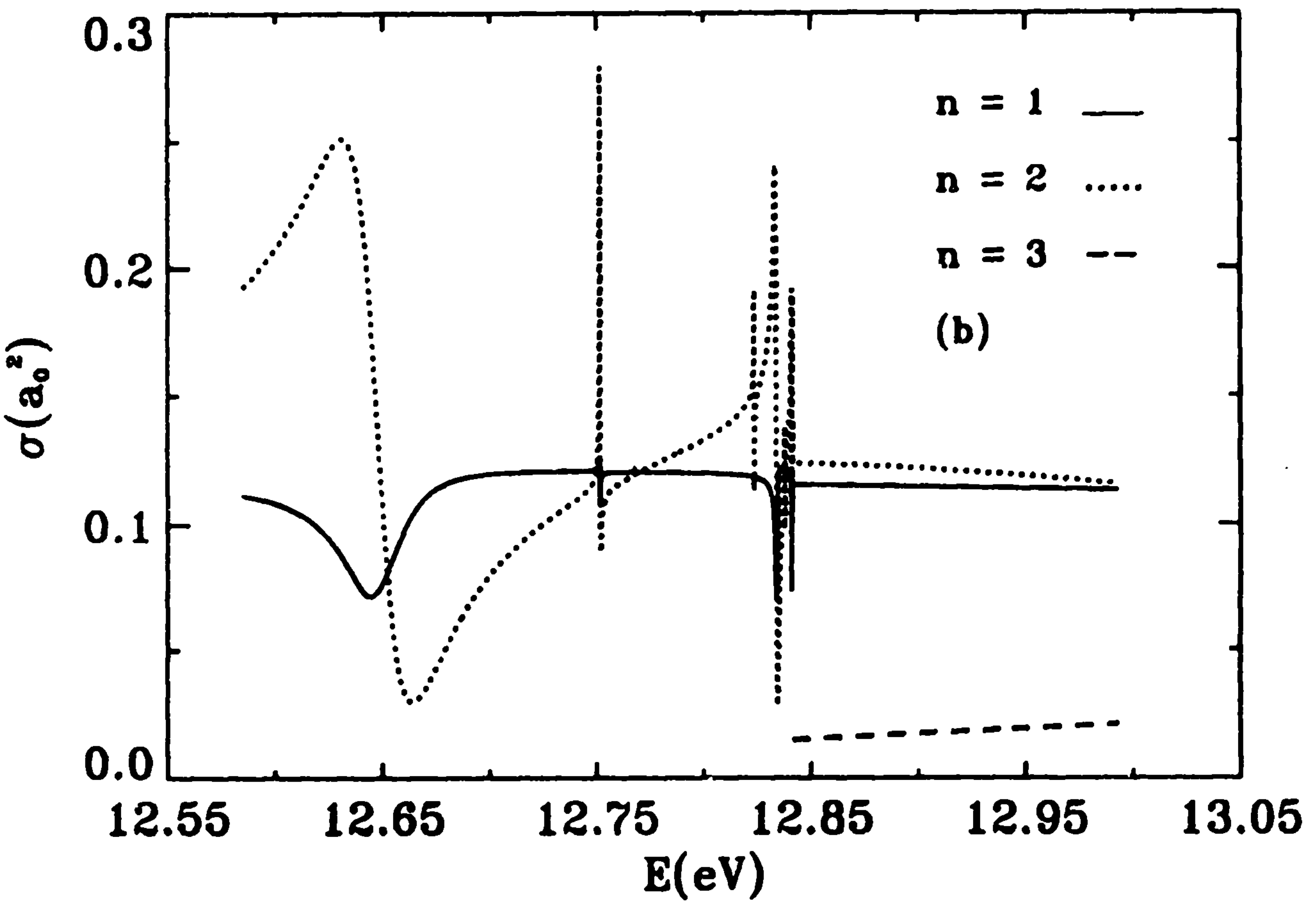

Figure 7.6: R-matrix theory partial cross sections for the production of individual states of hydrogen at energies near the $n=3$ threshold [1].

7.2 Shape Resonance Branching Ratio Measurement

Here I report measurements of relative cross sections for total decay of the $H^{-**}(n=2)$ shape resonance and for its partial decay into the H(N=2) channel. I normalized these cross sections to theoretical peak values to arrive at branching ratio values. Various functions were fit to the shape resonance total and partial cross section profiles (as described in Chapter 6). The fitted parameters are listed in Table 7.2 where "F" indicates a fit to the Fano function. "B" indicates a fit to Broad's modification [66] of the Fano function. "S" indicates a fit to Starace's modifications [29] of the Fano function. The error in the parameter value, as assigned by our fitting program MINUIT [65], is the deviation from the best fit value of the parameter that would increase its χ^2 value by one. All fits were convoluted with a Gaussian function to correct for experimental resolution. The MINUIT error in Γ is combined with that induced by the error in the experimental resolution.

In the fits to the total cross section, the original Fano function follows the profile of the data more closely than the function with Broad's energy dependent background adjustment, as evidenced by the values of the reduced chi-squared χ^2/ν in Table 7.2. χ^2 is a measure of the spread of the observations divided by a measure of the expected spread. The number of degrees of freedom ν is the number of data points minus the number of fit parameters. χ^2/ν should be approximately unity if the data fits the function well. χ^2/ν less than one indicates that error bars have been overestimated [75]. For the partial decay cross section, the goodness-of-fit is about the same for the three functional forms we tried.

I also made fits to 1983 data of Butterfield [25] (*b* superscript in Table 7.2). The fit to the partial cross section was better for the 1983 profile because more data was taken in that year. The parameters found from fits to the 1983 data show some dependence on the high-energy cutoff value of the fit, while the 1990 data do not.

While the fits to the shape resonance partial cross section profiles indicate similar widths for the 1983 and 1990 data, one can see in Figure 7.8, for example, that they are in fact quite different. The fitting program actually adjusts the width Γ and the background parameter σ_a at the same time. (The internal covariance matrix correlation coefficient between these two parameters was greater than 0.5 for all partial cross section fits.) The higher shoulder on the 1983 data seems to have a strong effect on the width obtained by the fit. Therefore, I also report the full width at half maximum (FWHM). with a base of zero for the N=2 partial cross section, the FWHM is 22.1 $^{+2.5}_{-1.8}$ meV (32.1 ± 2.1 meV) for the 1990 (1983) data. For the total cross section the base of the resonance was chosen to be the minimum cross sectional value between the Feshbach resonance and the shape resonance, at about 10.94 eV. This choice gives a FWHM of 23.2 ± 2.0 meV for the 1990 data and 32.9 $^{+1.3}_{-0.6}$ meV for the 1983 data.

Since no two theories have similar predictions for the width, central energy, or amplitude of the resonance (Figure 7.7), and definitions of "width" are vague at best, the comparisons of theoretical profiles with our data are shown in separate figures, normalizing experimental peak amplitudes to theory. In some cases the theoretical energy was shifted downward in order to make profile comparisons.

Decay Channel	Fit	Γ(meV)	E_0(eV)	q	χ^2/ν
Total	F	21 ± 1^a, 30 ± 1^b	10.974 ± 0.0003^a, 10.970 ± 0.0003^b	5.3 ± 0.2^a, 4.5 ± 0.1^b	2.6^a, 2.5^b
	B	20 ± 1^a, 33 ± 1^b	10.974 ± 0.0003^a, 10.970 ± 0.0002^b	4.6 ± 0.1^a, 4.2 ± 0.1^b	3.6^a, 4.1^b
H(2) Partial	F	20 ± 1^a, 22 ± 1^b	10.974 ± 0.0003^a, 10.972 ± 0.0001^b	4.2 ± 0.1^a, 2.7 ± 0.1^b	5.3^a, 2.6^b
	B	22 ± 1^a, 22 ± 1^b	10.973 ± 0.0003, 10.972 ± 0.0001^b	3.5 ± 0.1^a, 2.7 ± 0.1^b	4.6^a, 2.7^b
	S	20 ± 1^a, 22 ± 1^b	10.974 ± 0.0002^a, 10.972 ± 0.0001^b	4.3 ± 0.1^a, 2.5 ± 0.1^b	5.6^a, 3.0^b

Table 7.2: Widths Γ, central energies E_0, asymmetries q, and reduced chi-squared values χ^2/ν from Fano fits to total and partial cross sections. (a) 1990 data. (b) 1983 data.

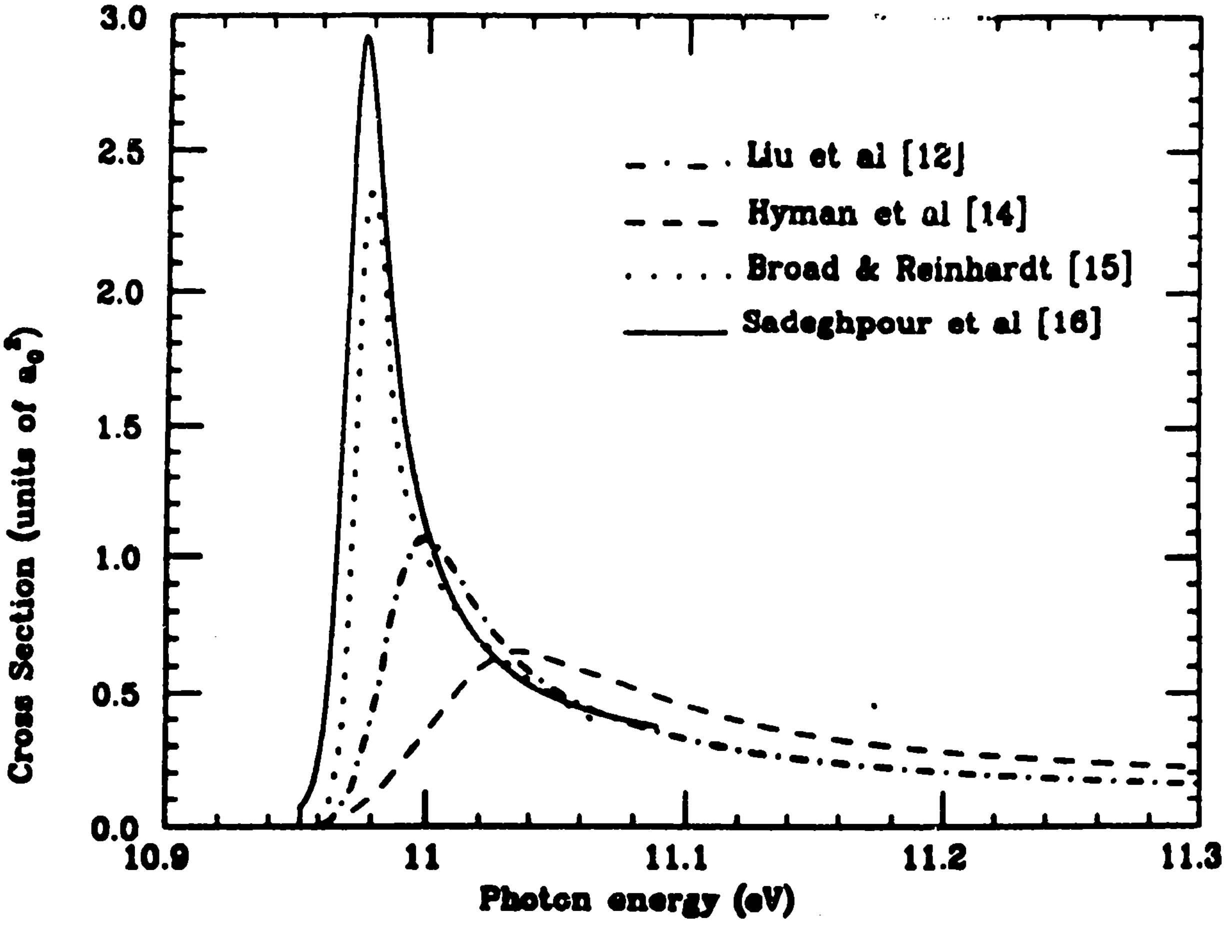

Figure 7.7: Theoretical photodetachment partial cross section vs energy above the threshold for production of H(2) plus a free electron.

7.2.1 $H^{-**}(2) \rightarrow H(2)$ Partial Cross Section

Figure 7.8(a) is a plot of our partial cross section data compared to a profile calculated by Liu *et al* [38] within an adiabatic hyperspherical representation in which electron correlations are described in terms of the surface harmonics at a constant hyperradius [76]. For this figure the theoretical curve has been shifted down in energy as it predicts the shape resonance 18.9 meV too high.

Figure 7.8 (b) shows a comparison with a $1s-2s-2p$ close coupling calculation of Hyman *et al* [35] using Hyleraas bound state wavefunctions. This profile has been shifted downward in energy so that the onset of production appears at 10.953 eV. One of the earliest, this calculation predicted the resonance to be much wider than experiment shows.

In Figure 7.9 (a) our data is compared with the multichannel J-matrix calculation of Broad and Reinhardt [36]. Their method solves the pseudostate close coupling equations for H^- photodetachment using standard configuration interaction methods and square integrable (L^2) basis functions. Their choice of scale parameter ξ=0.5 obtains reasonable values for the width and energy of the shape resonance, and no energy adjustment was necessary.

Figure 7.9(b) is a comparison with a profile resulting from a recent eigenchannel R-matrix calculation which incorporates an analytic description of electron motion in a dipole field [1]. For this figure we have made no shift in energy. To our knowledge, this prediction of Sadeghpour *et al* derives from the only *ab initio* calculation for partial and total cross sections to date. The energy and width are in

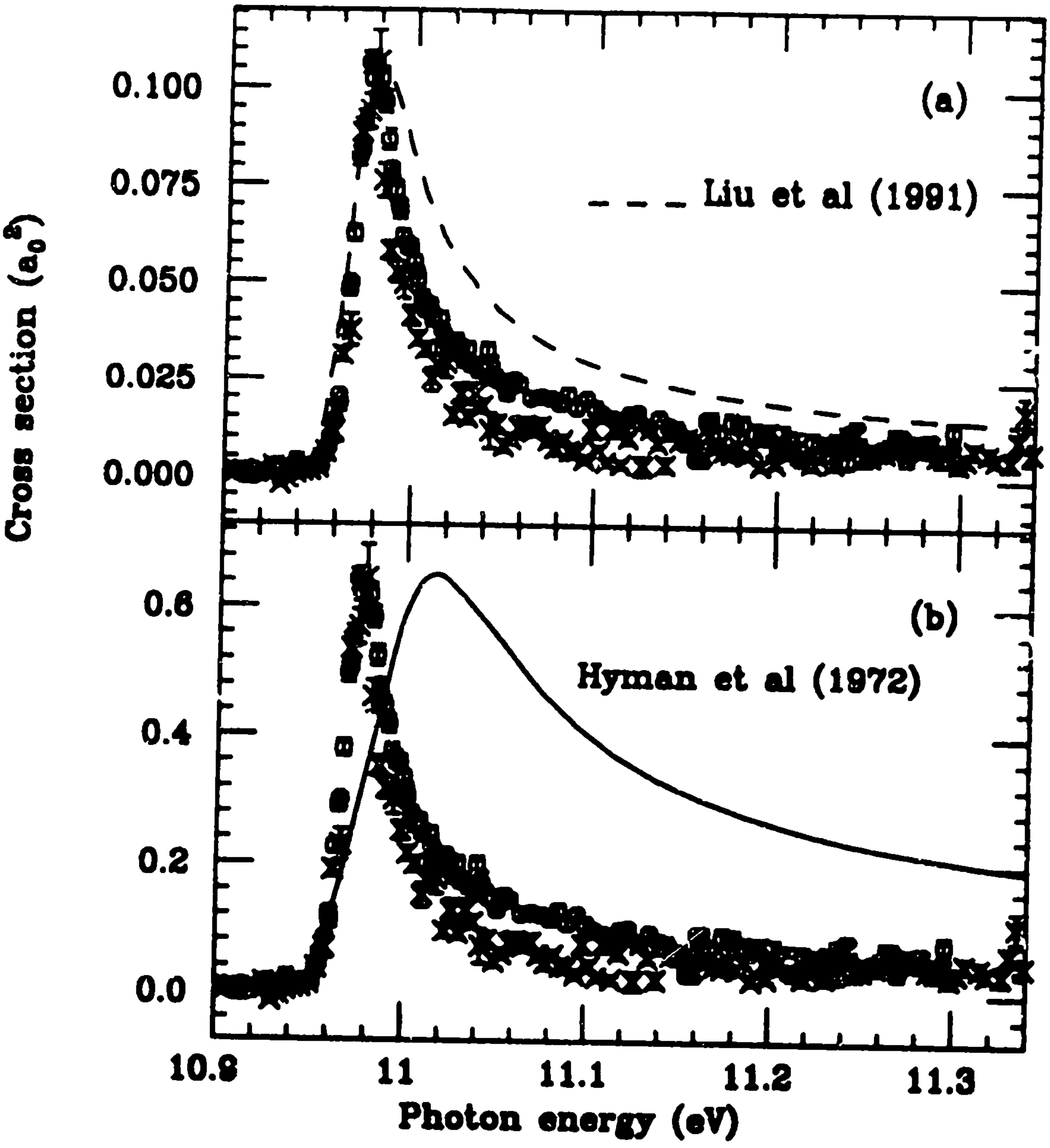

Figure 7.8: $H^{-**}(2) \rightarrow H(2)$ partial cross section vs photon energy. Open circles, 1983 data. Crosses, 1990. (a) Our data vs theory of Liu *et al* (b) Hyman *et al*.

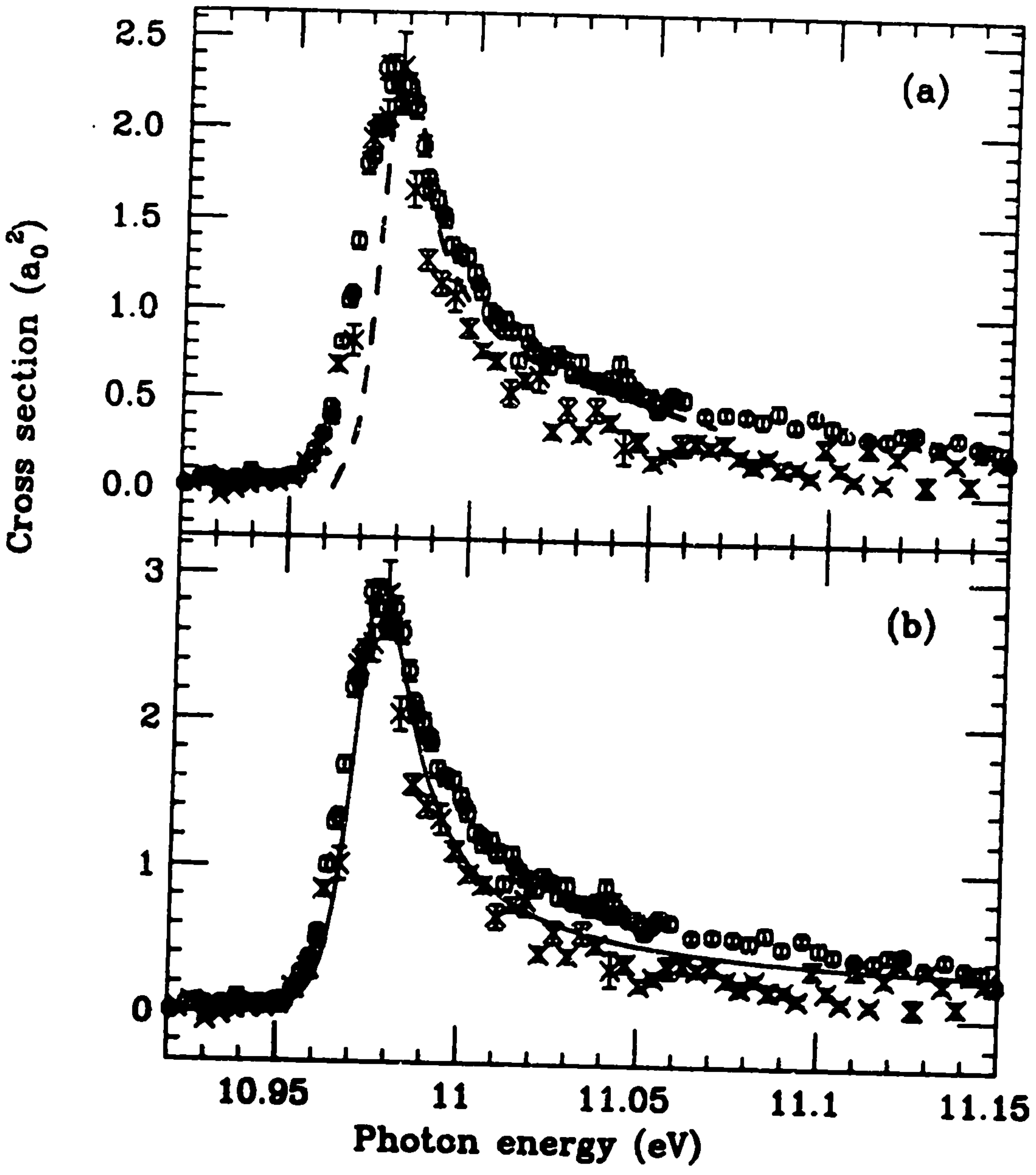

Figure 7.9: $H^{-**}(2) \rightarrow H(2)$ partial cross section vs photon energy. Open circles, 1983 data. Crosses, 1990. (a) theory of Broad and Reinhardt, (b) Sadeghpour *et al.*

good agreement with experiment.

7.2.2 The Shape Resonance Total Cross Section

The total cross section in the region of the shape resonance has previously been measured by this group, compared with theory, and reported elsewhere [77]. Therefore, in this analysis the focus is only on total cross sections from theories which have made predictions for both the total and partial decay channels. These are plotted against our data in Figure 7.10. The narrow Feshbach resonance below threshold is evident near 10.93 eV. Error bars are statistical only. The cross section was normalized to theory at the peak amplitude in each case. We note that Hyman *et al* [35] and Wishart [37] also calculated the total cross section, but their profiles are not displayed, as they predicted Γ to be much larger than the other theoretically calculated widths and the experimentally observed width.

There is an obvious discrepancy between the widths measured in different years. While stray fields in the lab could cause a slight narrowing of the shape resonance (Comtet *et al*, Ref. [77]), we are confident that these did not exceed one gauss. Fields of this magnitude should not be strong enough to cause an observable effect. Comparisons of relative amplitudes and laser intensities have led us to rule out saturation of the reaction as a possible cause for the broader measurement, but other unknown systematic errors must be contributing. A test of the shape resonance parameters as a function of laser intensity has never been done, however. It is possible that the intensity may affect the lifetime, which is so short that the resonance decays

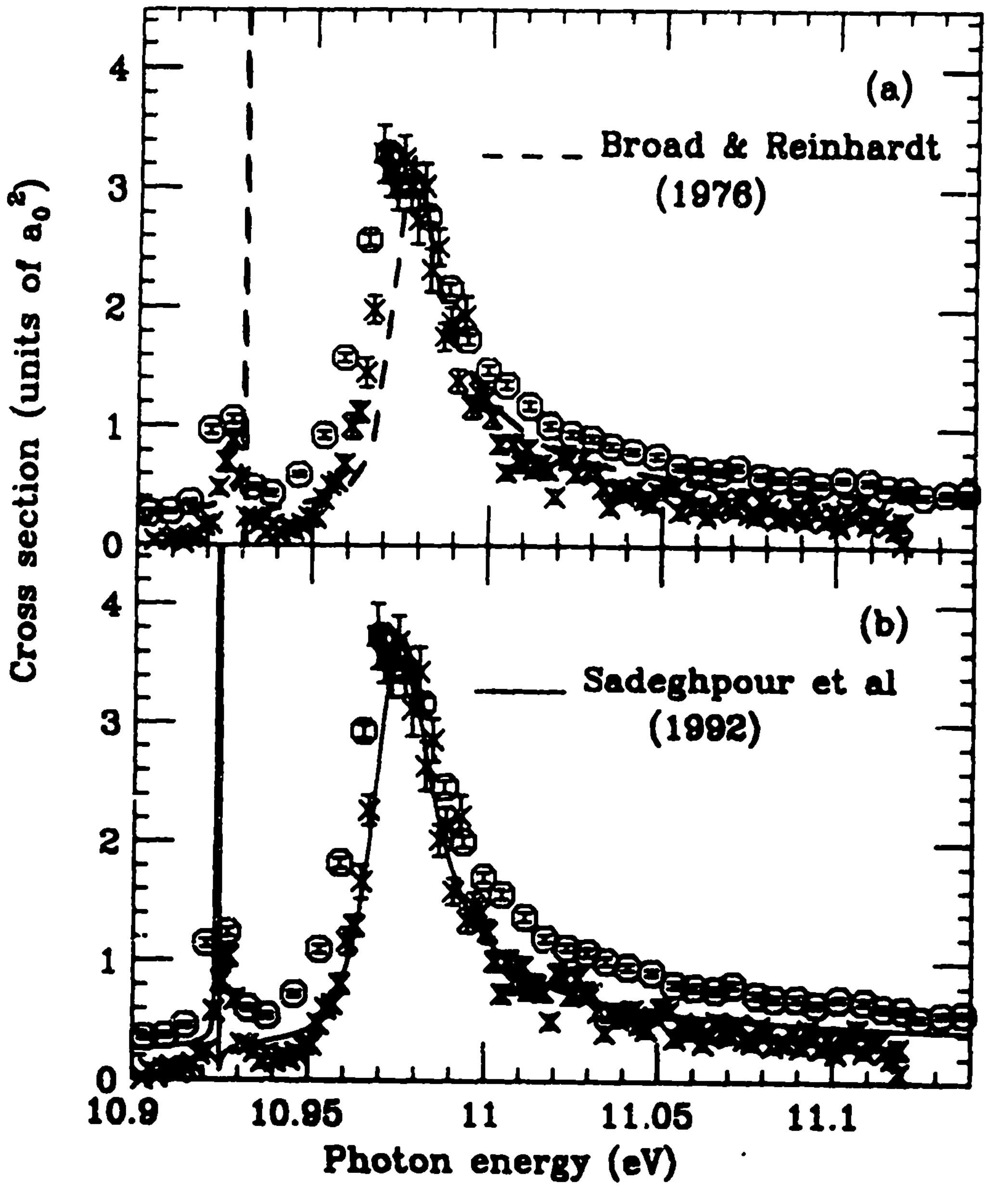

Figure 7.10: Photodetachment total cross section vs photon energy near the $n=2$ threshold. Open circles, 1983. Crosses, 1990. (a) Theory of reference [36]. (b) Theory of reference [1].

before leaving the laser field. In 1990 the CM laser intensity was about $6(10^7)$ while in 1983 it was about 10^8. This possible dependence should be investigated in a future experiment.

7.2.3 The Branching Ratio

The branching ratio reported here, $\sigma(2)/\sigma(Total)$, is that fraction of the total shape resonance decaying to H(N=2). I computed this ratio for 45 photon energies, ranging from 10.95 to 11.30 eV, by binning the data into bins seven meV wide and dividing by bin. Error bars are statistical only. Our data normalized to reference [36] give branching ratios only slightly different from those normalized to reference [1]. Both cases are shown in Figure 7.11. The maximum branching ratio (≈0.8) is approximately 20 meV above the central energy of the resonance. Experiment appears to be in good agreement with theory below about 11.1 eV. As discussed in Chapter 6, we have less confidence in experimental values above this energy.

7.3 Field-Induced Structure and Threshold Shifts

The H(4) partial cross section measurement was performed in CM field strengths of 0, 13, 25, 38, 63, and 87 kV/cm [78]. The data are displayed in Figures 7.12 to 7.14. Notice the trend with increasing electric field. Most notable is the large shift of the threshold toward lower energies. Figures 7.15 shows the data for H(5) production in 0 to 75 kV/cm fields. H(6) yield was examined in only three field strengths, 0, 13, and 25 kV/cm (Figure 7.18). The threshold shifts to lower energies as it does in the

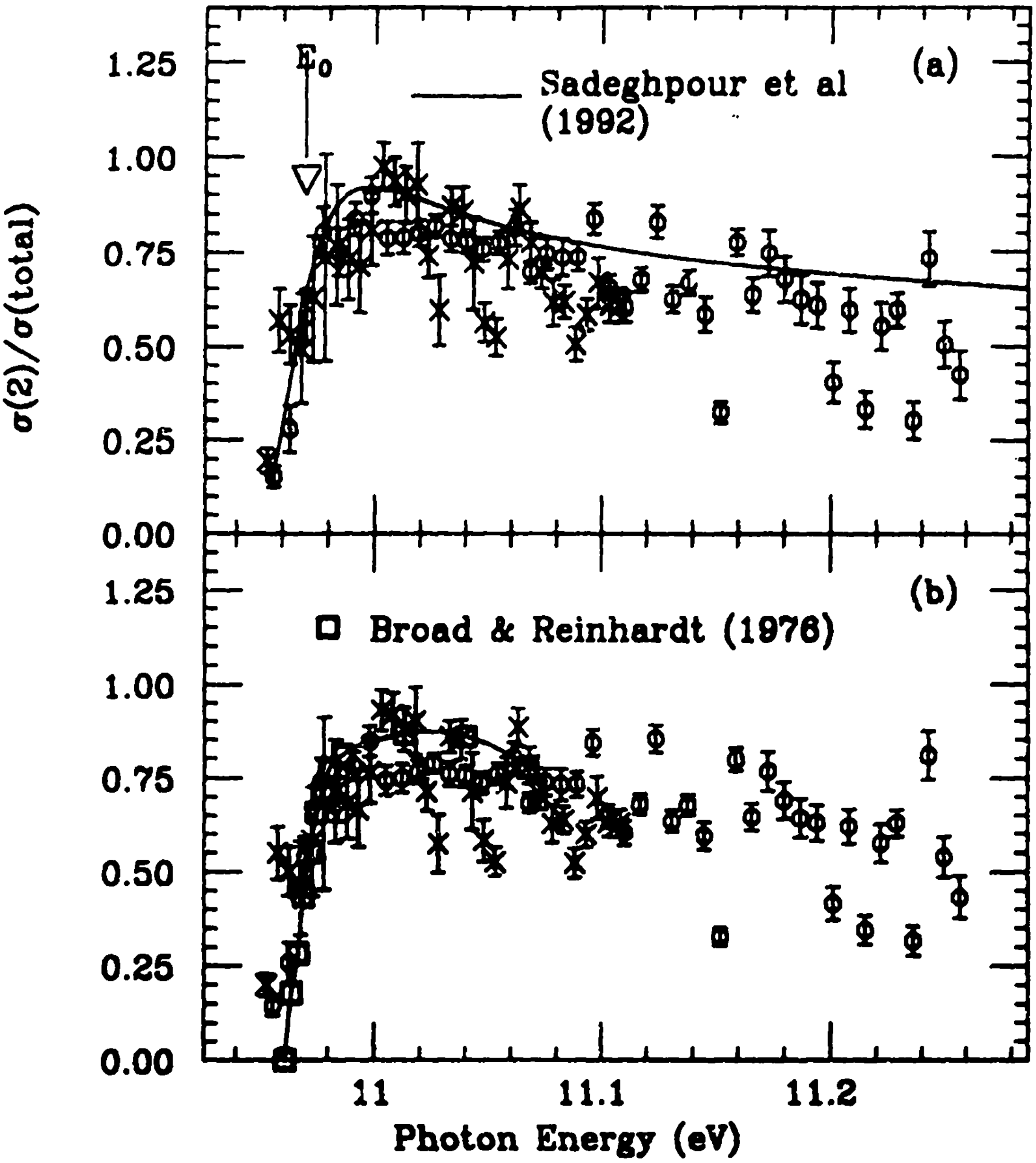

Figure 7.11: Shape resonance branching ratio vs photon energy. Open circles, 1983 data. Crosses, 1990. Arrow points to the approximate central energy. (a) Solid line, theory of Sadeghpour *et al* [1]. (b) Squares, theory of Broad and Reinhardt [36].

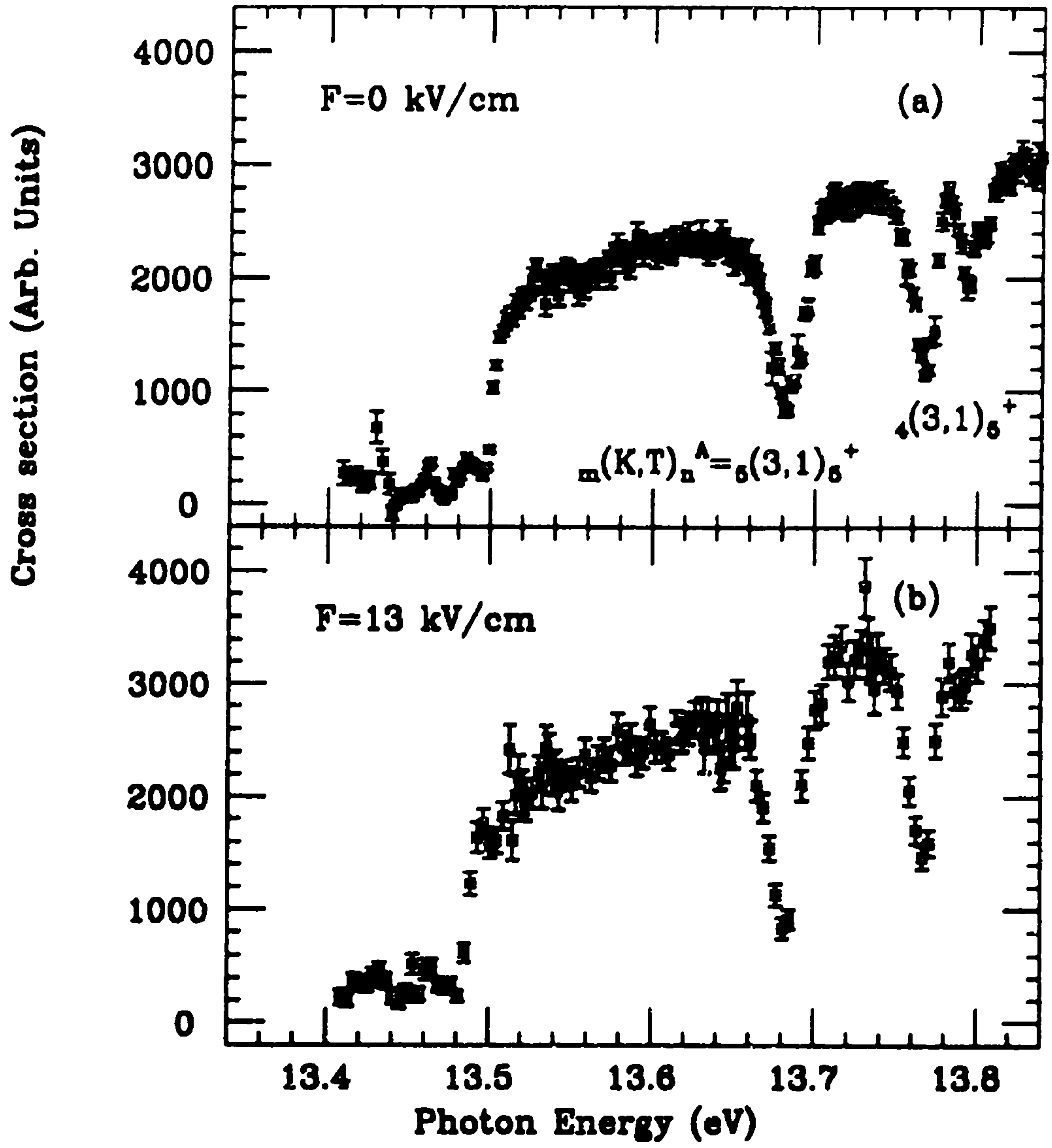

Figure 7.12: Photodetachment of H$^-$ with detection of fragment H(4) atom. (a) Zero applied field. (b) F=13 kV/cm.

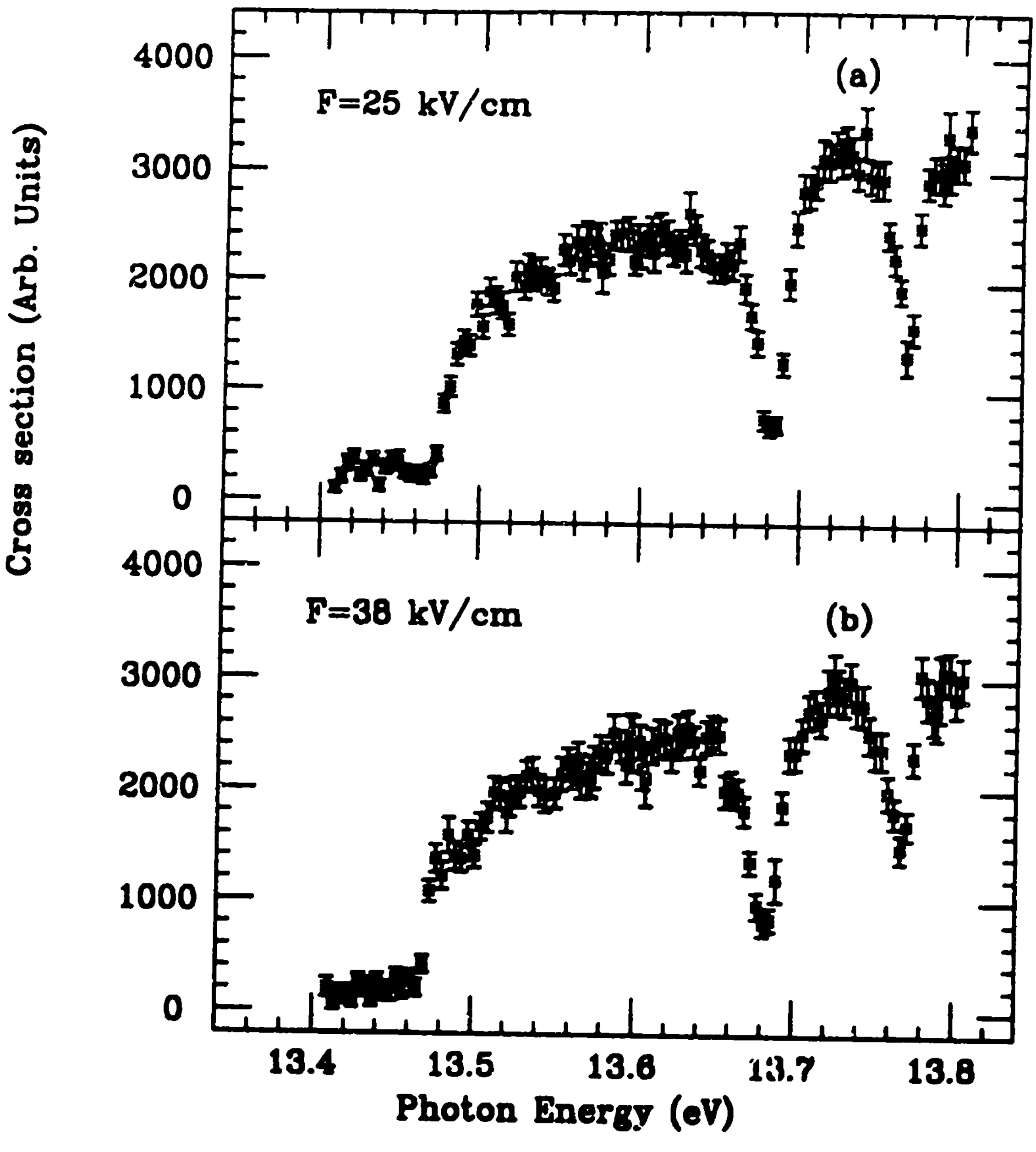

Figure 7.13: Photodetachment of H^- with detection of fragment H(4) atom. (a) F=25 kV/cm. (b) F=38 kV/cm.

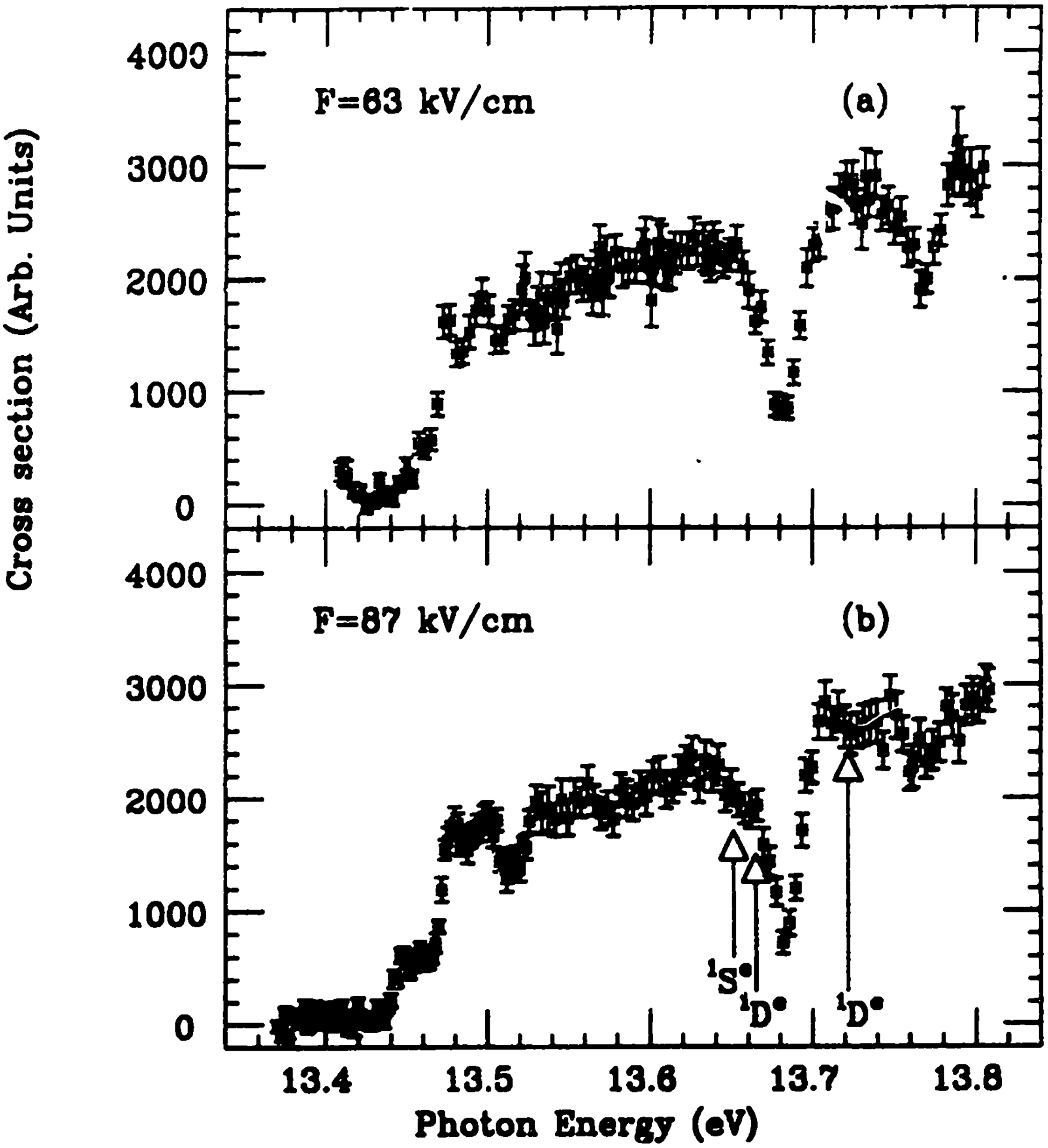

Figure 7.14: Photodetachment of H^- with detection of fragment H(4) atom. (a) F=63 kV/cm. (b) F=87 kV/cm. Arrows point to field-free central energies of some even parity resonances.

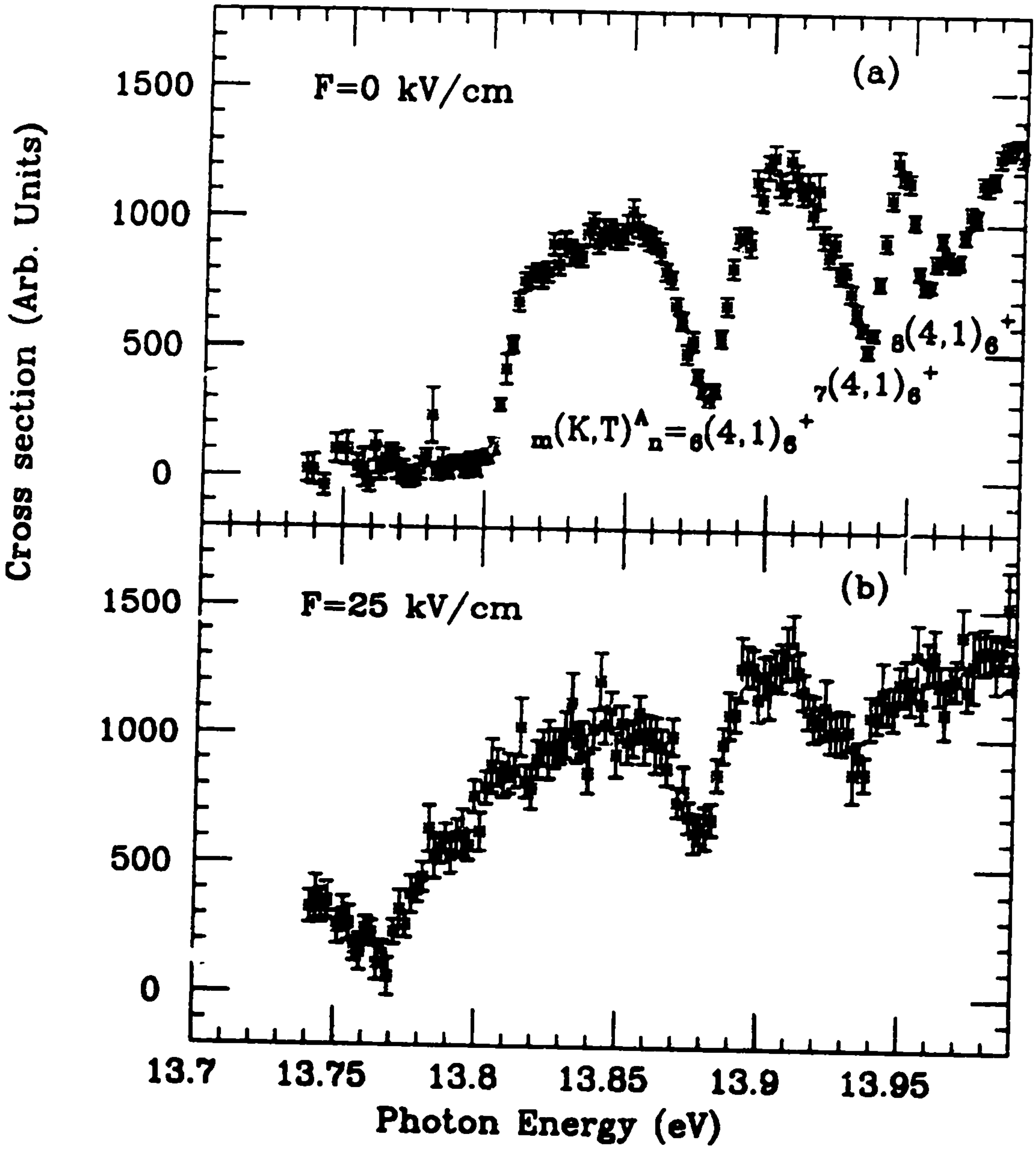

Figure 7.15: **Photodetachment of H^- with detection of fragment H(5) atom. (a) F=0 kV/cm. (b) F=25 kV/cm.**

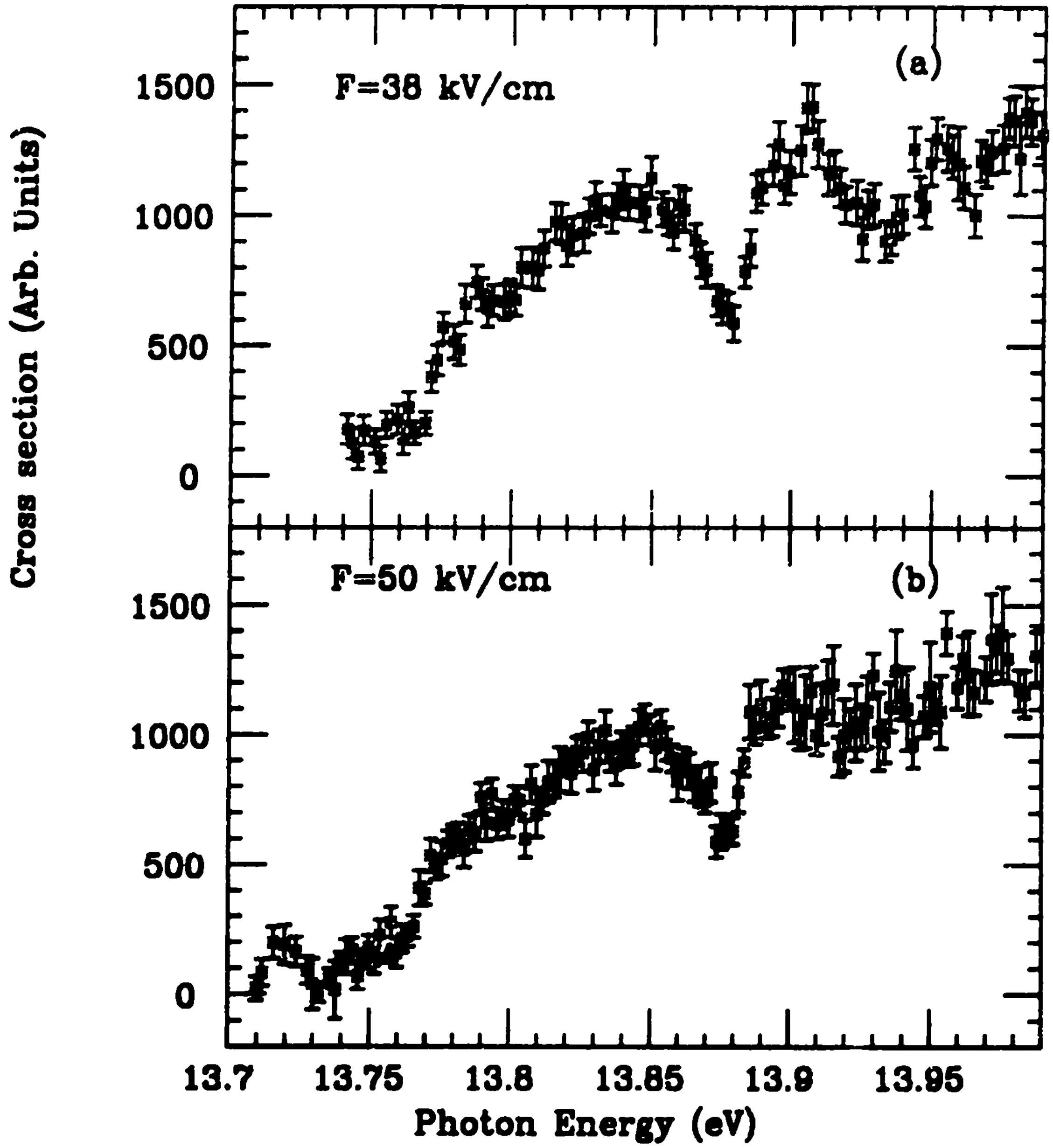

Figure 7.16: Photodetachment of H^- with detection of fragment H(5) atom. (a) F=38 kV/cm. (b) F=50 kV/cm.

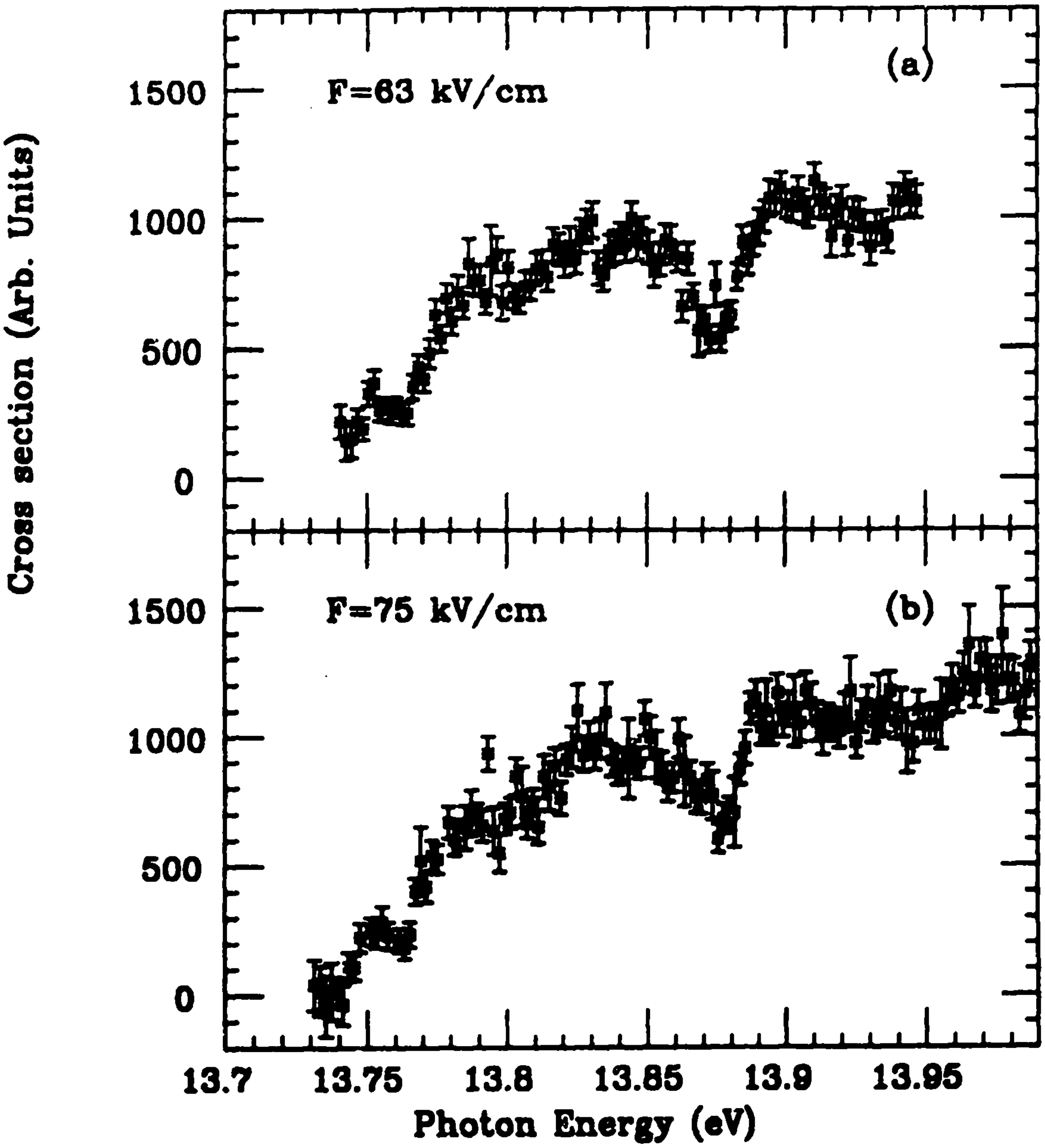

Figure 7.17: Photodetachment of H^- with detection of fragment H(5) atom. (a) F=63 kV/cm. (b) F=75 kV/cm.

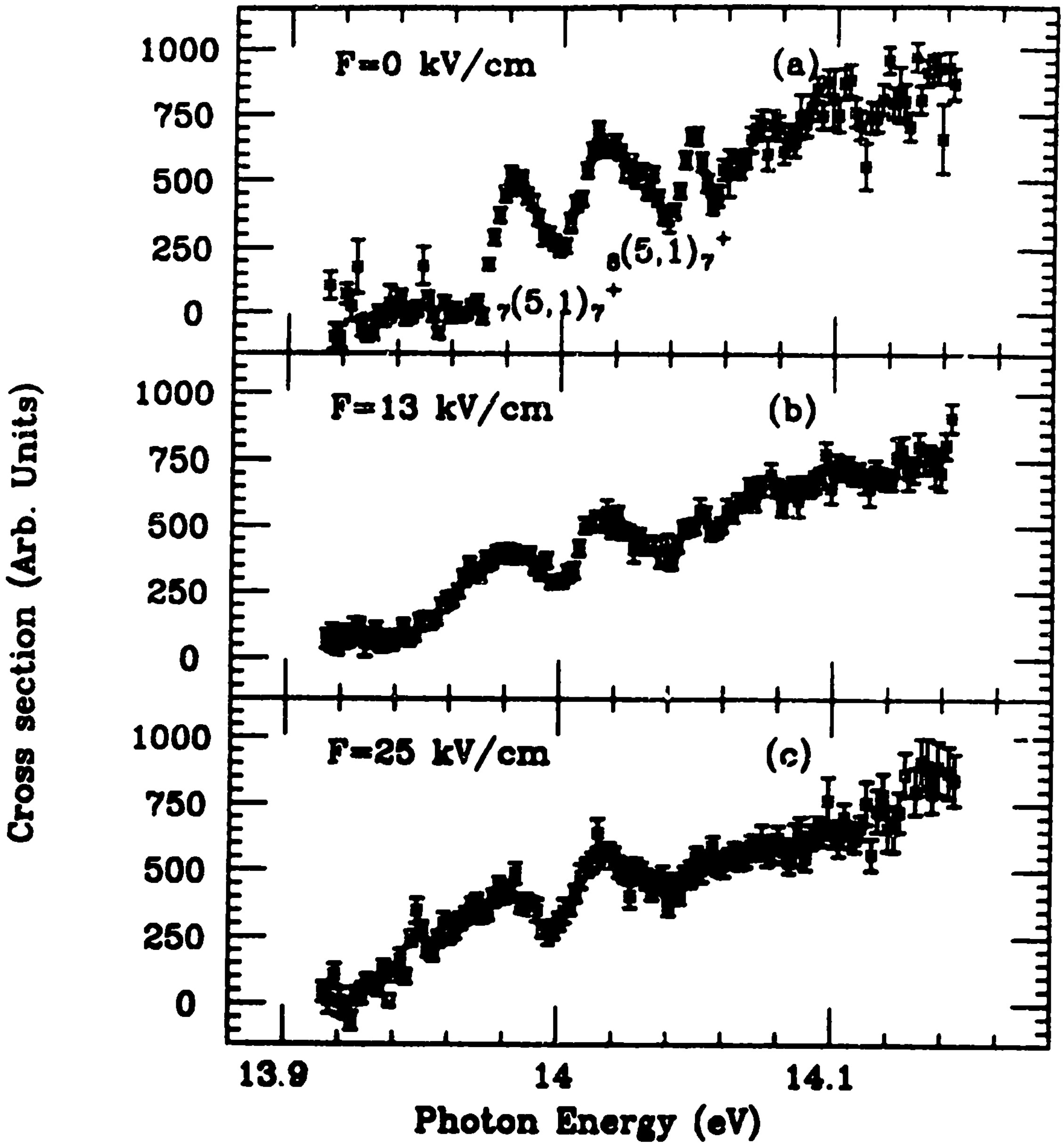

Figure 7.18: Photodetachment of H^- with detection of fragment H(6) atom. (a) F=0 kV/cm. (b) F=13 kV/cm. (c) F=25 kV/cm.

other channels, but no unusual structure is observed in the N=6 continuum at these field strengths.

The results of fitting the zero-field thresholds to a step function convoluted with a Gaussian function having a width equal to the experimental resolution are shown in Figure 7.19. While the N=5 and 6 thresholds are good fits to a step function with confidence levels of 95%, the CL for the N=4 threshold to be a step function is only 0.1%. The poor conformation to a constant function at the H(4) threshold may be an indicator that a centrifugal potential is interfering in this energy region. In fact, a shape resonance at ≈13.5 eV in the H(N=2) decay channel has been predicted in R-matrix calculations of Sadeghpour *et al* [1]. No shape resonance potential appears for $n=4$ in hyperspherical curves of Zhou and Lin, however. The experimental evidence is far from conclusive, but hints that an experimental study with better statistics and better energy resolution might be in order.

Figure 7.20 plots the amplitude of the threshold shift ΔE relative to the zero-field threshold for each field strength. These shifts are nearly an order of magnitude larger than those expected from Stark splitting of the H levels, as shown by the dashed lines in the figure. The solid lines are fits to a function which is proportional to $F^{2/3}$ (explained in Section 2.3.1) with the dipole moment a as a parameter called a_p. Our fits using the MINUIT code [65] provide $|a_p|=11.0\pm0.2$ (13.0 ± 0.2) a.u. for the N = 4 (5) threshold. The reduced chi-squared (χ^2/ν) is less than 0.7 for both fits, implying that we may have overestimated the size of our error bars, as mentioned in Section 6.2.1. These values of a are not consistent with theoretical zero-field dipole moments

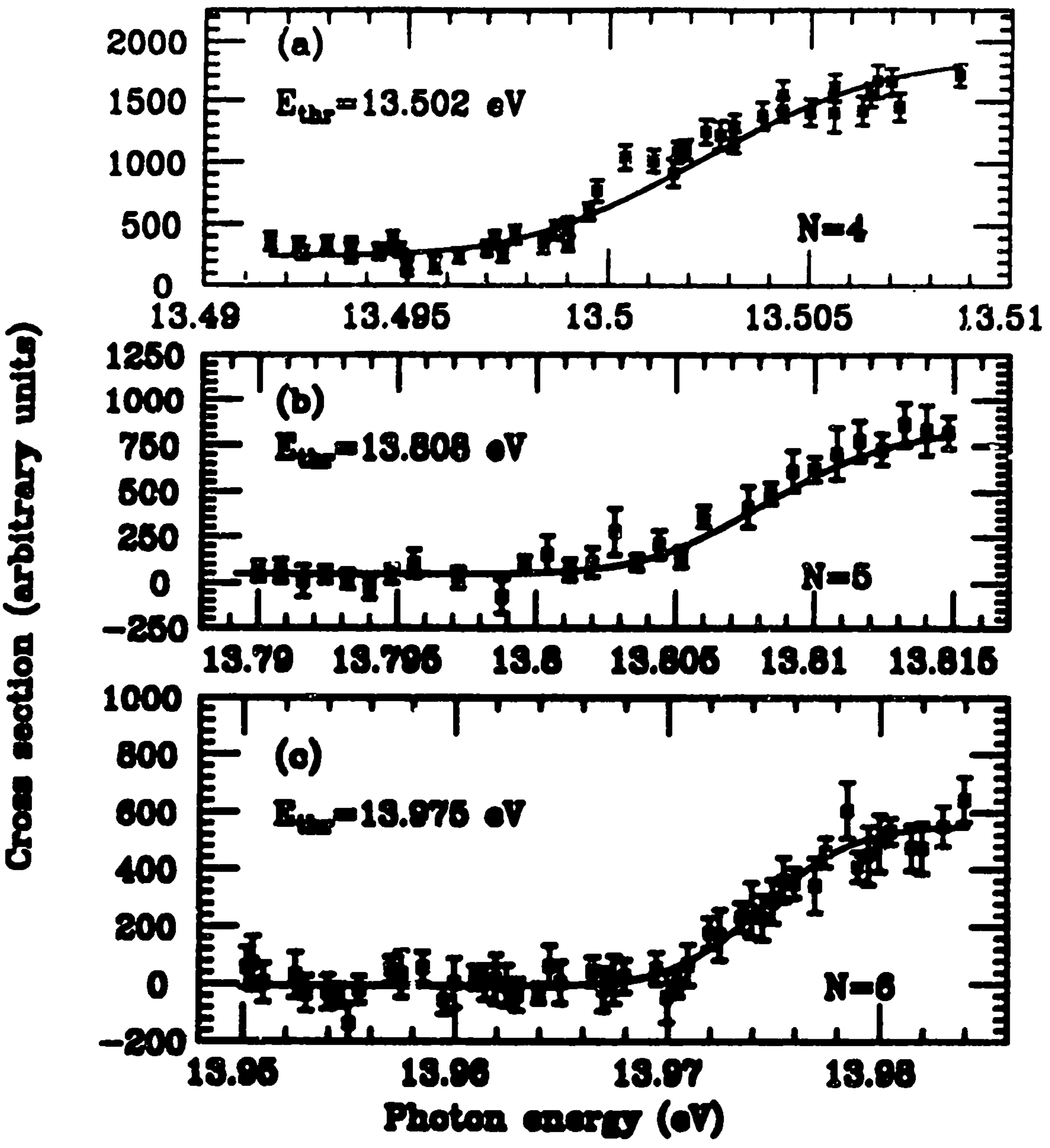

Figure 7.19: Thresholds fit to a step function. (a) H(4) threshold. (b) H(5) threshold. (c) H(6) threshold.

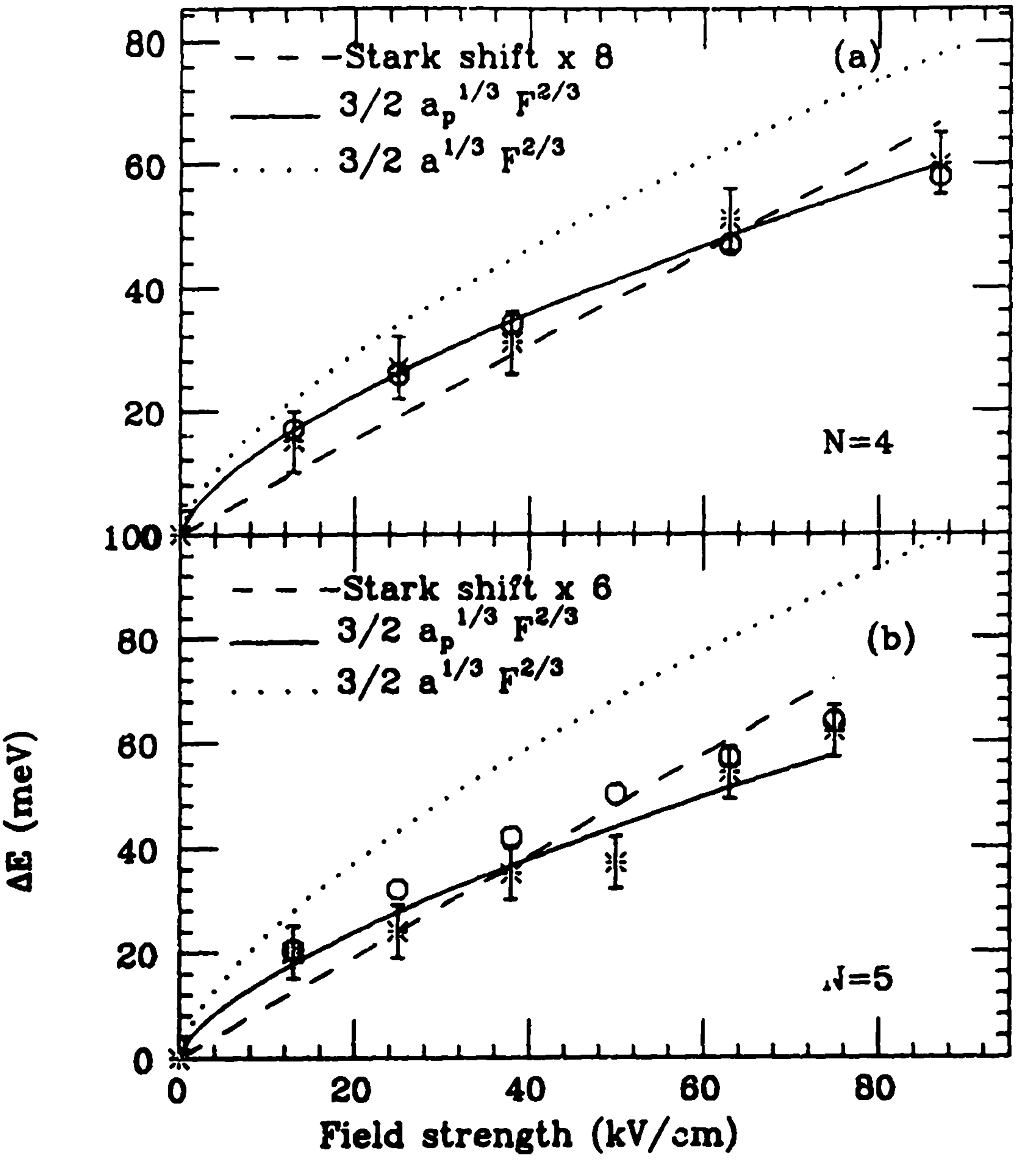

Figure 7.20: **Threshold shift ΔE relative to the zero-field threshold vs field strength. Open circles indicate values from calculations of Zhou and Lin [28]. (a) H(4) threshold shift values. (b) H(5) threshold shift values.**

calculated for the lowest '+' channel in each N-manifold: $a_{4\{0\}+}$=−18.5, $a_{5\{0\}+}$=−37.8. (from Eqn. (9) of Ref. [17]). See dotted line of Figure 7.20.) As explained by Zhou and Lin [28], it is found that the coupling between the '+' and '−' channels plays a significant role here, and the classical estimate is not adequate. Their values for ΔE from quantum mechanical calculations are plotted as open circles in Figure 7.20. Excellent agreement with experiment is seen for the H(4) threshold, while theoretical values are somewhat high compared with the experimentally measured H(5) threshold shifts.

A particularly intriguing change in the H(N=4) cross section appears in F=87 kV/cm. Figure 7.14(b) shows that a dip develops which is not seen in lower field strengths. A fit to the Fano function [7] places this feature at 13.513±0.001 eV—10 meV higher in energy than the zero-field threshold. The width from the fit is 15±6 meV. It has been suggested that this feature is the result of the modification of the $^1P^o$ '+' potential curve where an effective centrifugal potential barrier is induced when a field is applied [28]. This new potential does not modify the positions of the first two resonances associated with the '+' channel, but the third resonance is lifted to a position above the zero-field threshold. Without cross section calculations, it is unknown whether this feature should emerge as a peak or a dip, but the energy of the observed resonance compares favorably with the value E_0=13.511 eV calculated by Zhou and Lin using the WKB approximation. This means that a zero-field Feshbach resonance (below threshold) is transformed by a static field into a shape resonance (above threshold). To our knowledge, this idea is unprecedented, and shows that these are pioneering experiments which should be repeated with improved resolution, if possible.

We see no obvious periodic field-induced modulations of the type observed in the single electron photodetachment threshold [41, 40] One might expect this effect to be present since it is caused by the wave function reflecting from the potential barrier induced by the outgoing electron. We suspect, however, that these modulations or "ripples" in the cross section are being washed out by the presence of the resonances. Also note that the laser light used was not well-characterized (about 50% π and 50% σ polarization); ripples might be more obvious if 100% π-polarization were used.

Field Effects on Resonances

Resonances in the H(4) and H(5) continua converging to the $n = 5$ and 6 thresholds respectively, in fields ranging from 0 to 87 kV/cm, were fit to the Fano function. Fits are shown in Appendix G. Of the three $H^{-**}(5)$ resonances resolved in the experiment, the highest-energy state was quenched by a field of about 87 kV/cm. As remarked in Section 2.3.1, the resonance may tunnel into the parent channel. One case in particular—that of the second-lowest $H^{-**}(5)$—seems to verify this idea. In the H(4) channel its energy in a 63 kV/cm field corresponds to a similar feature in the shifted threshold region of the H(5) continuum channel. Compare Figures 7.14 and 7.17. To our knowledge, this is the first experimental evidence of this type of behavior in a two-electron system.

The lowest-lying resonance in the $H^{-**}(5)$ series (E_0=13.686 eV) has become quite asymmetric in the 87 kV/cm field, probably as a result of mixing of the $^1S^e$ and $^1D^e$ states with $^1P^o$. See Figure 7.14(c). The presence of these Stark states may also account for the slight variations in the Fano width and central energy of the resonance as the field magnitude is varied (Figure 7.21).

The same small variations in width and resonance energy with field strength are also observed in the second lowest $H^{-**}(5)$ at 13.77 eV (Figure 7.22) and in the two lowest $H^{-**}(6)$ resonances (Figures 7.23 and 7.24).

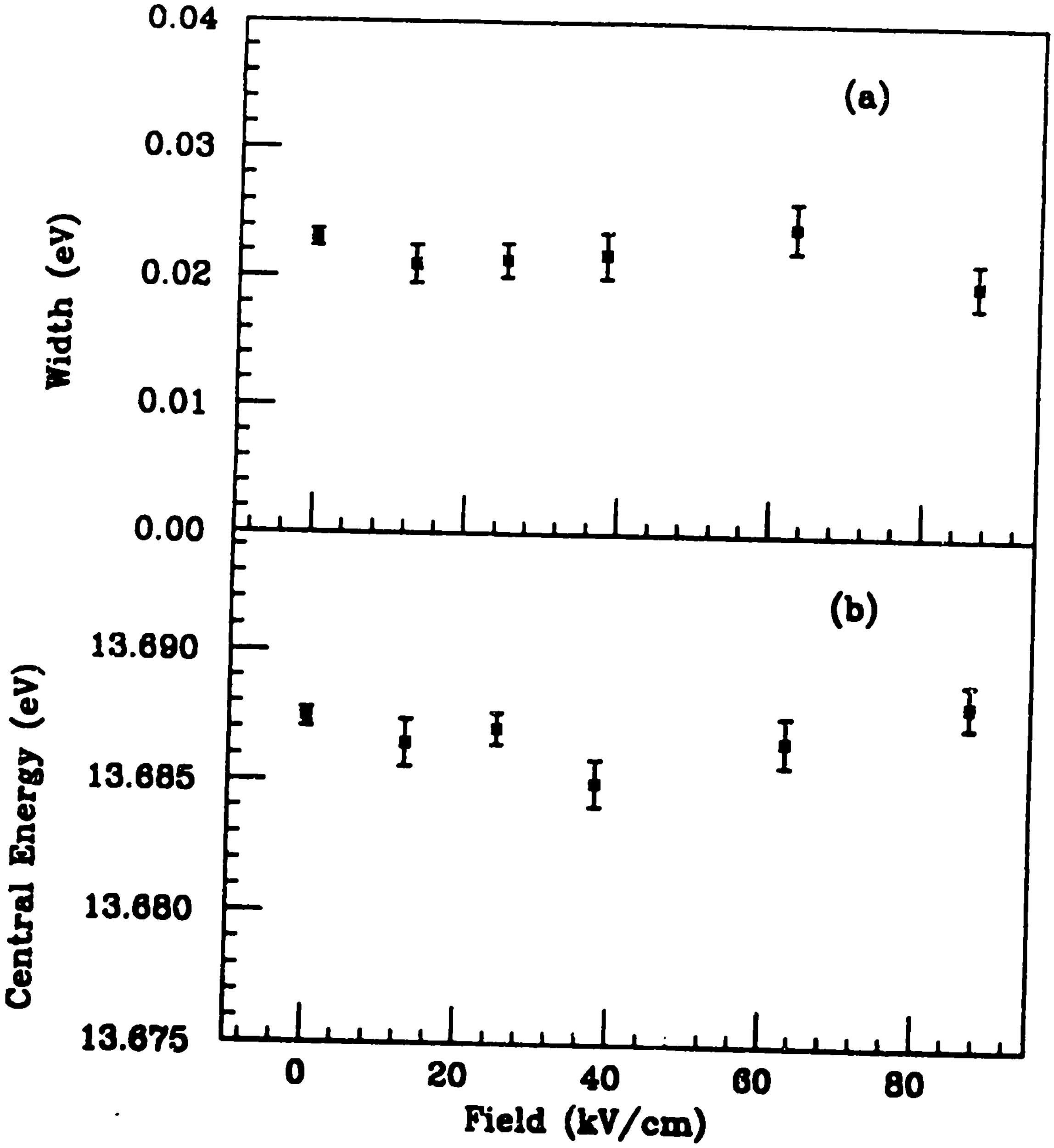

Figure 7.21: Fano parameters from fits to first $H^{-**}(5)$ for various field magnitudes. (a) Width vs field strength. (b) Central energy vs field strength.

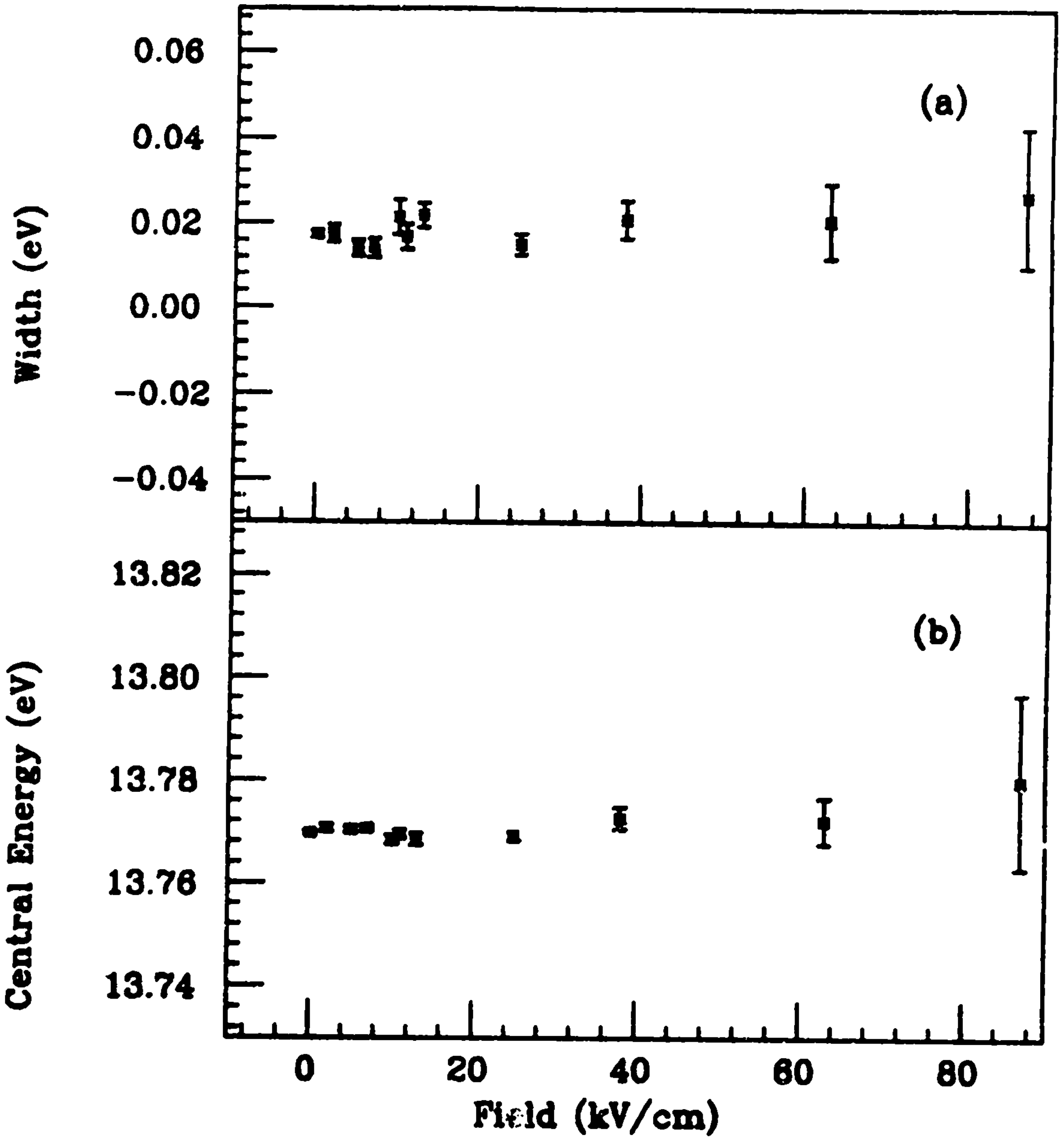

Figure 7.22: Fano parameters from fits to second $H^{-**}(5)$ for various field magnitudes. (a) Width vs field strength. (b) Central energy vs field strength.

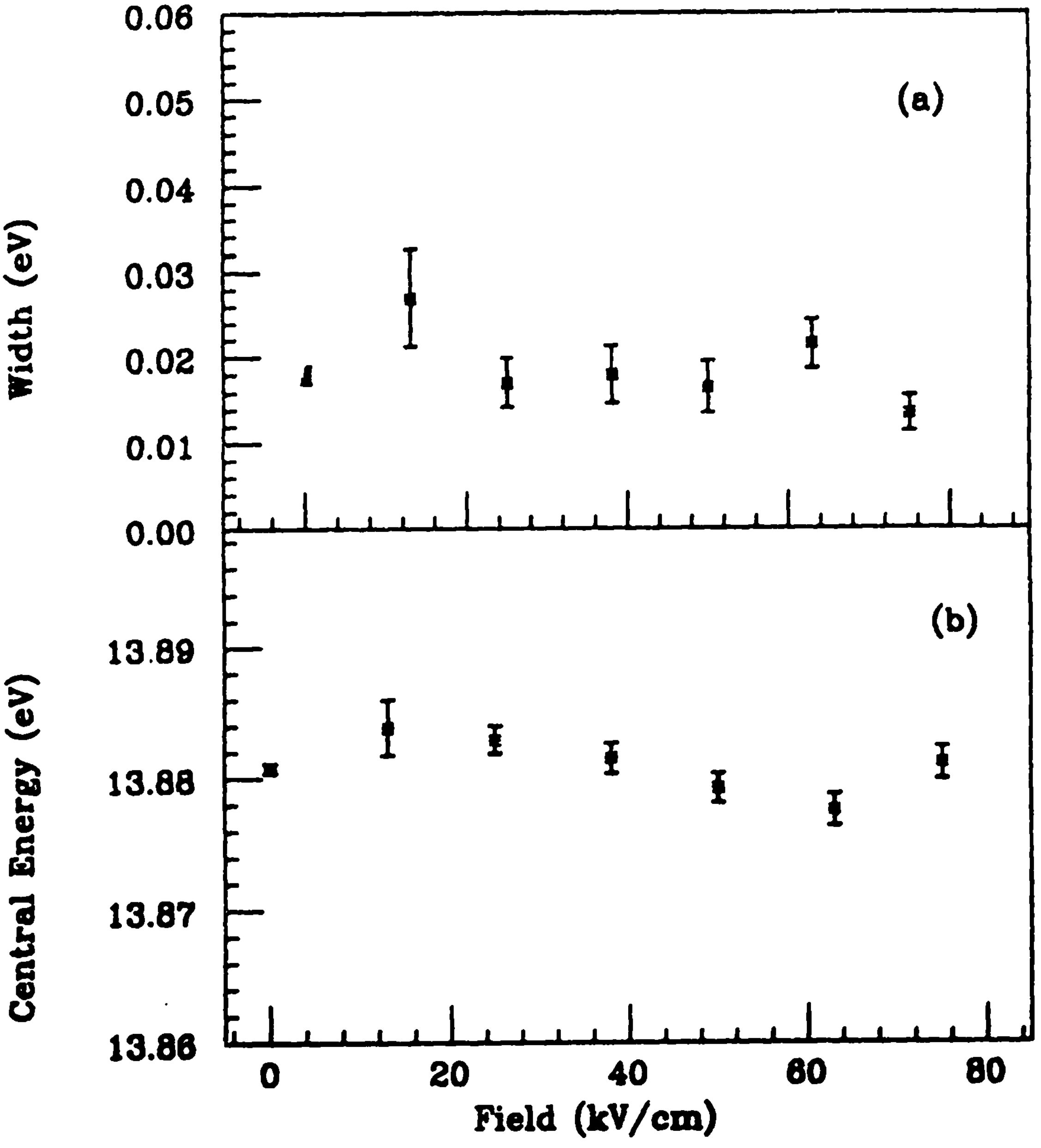

Figure 7.23: Fano parameters from fits to first $H^{-**}(6)$ for various field magnitudes. (a) Width vs field strength. (b) Central energy vs field strength.

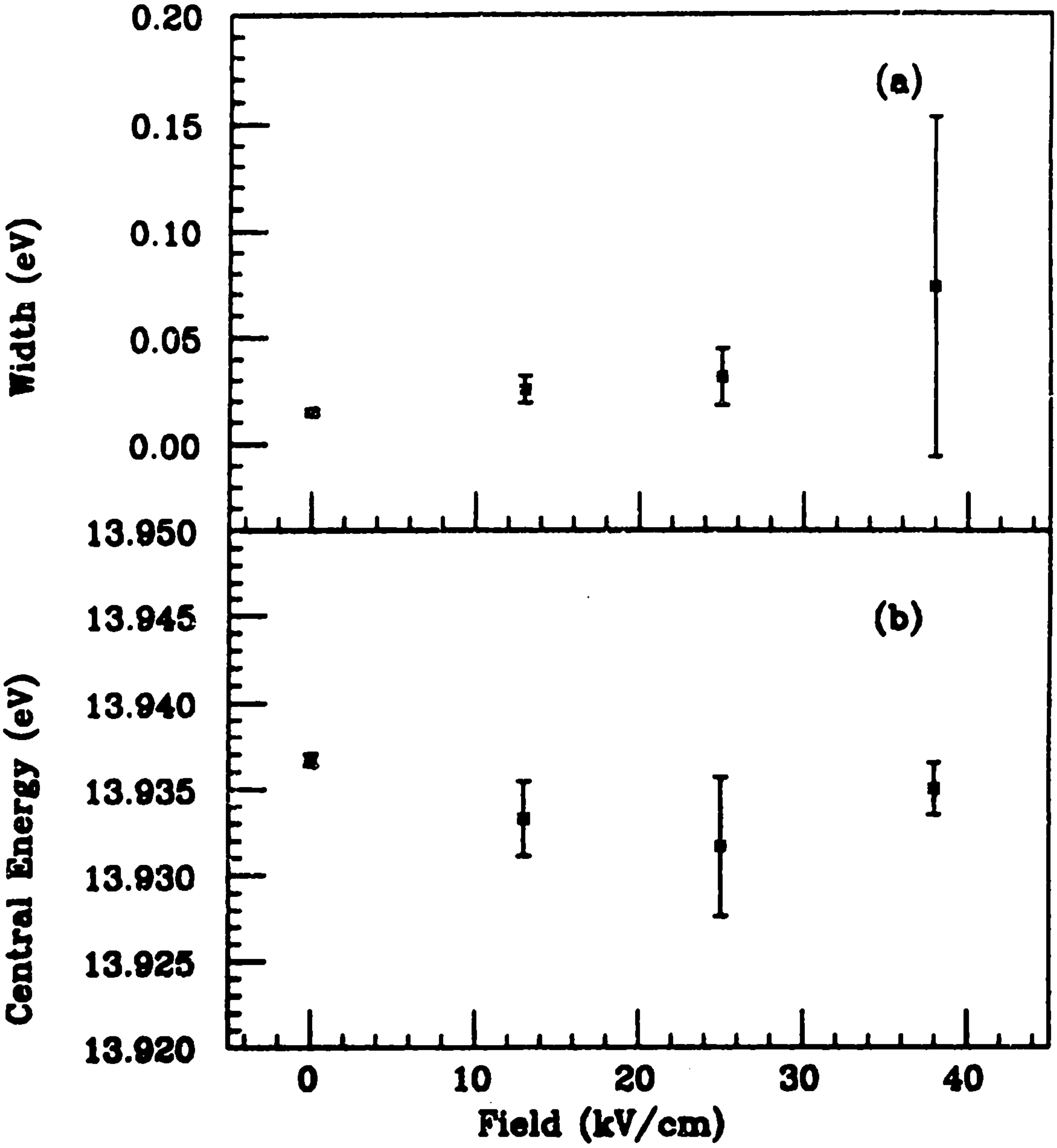

Figure 7.24: Fano parameters from fits to second $H^{-**}(6)$ for various field magnitudes. (a) Width vs field strength. (b) Central energy vs field strength.

Chapter 8

Summary and Outlook

8.1 Summary

Our partial cross section measurements for $H^{-**}(3) \rightarrow H(2)+e$ demonstrate for the first time that the nearest energetically-available continuum channel is preferred in the autoionization process. This propensity has been predicted by many theorists (See Appendix D), but never proven experimentally. The measured profile for the lowest $H^{-**}(3)$ and $H^{-**}(4)$ states compare favorably with R-matrix theory profiles of Sadeghpour, Greene, and Cavagnero.

At photon energies between 10.975 and 11.2 eV, the $H^{-**}(n=2)$ shape resonance shows a preference for decay to the H(2) channel. Within this energy range, the branching ratios calculated from our experimental data show good agreement with calculations of Sadeghpour *et al* [16] and Broad and Reinhardt [15]. The cross sections normalized to theoretical peak amplitudes also agree well. Various functional forms fit to the data show none clearly superior to the Fano function for goodness-of-fit. Discrepancies between cross section measurements indicate that a careful study of the effect of laser-intensity variation is needed.

In applied electric fields, large, nonclassical shifts to lower energy of the H(N=4, 5, and 6) production thresholds were observed for the first time. The stronger fields ($F \geq 50$ kV/cm) generate resonance-like structure in the cross section below the zero-field threshold region. It has been shown that at least one of these resonances can be attributed to field-assisted tunneling of a Feshbach resonance converging to the zero-field threshold from below. This is the first experimental evidence of "decay to the parent" of an autoionizing state, an interpretation compatible with results of hyperspherical calculations by Zhou and Lin. A new resonance develops *above* the zero-field H(4) threshold energy as the magnitude of the electric field is increased, and is quite obvious in a field F=87 kV/cm. This has been interpreted as a field-induced shape resonance, a phenomenon to our knowledge never observed or hypothesized before the appearance of this data.

The zero-field Feshbach resonances converging to the H(5, 6, and 7) thresholds were observed to shrink and become asymmetric when static fields were applied to the laser–H^- interaction volume. This behavior is in accord with current ideas about the nature of doubly-excited resonances, but theoretical cross sections are as yet unavailable.

8.2 Outlook

Experiments in photodetachment of the negative ion of hydrogen have proven to be rich in information regarding the three-body Coulomb problem. The method of crossing laser beams with a relativistic H$^-$ beam provides the greatest energy tunability, and has delivered many new—even unpredicted—results.

Particularly important have been recent studies of high-n thresholds and doubly-excited resonances with and without applied dc fields [26], multiphoton experiments [79], and foil transmission work [80]. The application of partial cross section measurements to an understanding of the H$^-$ system attempted in this thesis is only a beginning. Understanding of this ion and its electron correlations is far from complete, and much work remains for future experimental investigation.

- Using the two-laser method described in this thesis, branching ratios for the excited states of H$^-$ to decay into the various excited states of neutral hydrogen should be measured, although some care must be taken when considering decay to H(n=2) because of the rapid radiative decay of the $2p$ state [81] (lifetime 1.6 ns). The flight path must also be carefully shielded from stray fields.

- H(2) production near the H(4) threshold should be examined with better resolution to determine if a shape resonance occurs in this energy region.

- The H(3) production threshold region should be examined with applied static fields.

- A most interesting experimental study would be to continue the measurement of resonances to energies above the n=8 threshold. Doubly-excited states converging to thresholds with $n \geq 9$ should overlap the next lower threshold, and interfere with those converging there, possibly inducing quantum chaos [82].

- The large shape resonance just above the n=2 threshold has been studied in static electric fields [83], but a more systematic experiment, using smaller steps in the electric field strength, should most certainly be performed to look for predicted oscillations on the high-energy shoulder [52] of this unique resonance. A study of the width of the shape resonance as a function of laser intensity should also be done.

- The lowest electron-detachment threshold at 0.7542 eV should be studied in applied field strengths greater than about a MV/cm. This is the region in which Fabrikant [84] predicts the observability of rescattering of the electron wave.

- The lowest-energy Feshbach resonance at a photon energy of 10.9264 eV has been observed with a resolution of two meV. Theory, however, predicts a width on the order of 30 μeV [58]. A measurement of this width would be useful as a gauge to theorists making very high-precision calculations. If this resolution can be achieved, the second-lowest n=2 Feshbach resonance might also be observed.

- A remeasurement of the two-electron detachment threshold is planned for 1993 at LAMPF. The expected experimental resolution of 2 meV should be sufficient to observe the presence or absence of modulations on the threshold, such as have been predicted in a Coulomb-dipole model calculation [85].

- Cross section measurements to date have been relative only, owing to the uncertainty in the overlap volume between the laser and ion beams. Large differences among various theoretical predictions for photodetachment cross sections [81] indicate however that absolute cross section measurements should be attempted in the region of the H(n=2) threshold at least.

Appendix A

Relativistic transformations

The conversion between two different frames of reference, known as the "Lorentz tranformation", for the case in which the two frames are defined to have a common origin in time and space, is discussed in this appendix. The convention of Minkowski in which time and time-like kinematic objects are treated as imaginary numbers is adopted here with the relative motion along the x-axis. An event in the frame S can thus be located with the four-vector (x, y, z, ict) and in the uniformly relatively moving frame S′ with (x′, y′, z′, ict′). The conversion $\underline{L}$ relating these two descriptions of the same event is, in tensor form,

$$\underline{L} = \begin{bmatrix} \gamma & 0 & 0 & i\beta\gamma \\ 0 & 1 & 0 & 0 \\ 0 & 0 & 1 & 0 \\ -i\beta\gamma & 0 & 0 & \gamma \end{bmatrix} . \tag{A.1}$$

The energy-momentum four-vectors of a particle as determined in the two frames are thus related by

$$\begin{bmatrix} p'_x \\ p'_y \\ p'_z \\ iE'/c \end{bmatrix} = \underline{L} \begin{bmatrix} p_x \\ p_y \\ p_z \\ iE/c \end{bmatrix} \tag{A.2}$$

In the case where the particle is a photon, the connection is particularly simple because of the Lorentz-invariant relation

$$p^2 - \frac{E^2}{c^2} = p'^2 - \frac{E'^2}{c^2} = 0 \tag{A.3}$$

since the photon mass is zero. This relationship follows simply from the fact that the length of a four-vector squared (its dot product with itself) is an invariant under the Lorentz transformation. In the case of the energy-momentum four-vector the length is $(mc)^2$ where m is the particle's rest mass.

Taking the nonconstraining definition that $p_z=0$, and explicitly using $p=E/c$, we have

$$\begin{bmatrix} p' cos\ \theta' \\ p' sin\ \theta' \\ 0 \\ ip' \end{bmatrix} = \underline{L} \begin{bmatrix} p\ cos\ \theta \\ p\ sin\ \theta \\ 0 \\ ip \end{bmatrix} \tag{A.4}$$

where θ and θ', respectively, are the angles the photon's trajectory makes with the x and x′ axis in the xy and x′y′ planes.

From the fourth component of (A.4) we have directly

$$ip' = \gamma(-i\beta p\ cos\ \theta + ip) \tag{A.5}$$

or

$$E' = \gamma(1 - \beta \cos \theta)E \tag{A.6}$$

which is known as the "Doppler shift".

Appendix B

Hyperspherical Coordinates

In hyperspherical coordinates the two electrons are treated as a quasiparticle mapped in six dimensions—five angles and one "radius"). The hyperradius is defined as R=$\sqrt{r_1^2+r_2^2}$, where r_1 and r_2 are the radial distances to the two electrons. The hyperangles are $\alpha = arctan(r_2/r_1)$ with $0 \leq \alpha \leq \frac{\pi}{2}$ and θ_{12} =$\cos^{-1}(\hat{r}_1 \cdot \hat{r}_2)$, plus three Euler angles (ϕ, θ, ψ) locating the triangular figure in space. The set of six coordinates (R, $\alpha, \theta_{12}, \phi, \theta, \psi$) is equivalent to $(\vec{r}_1, \vec{r}_2)$. In this coordinate system the potential energy

$$V(r_1, r_2) = -\frac{Ze^2}{r_1} - \frac{Ze^2}{r_2} + \frac{e^2}{r_{12}}, \tag{B.1}$$

with $r_{12} = |\vec{r}_1 - \vec{r}_2|$, becomes [86]

$$V(R, \alpha, \theta_{12}) = \frac{e^2}{R} C(\alpha, \theta_{12}) \tag{B.2}$$

where

$$C(\alpha, \theta_{12}) = -\frac{Z}{cos\ \alpha} - \frac{Z}{sin\ \alpha} + \frac{1}{\sqrt{1 - sin(2\alpha)\ cos\ \theta_{12}}}. \tag{B.3}$$

is the correlation potential for two electrons in the field of a proton.

The coupling term involving θ_{12} causes the channels to repel each other, giving rise to narrowly avoided crossings among the adiabatic potential curves. These weak couplings may be eliminated by the implementation of diabatic states in the region of the avoided crossings. The curves may be made diabatic by allowing R to vary nonadiabatically in the region of interest. Curves of opposite symmetry may thus cross, and the potentials become diabatic as shown in Figure B.1. With this approximation technique the Schrödinger equation becomes separable in hyperspherical coordinates.

Neglecting the spin-orbit coupling the hyperspherical Schrödinger equation for the electron pair is then

$$\left[\frac{1}{2}\left(-\frac{\partial^2}{\partial R^2}+\frac{\Lambda^2}{R^2}\right)+V(R,\alpha,\theta_{12})-E\right]\Psi(R,\alpha,\theta_{12})=0 \tag{B.4}$$

where

$$\Lambda^2=-\frac{\partial^2}{\partial\alpha^2}-\frac{1}{4}+\frac{\ell_1^2}{cos^2\alpha}+\frac{\ell_2^2}{sin^2\alpha}. \tag{B.5}$$

The quantity $-(\Lambda/R)^2$ describes a generalized angular momentum barrier, and Λ is designated the "grand angular momentum".

Correlation quantum numbers

The highly degenerate eigenvalues $(\ell_1+\ell_2+2m+2)^2$ of Λ^2 are compatible with a new set of approximate quantum numbers, $(K,T)^A$. These have reasonably been called "correlation" quantum numbers, and correspond to different subgroups of rotations in six dimensions.

K and T effectively replace the independent particle quantum numbers ℓ_1

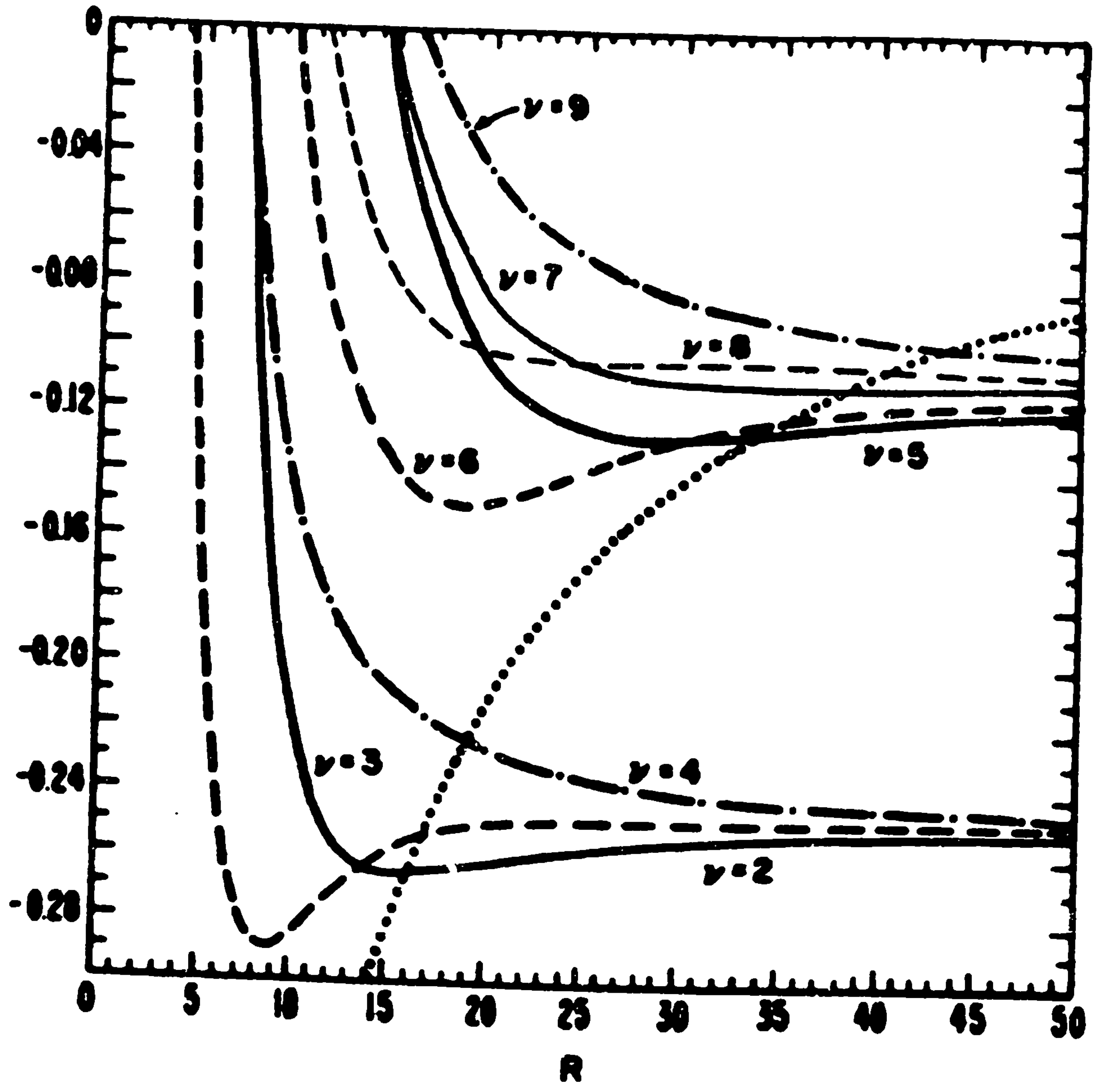

Figure B.1: Diabatic potential curves for H^- $^1P^o$. [87].

and ℓ_2. They are related to the total angular momentum and the principal quantum number n by [88]

$$T = 0,\ 1,\ 2, \ldots,\ min(L, n-1) \tag{B.6}$$

$$K = n-1-T,\ n-3-T, \ldots,\ -n+3+T,\ -n+1+T. \tag{B.7}$$

K describes the angular correlation of the two electrons with respect to the nucleus ($K \propto cos\ \theta$), similar to the bending vibrational quantum number of a triatomic molecule. T is just the familiar orbital angular momentum magnetic quantum number m—the projection of $\vec{L}$ along the interelectronic axis. Nonzero T values express the effect of the torque exerted on the inner electron by the outer one, while $T = 0$ indicates that the electrons move in the same plane.

An important difference between the quantum numbers developed in hyperspherical coordinates and those developed in prolate spheroidal coordinates (see next appendix) is that the magnetic quantum number T is taken to be a good quantum number in the molecular orbital classification which uses prolate spheroidal coordinates. According to a hyperspherical coordinate analysis of Watanabe and Lin [89], however, T is only an approximate quantum number, indicating that states with differing T-values can mix. According to Z. Chen and C. D. Lin, a small admixture of T=0 with T=1 is responsible for the existence of the $H^{-**}(2)\ {}^1P^o$ shape resonance [90].

The quantum number A determines the reflection symmetry of the radial wave function with respect to the $\alpha = \pi/4$ axis, and thus describes radial correlations, but is not independent of K and T:

$$A = \begin{cases} \pi(-1)^{T+S} & \text{for } K \geq L-n+1 \\ 0 & \text{for } K < L-n+1 \end{cases} \tag{B.8}$$

so that $A = \pm 1$ or 0. Here π is the parity, and L is the total angular momentum quantum number. An eigenchannel with $A=+1$ is often called a '+' channel, or a '-' channel if $A=-1$. These are similar to the '+' and '-' states of Cooper, Fano and Prats, mentioned in Section 1.1. The $A=0$ channel is completely repulsive and binds no states in H^-. The tendency of '+' channels to produce the strongest resonances has been substantiated by several authors [16, 91, 88], and verified by the LAMPF experiments.

Doubly-excited states are often labeled as ${}_m(K,T)_n^A\ {}^{2S+1}L^\pi$, where m and n retain the usual meaning from the independent particle model, being the principal quantum numbers of the outer and inner electrons respectively. This notation is used extensively in this thesis.

Appendix C

Prolate Spheroidal Coordinates

The six independent coordinates in the molecular orbital classification are R, θ, ψ, λ, μ, and ϕ where $\lambda = (r_1 + r_2)/\mathrm{R}$ and $\mu = (r_1 - r_2)/\mathrm{R}$ are the prolate spheroidal coordinates, and ϕ is the azimuthal angle of r, the position of the nucleus with respect to the CM of the two electrons.

Adapted from molecular theories, the formulation allows for approximate quantum numbers (n_μ, n_λ, m) which can be related to the hyperspherical quantum numbers. An excellent review on the subject is found in reference [92] where it is shown that

$$K = \left[\frac{n_\mu}{2}\right] - n_\lambda \tag{C.1}$$

$$T = m \tag{C.2}$$

$$A = (-1)^{n_\mu} \tag{C.3}$$

Here $[n_\mu/2]$ is the integer value of $n_\mu/2$ and m is the familiar magnetic quantum number, considered to be a good quantum number in molecular orbital calculations of Feagin and Briggs. n_μ designates the number of nodes in the hyperspherical coordinate α, which coincides with one of the prolate spheroidal directions, and n_λ gives the number of elliptical molecular orbital nodes.

It is interesting to note that n_λ, n_μ, and m can be extracted from consideration of the potential curves at any R, while the hyperspherical quantum numbers K, T, and A were developed in the asymptotic limit of the escaping electron ($R \to \infty$) [93].

Appendix D

Propensity Rules

Propensity rules, as the name implies, are not exact selection rules. Rather they tell us what transitions are most likely when the atom or ion in question passes from one state to another. Not surprisingly, they have been formulated in both hyperspherical and prolate spheroidal coordinates for electron-scattering and for photodetachment.

In one of the earliest and most comprehensive studies of the application of hyperspherical coordinates to atomic systems, Watanabe and Lin [89] introduced "systematics" of autoionization widths relating to the overlap between the doubly-excited resonance wave function with a continuum wave function. When $\alpha = \pi/4$, $\theta_{12} = 0$, the overlap is expected to be at a maximum, epecially when channels have similar characteristics—a propensity which is verified by the 1990 $H^{-**}(3) \rightarrow H(2)$ measurement. These authors introduced "rules of thumb" (propensity rules) for autoionization which give

$$\Delta n = -1, \ \Delta K = -1, \text{ and } \Delta T = 0 \tag{D.1}$$

with A unchanged.

A measure of real angular excitation, the number of nodes in θ_{12} (sometimes called the vibrational quantum number $_{n}\{v\}^{A}$ [17]) is found to be $(n - 1 - K - T)/2$ [94], but this is equivalent to the molecular orbital quantum number n_λ. Using (D.1) we find Δn_λ (or Δv^{+}) $= 0$. The number of nodes in the hyperspherical pseudoangle α is $n_\mu = n - 1 - T + K$ [17]. Again using (D.1) one finds Δn_μ=-2.

For the relation to united atom and separated atom classifications, see reference [92].

Appendix E

Q-program PROC8.FOR

```
C [DAQ588.QDEV] PROC8.FOR
C
C     Modified to output raw data to data file at every laser
C     shot when the PRM parameter SHOT is set to unity.
C                               M. Halka              MAY 16, 1991
C
C     This subroutine is an Analzyer Task event processing routine for
C     event 8, called automatically by the Q system whenever an event
C     8 is encountered in the data stream and the processing status is
C     "PROCESS" and it is either "MUST PROCESS" or "MAY PROCESS" with
C     time available.
C
C     This subroutine retrieves 8 TDC words, 24 ADC words,and
C     24 scaler words.
C
C     The file HIRAB.INC must be on the system disk when this
C     source is compiled.
C
C     This subroutine processes laser related data.
C
      SUBROUTINE PROC8
      IMPLICIT NONE
      INCLUDE 'HIRAB.INC' !include COMMON/REGION/ specification
      INTEGER*2 IEVHDR(2),NUMWRD,RLEN,I,LUN,NUMADC,NUMSC,NUMTDC
      INTEGER*2 ADCHST(32), IERR(2)
      INTEGER*2 TDC(8),MISS
      INTEGER*2 ADCA(12),ADCB(12),ITEST(10)
      INTEGER*2 CALS(2)
      INTEGER*4 SCA(12),SCB(12),ISIG(12),ISTD(12)
      INTEGER*4 LPOW,LERR,BCURR,BERR
      REAL*4 TEMP,OUTX
      LOGICAL*2 TSTVAL   !FUNCTION CALL
      LOGICAL*2 TSTRES
C
```

```
C     LOCAL EVENT DATA STORAGE
C
      COMMON /EVENT8/ IEVHDR,TDC,ADCA,ADCB,SCA,SCB,CALS,NUMWRD
      NUMTDC=8
      NUMADC=24 ! NUMBER OF ADC CHANNELS ( 10 BIT EACH )
      NUMSC=24  ! NUMBER OF SCALER CHANNELS (24 BIT EACH )
      RLEN=2+NUMTDC+NUMADC+NUMSC*2+2 ! NUMBER OF I*2 WORDS
                                     ! 1 WORD= 16 BITS
C
C     RETRIEVE DATA FROM THE MBD BUFFER, PUT DATA IN THE LOCAL ARRAYS,
C     AND RECORD RAW DATA ON TAPE.
C
      CALL AGETEV(1, RLEN, IEVHDR, NUMWRD)
      IF(RLEN.NE.NUMWRD .AND. ANGNUM.EQ.1 .AND. COUNT8.EQ.0)THEN
        WRITE(6,*)' PROC8 --- NUMWRD IS NOT EQUAL TO RLEN'
        WRITE(6,*)' NUMBER OF WORDS RETRIEVED = ',NUMWRD
      ENDIF
C
C     PUT CALORIMETER DATA IN ADCA(12), ADCB(12)
C
      ADCA(12)=CALS(2) ! PEAK VALUE


      ADCB(12)=CALS(1) ! BKGND LEVEL
C
C     STUFF DATA INTO THE HISTOGRAM ARRAY
C
      DO 11 I=1,12
      ADCHST(I)=ADCA(I)
      ADCHST(I+12)=ADCB(I)
 11   CONTINUE
      DO 22 I=1,8
      ADCHST(24+I)=TDC(I)
 22   CONTINUE
C
C ============================================================
C
C
C     UPDATE HISTOGRAMS FOR BLOCK #1
C
      CALL HSTBLK(1, ADCHST,1,1,IERR)
        IF (IERR(1).NE.1) THEN
         WRITE (6,50) IERR(1), IERR(2)
         RETURN
      ENDIF
  50    FORMAT(' PROC8 -- BLOCK 1 UPDATE ERROR; IERR= ',2I6,
     & 'HISTOGRAM NOT UPDATED')
C
C ==============================================================
C
C     WRITE RAW NUMBERS TO DATA FILES IF LOOKING AT
C       SHOT TO SHOT INFO
C
      IF (SHOT .EQ. 1) THEN
        DO 111 I=1,12
        ! REALS
```

```
            TEMP=FLOATI(ADCA(I))                   !RAW NUMBERS
    C       IF(TEMP .LT. 0.5)TEMP=0.0
            IF(LASER.EQ.0 .AND. I.LE.5)TEMP=FLOATJ(SCA(I))
                                        !GET SCALER DATA IF LASER=CW
            IADCR(I)=JNINT(TEMP)            ! PARTICLES PER LASER SHOT
            FADCR(I)=TEMP
            FADCR2(I)=TEMP**2    ! REAL SUM^2 FOR STANDARD DEVIATION

            ! ACCIDENTALS

            TEMP=FLOATI(ADCB(I))                          !RAW NUMBERS
    C       IF(TEMP .LT. 0.5)TEMP=0.0
            IF(LASER.EQ.0 .AND. I.LE.5)TEMP=FLOATJ(SCB(I))
                                        !GET SCALER DATA IF LASER=CW
            IADCA(I)=JNINT(TEMP)                  ! INTEGER PARTICLES PER SHOT
            FADCA(I)=TEMP                         ! REAL SUM FOR AVERAGES
            FADCA2(I)=TEMP**2    ! REAL SUM^2 FOR STANDARD DEVIATION
     111      CONTINUE
          ENDIF
    C
    C     CONVERT DIGITIZED PULSE HEIGHTS TO COUNTS, AND
    C     UPDATE THE RUNNING SUMs AND SUM^2s.
    C
          IF (SHOT .EQ. 0) THEN
            DO 112 I=1,12
            ! REALS
    C
    C         DELETE SPURIOUS EVENTS, A NEW COMMAND BY M.H.
    C
            IF (I .EQ. 1 .AND. FLOAT(ADCA(I)) .EQ. 1) RETURN
    C
            TEMP=INVMR(I)*(FLOATI(ADCA(I))-PDR(I)) !COMPUTE # OF PARTICLES
                                                     !FROM ADC PULSE HEI
            IF(TEMP .LT. 0.5)TEMP=0.0
                                              !GET SCALER DATA IF LASER=CW
            IF(LASER.EQ.0 .AND. I.LE.5)TEMP=FLOATJ(SCA(I))
            IADCR(I)=IADCR(I)+JNINT(TEMP)  ! INTEGER SUM
            FADCR(I)=FADCR(I)+TEMP      ! REAL SUM FOR AVERAGES
            FADCR2(I)=FADCR2(I)+TEMP**2    ! REAL SUM^2 FOR STD DEV

            ! ACCIDENTALS
C         DELETE SPURIOUS EVENTS, A NEW COMMAND BY M.H.
            IF (I .EQ. 1 .AND. FLOAT(ADCA(I)) .EQ. 1) RETURN
    C
            TEMP=INVMA(I)*(FLOATI(ADCB(I))-PDA(I)) !COMPUTE # OF PARTICLES
                                                     !FROM ADC PULSE HEI
            IF(TEMP .LT. 0.5)TEMP=0.0
                                              !GET SCALER DATA IF LASER=CW
            IF(LASER.EQ.0 .AND. I.LE.5)TEMP=FLOATJ(SCB(I))
            IADCA(I)=IADCA(I)+JNINT(TEMP)  ! INTEGER SUM
            FADCA(I)=FADCA(I)+TEMP      ! REAL SUM FOR AVERAGES
            FADCA2(I)=FADCA2(I)+TEMP**2    ! REAL SUM^2 FOR STD DEV
     112      CONTINUE
            ENDIF
```

```
C      TDC DATA
C
       DO 222 I=1,8
          TEMP=FLOATI(TDC(I))
          TDCA(I)=TDCA(I)+TEMP
          TDCA2(I)=TDCA2(I)+TEMP**2
 222   CONTINUE
C
C      WRITE TO THE DATA FILE ( SHOT-TO-SHOT MODE )
C
       IF (SHOT .EQ. 1 .AND. CONFIG.EQ.1) THEN
         OUTX = SECTOR
         IF(ANALYZ .EQ. 0)THEN
         WRITE(11,100)ANGNUM,OUTX,ENCO,
     &     IADCR(DETOK(1)),IADCA(DETOK(1)),ISIG(DETOK(1)),ISTD(DETOK(1)),
     &     IADCR(DETOK(2)),IADCA(DETOK(2)),ISIG(DETOK(2)),ISTD(DETOK(2)),
     &     IADCR(DETOK(3)),IADCA(DETOK(3)),ISIG(DETOK(3)),ISTD(DETOK(3)),
     &     BCURR,BERR,LPOW,LERR,JNINT(TDCSTD(1))
100      FORMAT(1X,I3,1X,F5.1,1X,I5,1X,12I7,1X,5I5)
           ENDIF
       ENDIF
C

         IF(SHOT.EQ.1.AND.CONFIG.EQ.4)THEN
         OUTX=SECTOR
       IF(ANALYZ .EQ. 0)THEN
         WRITE(11,101)ANGNUM,
     &   JNINT(FADCR(6)),JNINT(STDR(6)),JNINT(FADCR(12)),JNINT(STDR(12)),
     &     IADCR(DETOK(1)),IADCA(DETOK(1)),ISIG(DETOK(1)),ISTD(DETOK(1)),
     &     IADCR(DETOK(2)),IADCA(DETOK(2)),ISIG(DETOK(2)),ISTD(DETOK(2)),
     &     IADCR(DETOK(3)),IADCA(DETOK(3)),ISIG(DETOK(3)),ISTD(DETOK(3)),
     &     BCURR,BERR,JNINT(TDCSTD(1))
101      FORMAT(1X,I3,1X,4I5,1X,12I7,1X,3I5)
         ENDIF
       ENDIF
C
C      UPDATE THE EVENT COUNTER
C
       COUNT8=COUNT8+1
       RETURN
       END
```

Appendix F

CAMAC Module List

```
;    HIRAB CAMAC MODULE LIST
;
; [DAQ588.QDEV] HIRAB.QAL
; MBD FILE TO CONTROL HIRAB'S EXPERIMENTS DATA ACQUISITION.
; *****************************************************
;   CRATE 1, SLOT ASSIGNMENTS:
;
;  SLOT  DEVICE              COMMENTS
;  ---- ----------       ---------------------------------------------
;   1   JORGER DD       DATAWAY DISPLAY
;   2   SPARE
;   3   LeCroy     2228A     8 CHANNEL TDC, EVENT 8
;   4   SPARE
;   5   LeCroy     2249W     12 CHANNEL INT. ADC FOR EVENT 8, REALS
;   6   LeCroy     2249W     12 CHANNEL INT. ADC FOR EVENT 8, ACCIDENTALS
;   7   LeCroy  2249A        12 CHANNEL INT. ADC FOR EVENT 9
;   8   LeCroy     2551      12 CHANNEL SCALER FOR EVENT 8, REALS
;   9   LeCroy     2551      12 CHANNEL SCALER FOR EVENT 8, ACCIDENTALS
;  10   LeCroy     2251      12 CHANNEL SCALER FOR EVENT 9
;  11   JORWAY     41        12 BIT NIM OUTPUT REGISTER
;                            BIT 1=STOP
;                            BIT 2=START
;                            BIT 3=RESET FARADAY CUP SCALER
;                            BIT 4=STEP BIG CHAMBER'S STEPPING MOTOR
;                            BIT 5=RESET ANGLE COUNTER
;                            BIT 6-12=SPARE
;  12  SPARE
;  13  KS 3420      INPUT REGISTER FOR EVENT 4
;                            READ THE BIG CHAMBER'S SECTOR POT
;  14  JORWAY       33       2 CHANNEL DAC FOR EVENT 4 OR MANUAL CONTROL
;                            CHANNEL 0: 30 KV POWER SUPPLIES
;                            CHANNEL 1: SPECTOMETER POWER SUPPLY
;  15 SPARE
;  16 JORWAY       61-1      TTL LEVEL INPUT GATE FOR EVENT 4
;                            CHANNEL 0: READ THE LITTLE ENCODER
;                            CHANNEL 1: READ THE BIG ENCODER
```

```
;  17 SPARE
;  18-19 BiRa       2206     LAMPF TRIGGER MODULE
;  20 JOERGER       SMC-L    STEPPER MOTOR CONTROLLER TO CONTROL THE WAFFOG
;                            FLOUR ACTUATOR ( BEAM DUMP )
;  21 JOERGER       SMC-L    STEPPER MOTOR CONTROLLER TO CONTROL THE LITTLE
;                            CHAMBER'S FLOUR ACTUATOR
;  22 SPARE
;  23 LeCroy        2301     QVT CAMAC INTERFACE TO LR3001
;  24-25 BiRa 1302      TYPE A-2 CONTROLLER
;
;  CRATE 2, SLOT ASSIGNMENTS:
;
;  SLOT  DEVICE              COMMENT
;  ---- ----------      ----------------------------------------------
;  1 JORWAY         202      DATAWAY DISPLAY
;  2-3 BiRa         3101-1   15 CHANNEL STEPPER MOTOR CONTROLLER
;                            CHANNEL 1: STEPPER #1 ( LITLLE SPIDER )
;                            CHANNEL 2: STEPPER #2 ( 1/2 WAVE PLATE )
;  4 SPARE

;  5-6 JORWAY       30       1 CHANNEL 12-BIT ADC (R = 100 MOHMS) FOR EVENT
;                            LASER CALORIMETER
;  7 JORWAY         32       2 CHANNEL 12 BIT ADC (R = 100 MOHMS) FOR EVENT
;                            CHANNEL 0: SPECTROMETER MAGNETOMETER
;                            CHANNEL 1: SWEEP MAGNET MAGNETOMETER
;  8 JORWAY         32       2 CHANNEL 12 BIT ADC (R input=100 MOHMS) FOR
;                            EVENT 9
;                            CHANNEL 0: POSITIVE HV
;                            CHANNEL 1: NEGATIVE HV
;  9-20             SPARE
;  21-23 EC, BHT-010/D       BRANCH TERMINATION UNIT
;  24-25 EC, CC-A1 TYPE A-1 CONTROLLER
;
; *******************************************************
;
        FRONTEND HIRAB
;
;       DEVICE DEFINITIONS:
;
;       DEVICE LOGICAL NAME, THE MODULE NAME, CRATE #, SLOT #,
;       SUBADDRESS
;
;       THE LOGICAL NAME IS USED IN THE QAL CODE TO REFER TO THE MODULE
;       AND SUBADDRESS, SEE USER$Q:QMODULE.DAT FOR A LISTING OF THE
;       DEVICES.
;
; 8 CHANNEL TDC (EVENT 8)
;
                                          ;HST,BLK,INDEX,COMMENTS
        DEVICE    TDCA0,LR2228,1,3,0  ;JITTER,1,25,LASER TIMING JITTER
;
; INTEGRATING ADC FOR LASER REALS (EVENT 8)
; LeCroy 2249W HAS A DYNAMIC RANGE OF 0.0 TO -2.0 VOLTS WITH THE
; SAME RESOLUTION OF 2249A.
```

```
                                               ;HIST,BLK,INDEX,COMMENTS
        DEVICE    ADCA0,LR2249,1,5,0 ;EREAL,1,1,e DETECTOR
        DEVICE    ADCA1,LR2249,1,5,1 ;HZ1R,1,2,H0(1) DETECTOR (TOP)
        DEVICE    ADCA2,LR2249,1,5,2 ;HZ2R,1,3,H0(2) DETECTOR (BOT)
        DEVICE    ADCA3,LR2249,1,5,3 ;HPR,1,4,H+ DETECTOR
        DEVICE    ADCA4,LR2249,1,5,4 ;PADDR,1,5,CERENKOV
        DEVICE    ADCA5,LR2249,1,5,5 ;FPDR,1,6,FAST PHOTO DIODE
;
;  INTEGRATING ADC FOR LASER ACCIDENTALS (EVENT 8)
;
                                     ;HIST,BLK,INDEX,COMMENTS
        DEVICE    ADCB0,LR2249,1,6,0 ;EACC,1,13, e-
        DEVICE    ADCB1,LR2249,1,6,1 ;HZ1A,1,14, H0(1)
        DEVICE    ADCB2,LR2249,1,6,2 ;HZ2A,1,15, H0(2)
        DEVICE    ADCB3,LR2249,1,6,3 ;HPA,1,16, H+
        DEVICE    ADCB4,LR2249,1,6,4 ;PADDA,1,17, CERENKOV
        DEVICE    ADCB5,LR2249,1,6,5 ;FPDA,1,18, FPD
;
; SCALER FOR LASER REALS (EVENT 8)
;
        DEVICE    SCA0,LR2551,1,8,0  ;e- . LASER DATA GATE
        DEVICE    SCA1,LR2551,1,8,1  ;H0(1) . LASER DATA GATE
        DEVICE    SCA2,LR2551,1,8,2  ;H0(2) . LASER DATA GATE
        DEVICE    SCA3,LR2551,1,8,3  ;H+ . LASER DATA GATE
        DEVICE    SCA4,LR2551,1,8,4  ;FIC . LASER DATA GATE
        DEVICE    SCA5,LR2551,1,8,5  ;RESERVED
;
; SCALER FOR LASER ACCIDENTALS (EVENT 8)
;
        DEVICE    SCB0,LR2551,1,9,0  ;e- . LASER BKGND GATE
        DEVICE    SCB1,LR2551,1,9,1  ;H0(1) . LASER BKGND GATE
        DEVICE    SCB2,LR2551,1,9,2  ;H0(2) . LASER BKGND GATE
        DEVICE    SCB3,LR2551,1,9,3  ;H+ . LASER BKGND GATE
        DEVICE    SCB4,LR2551,1,9,4  ;FIC . LASER BKGND GATE
        DEVICE    SCB5,LR2551,1,9,5  ;RESERVED
;
; SCALER FOR SPECTROMETER LASERLESS RUNS & MORE INSTRUMENTS (EVENT 9)
;
        DEVICE    SCC0,LR2551,1,10,0 ;e- . LASERLESS DATA GATE
        DEVICE    SCC1,LR2551,1,10,1 ;e- . LASERLESS BKGND GATE
        DEVICE    SCC2,LR2551,1,10,2 ;FIC . LASERLESS DATA GATE
        DEVICE    SCC3,LR2551,1,10,3 ;FIC . LASERLESS BKGND GATE
;
;  NIM OUTPUT REGISTER
;
        DEVICE    OUT,J00041,1,11,0
;
; 12 BIT ADC WITH 100 MOHMS IMPEDANCE
;
                                               ;HST,BLK,INDEX,COMMENTS
        DEVICE TBADC0,J00030,2,6,0   ;-,2,15, SPARE
;
***********************************************************
```

Appendix G

Fano fits

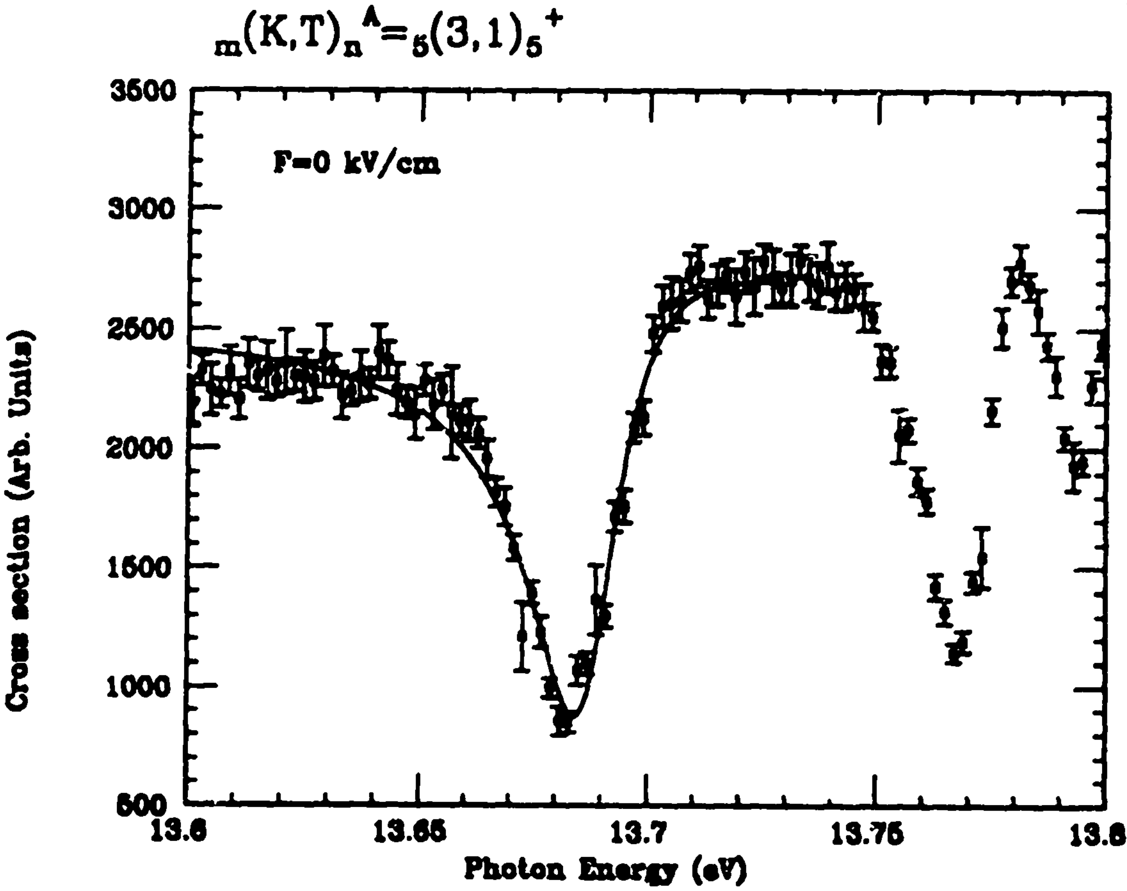

Figure G.1: Lowest resonance in $n=5$ manifold with $F=0$.

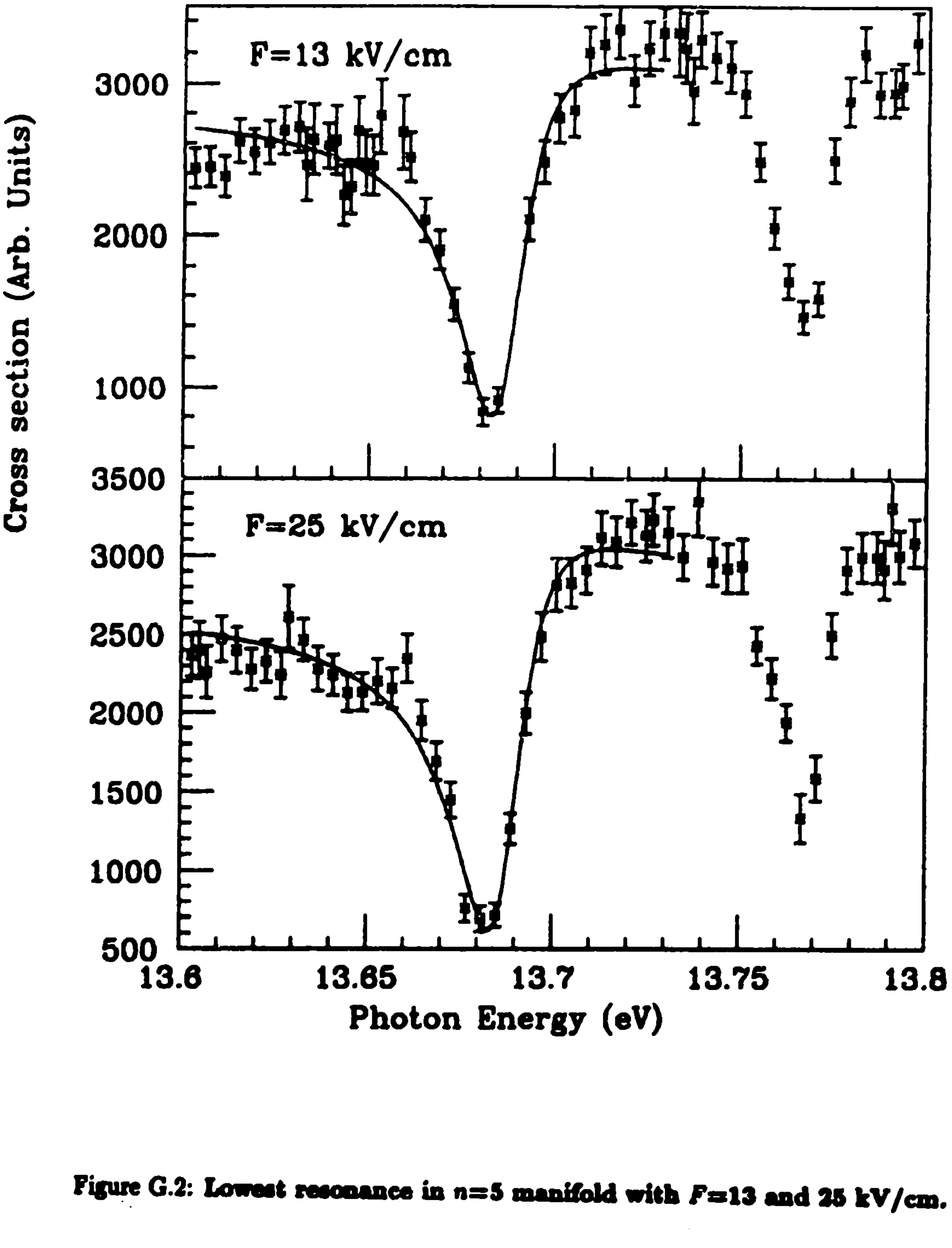

Figure G.2: Lowest resonance in $n=5$ manifold with $F=13$ and 25 kV/cm.

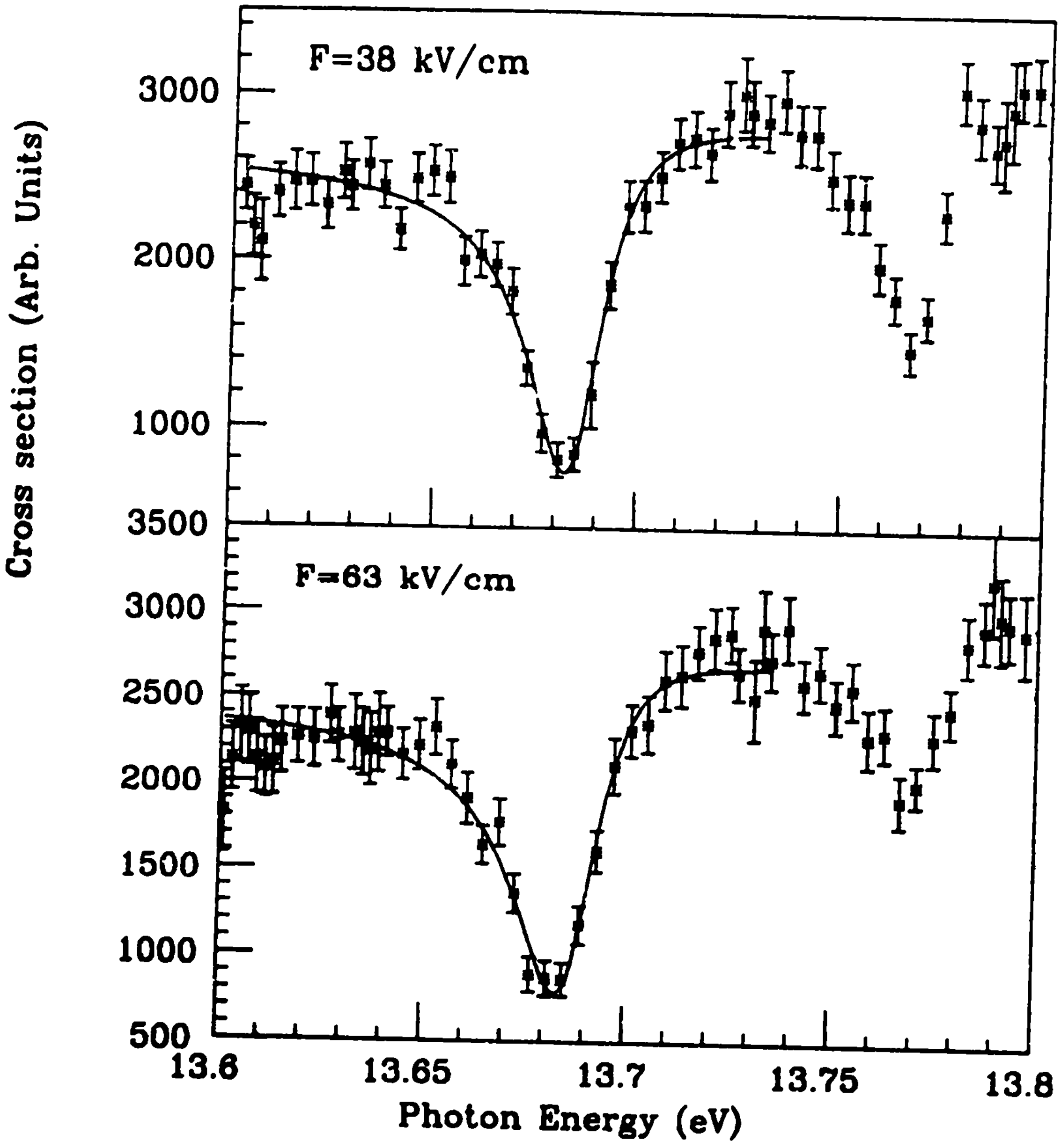

Figure G.3: Lowest resonance in $n=5$ manifold with $F=38$ and 63 kV/cm.

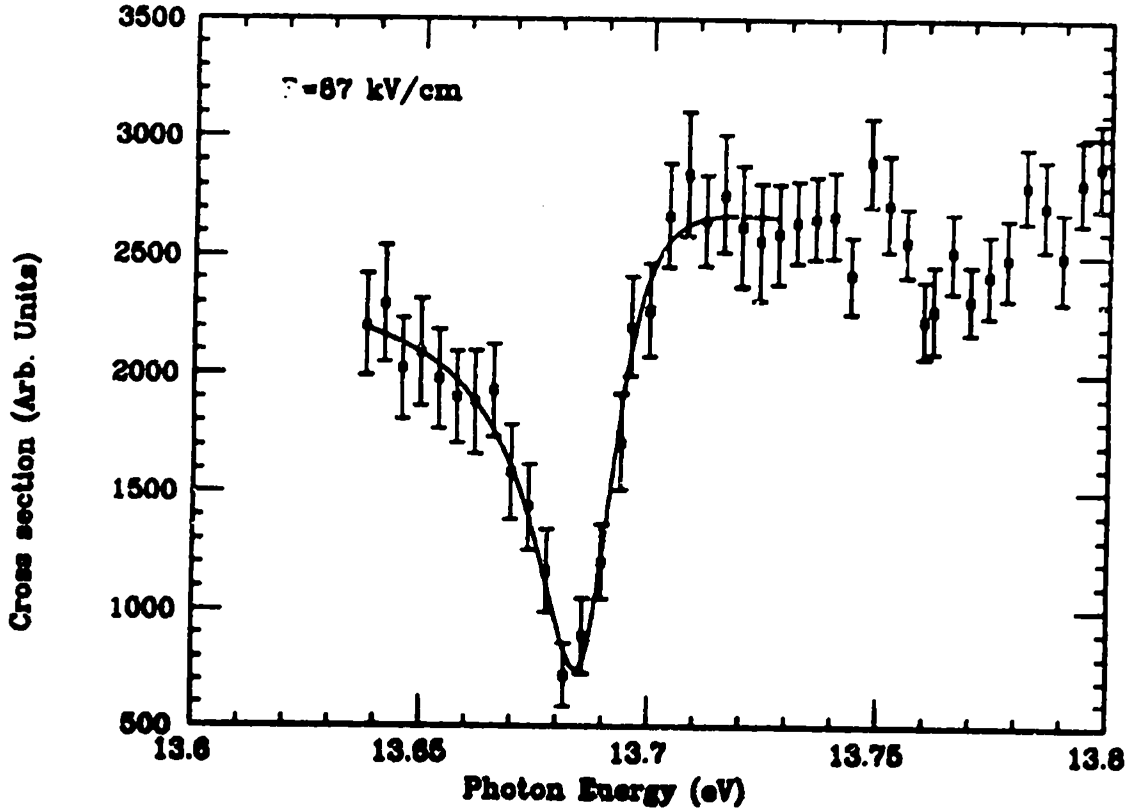

Figure G.4: Lowest resonance in $n=5$ manifold with $F=87$ kV/cm.

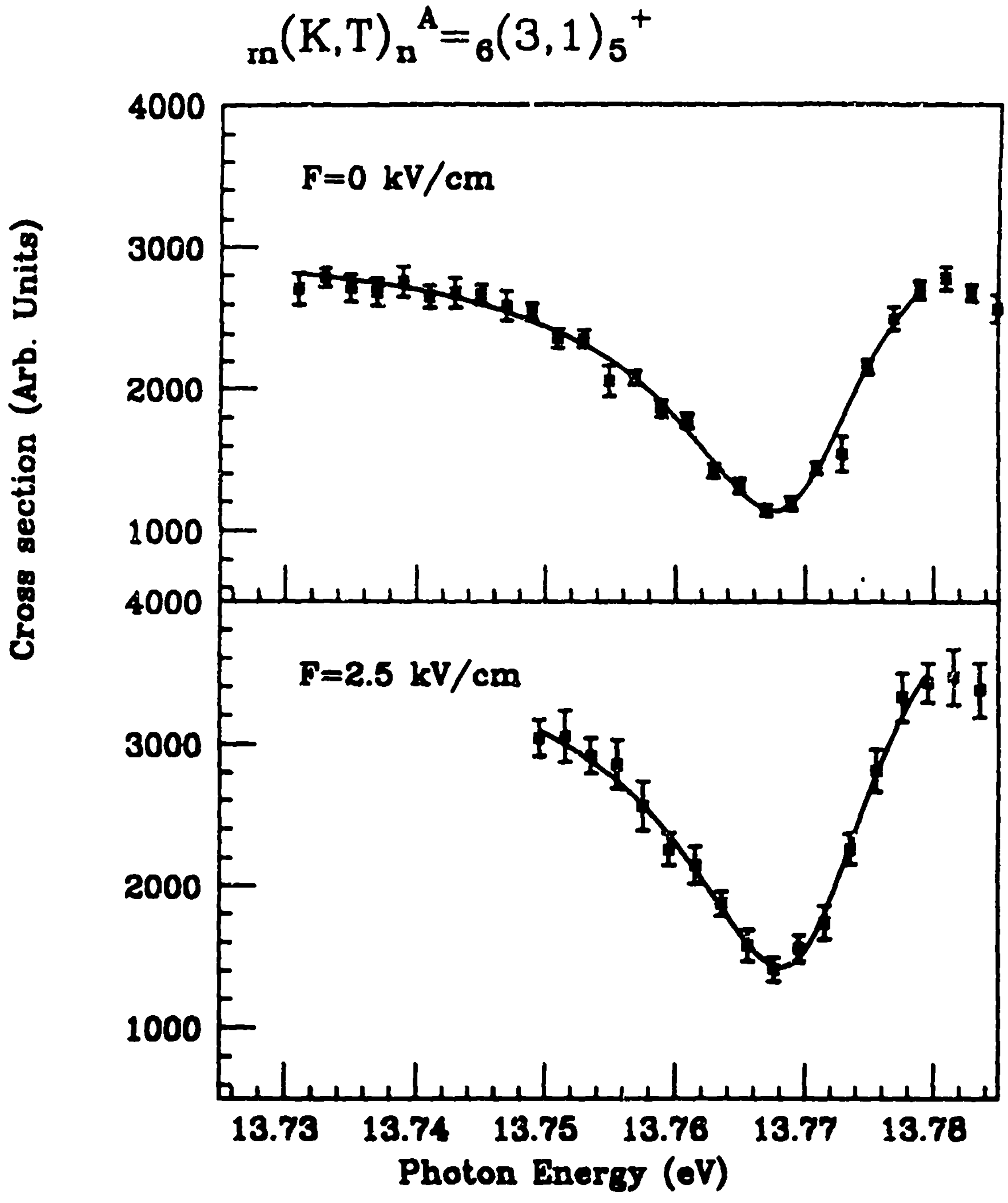

Figure G.5: Second resonance in $n=3$ manifold with $F=0$ and 2.5 kV/cm.

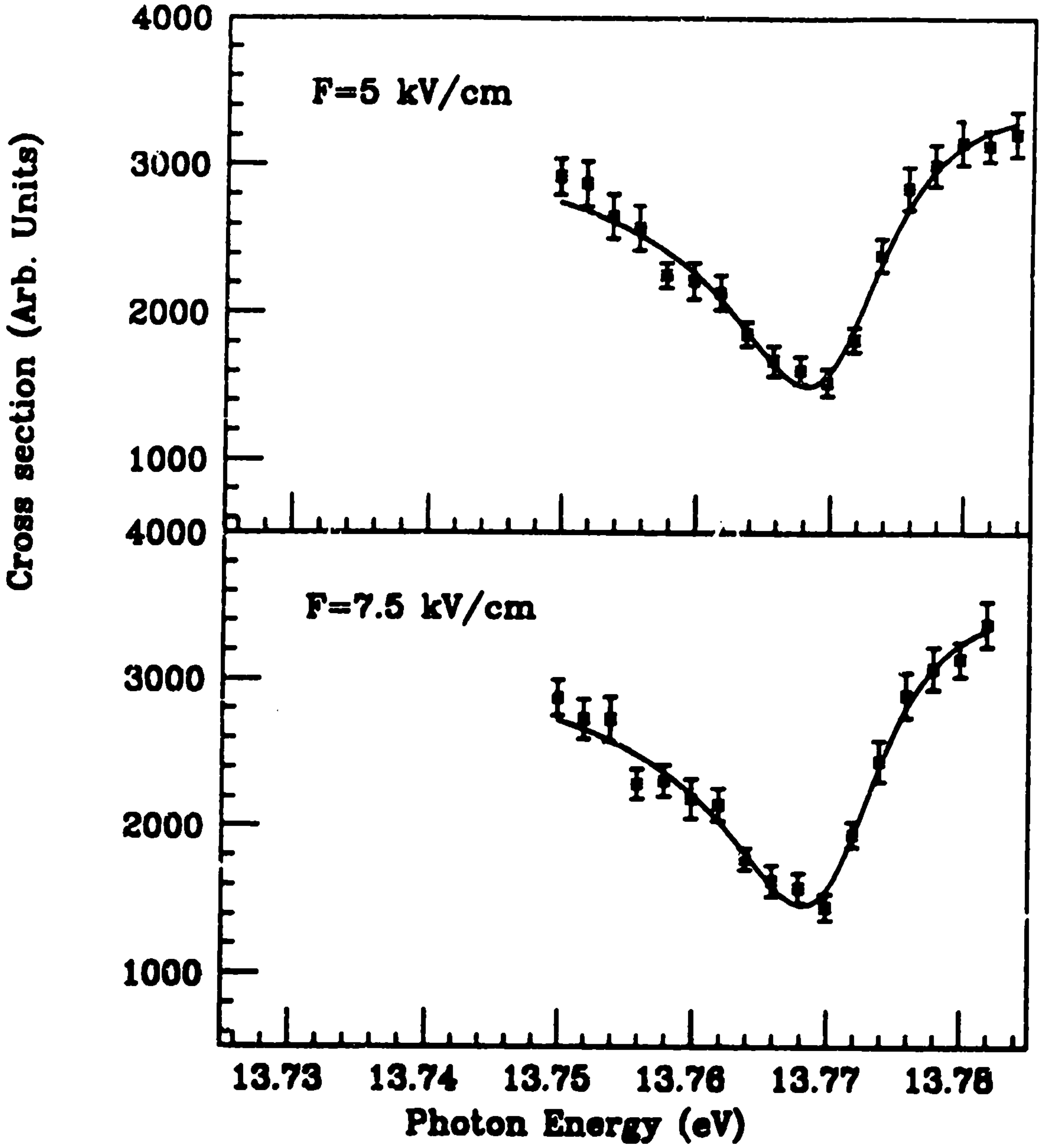

Figure G.6: Second resonance in $n=5$ manifold with $F=5$ and 7.5 kV/cm.

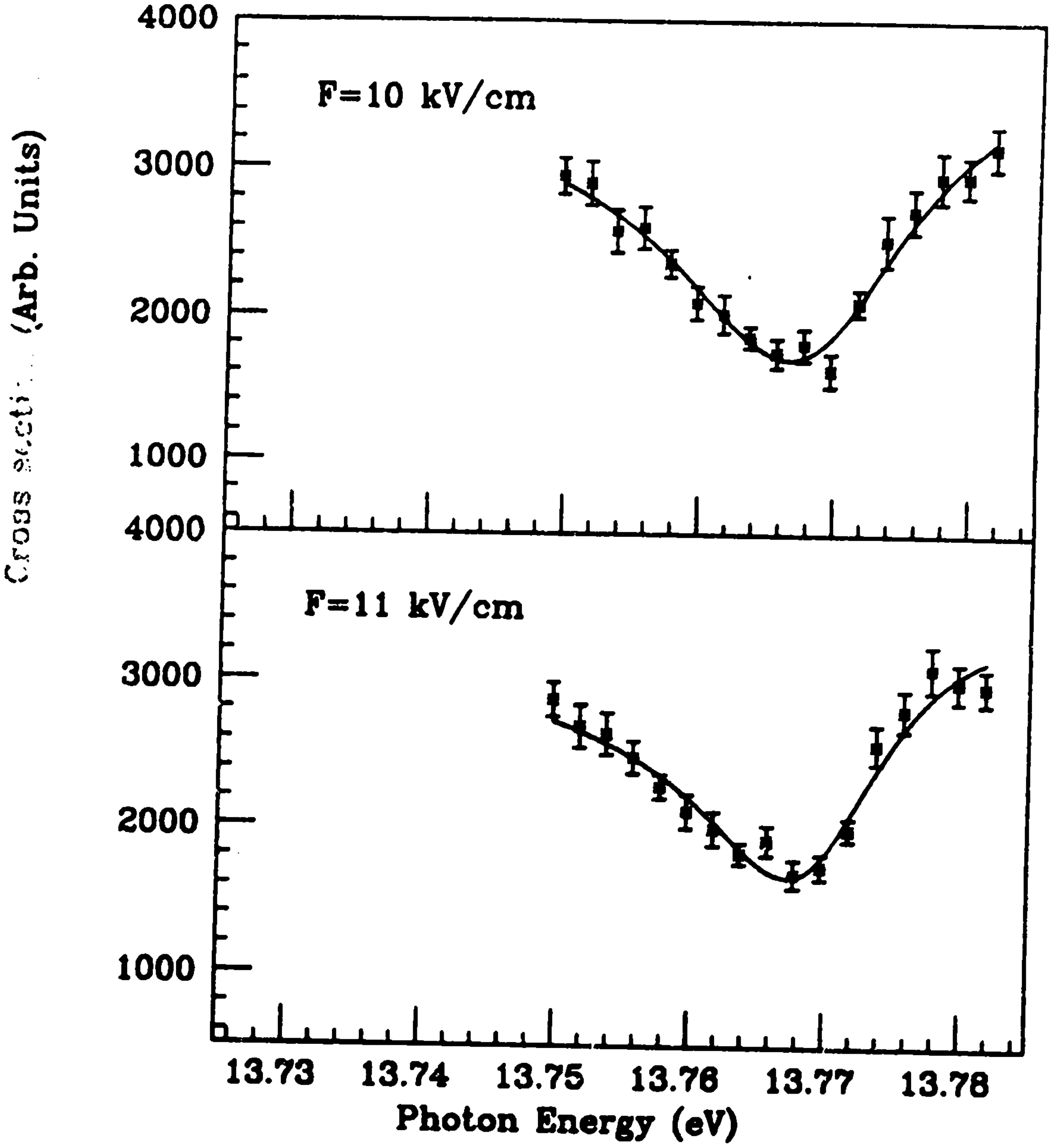

Figure G.7: Second resonance in $n=5$ manifold with $F=10$ and 11 kV/cm.

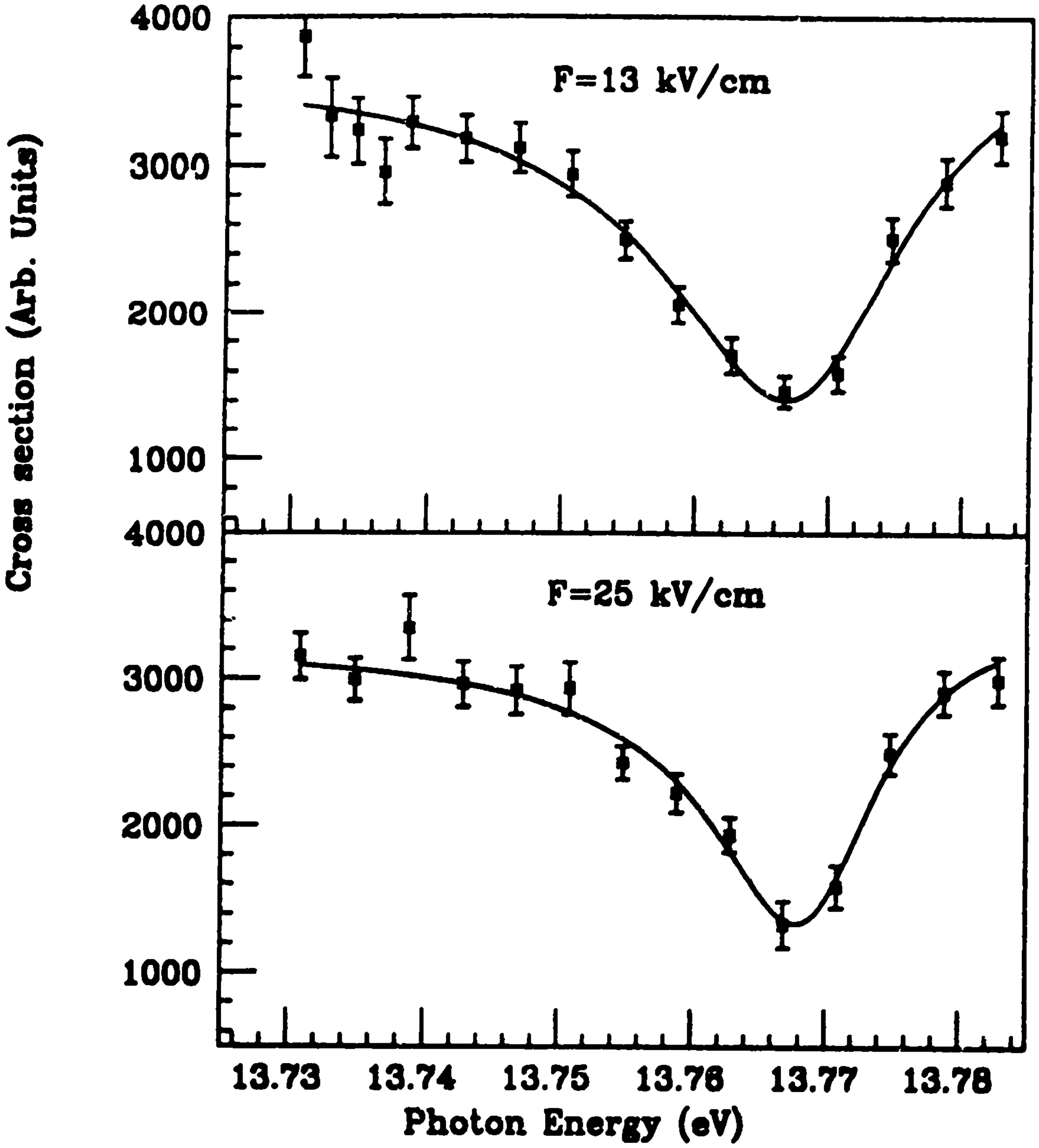

Figure G.8: Second resonance in $n=5$ manifold with $F=13$ and 25 kV/cm.

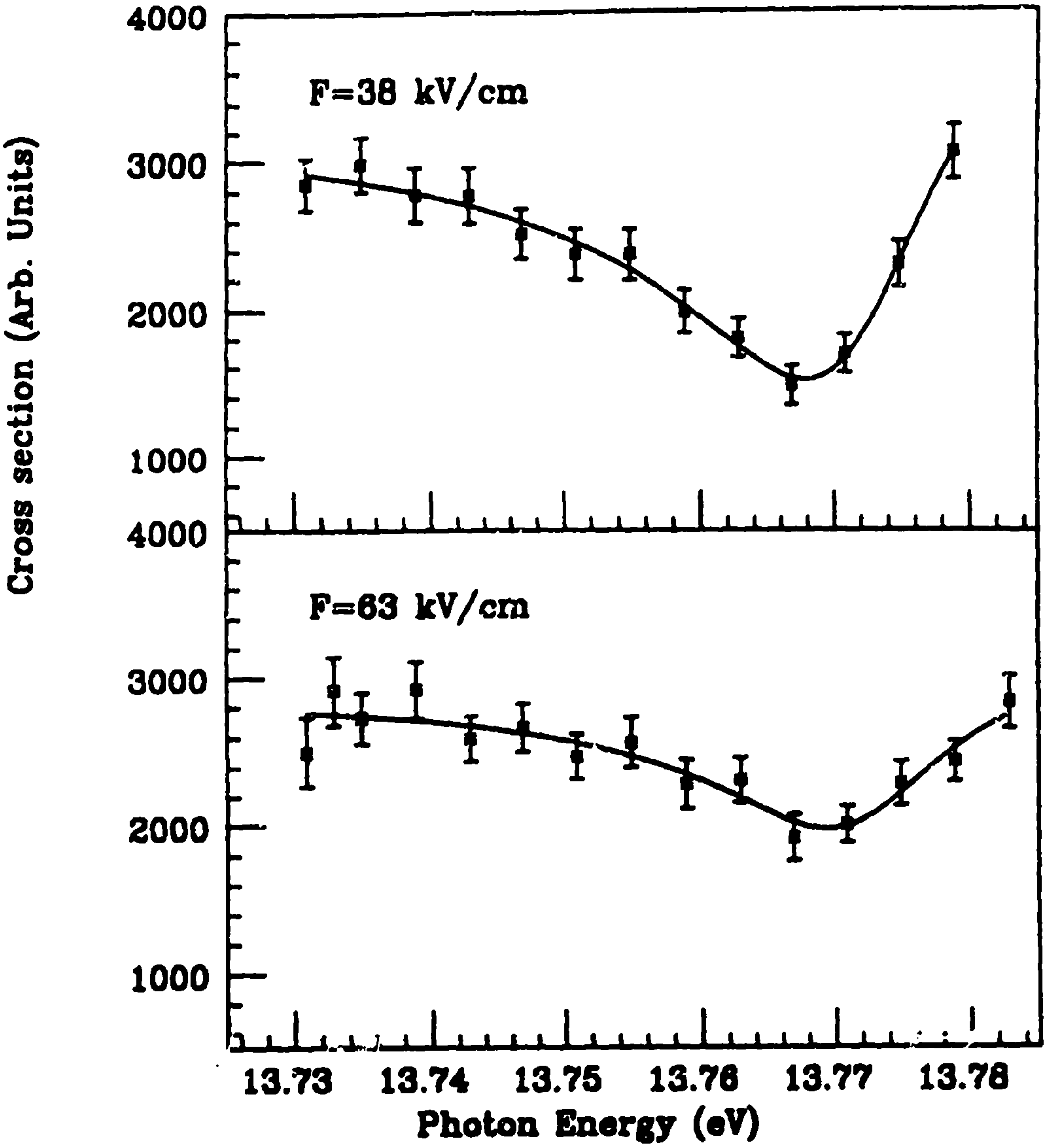

Figure G.9: Second resonance in $n=5$ manifold with $F=38$ and 63 kV/cm.

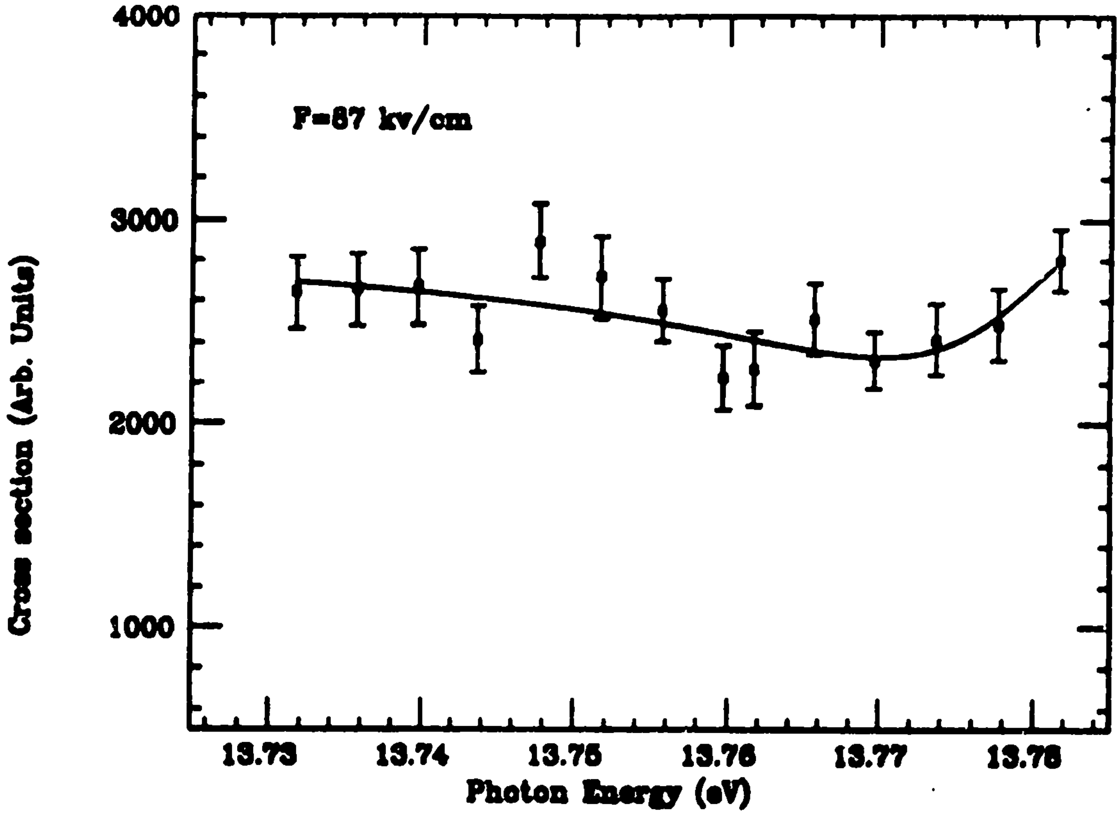

Figure G.10: Second resonance in n=5 manifold with F=87 kV/cm.

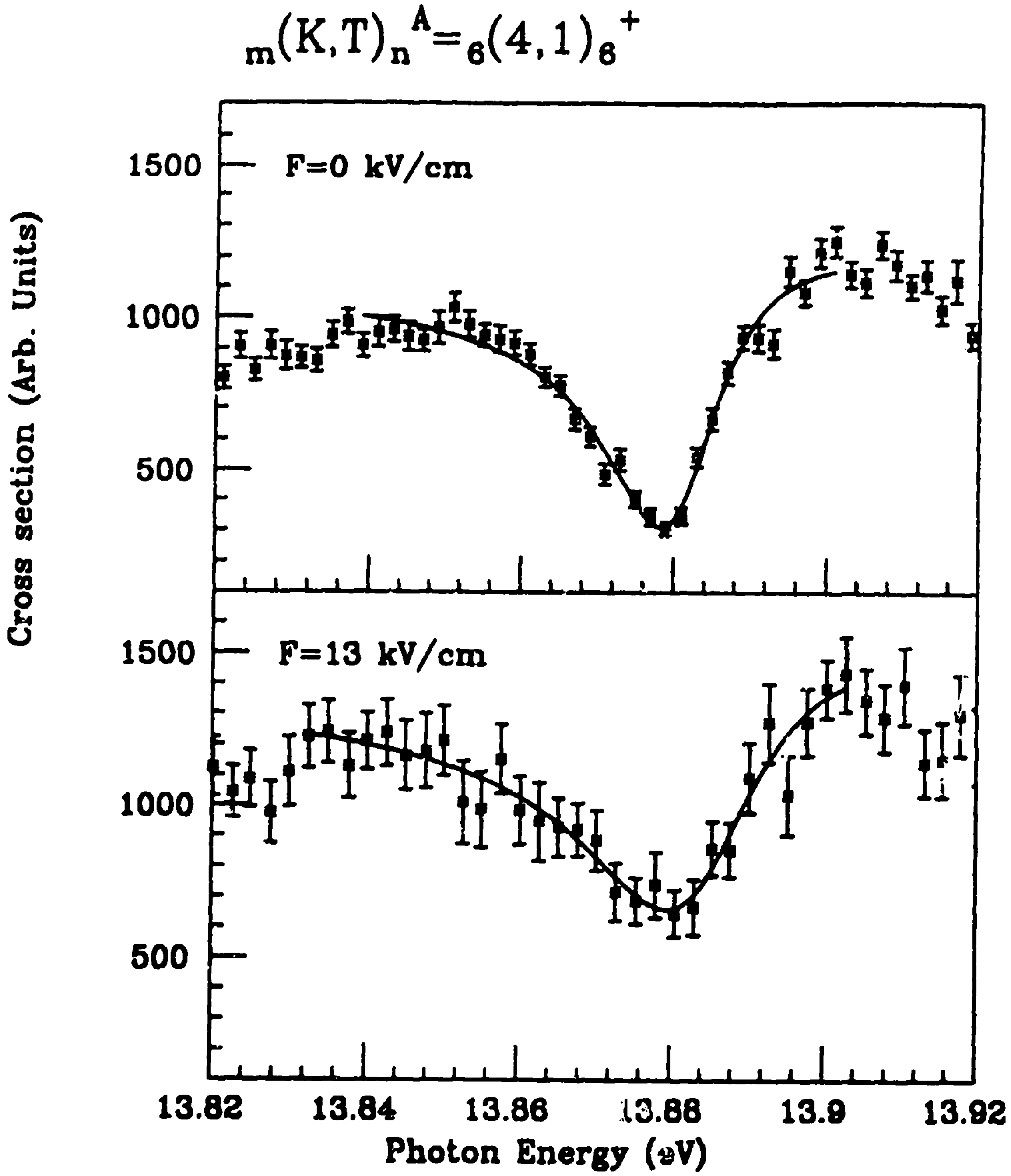

Figure G.11: Lowest resonance in $n=6$ manifold with $F=0$ and 13 kV/cm.

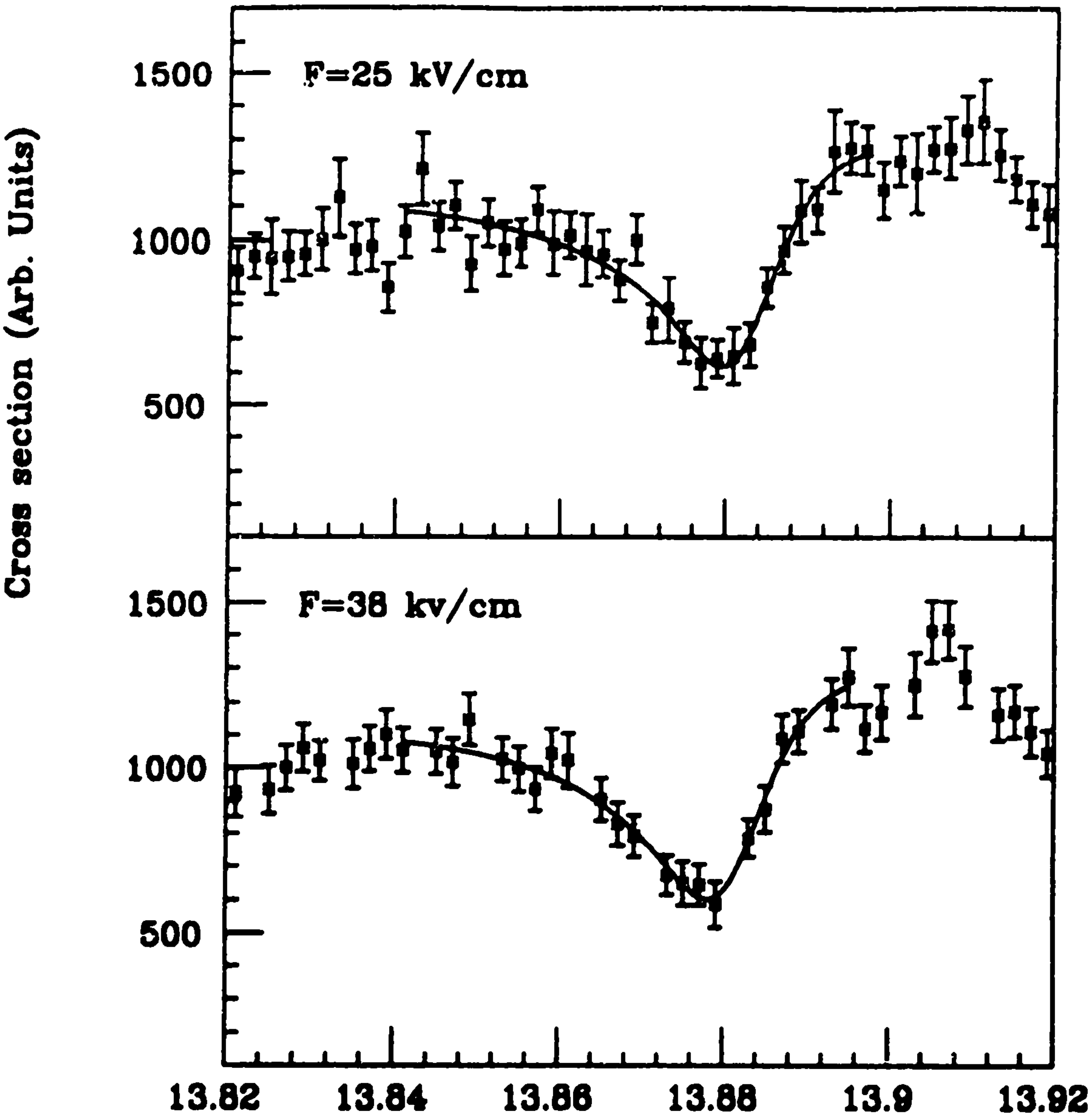

Figure G.12: Lowest resonance in $n=6$ manifold with $F=25$ and 38 kV/cm.

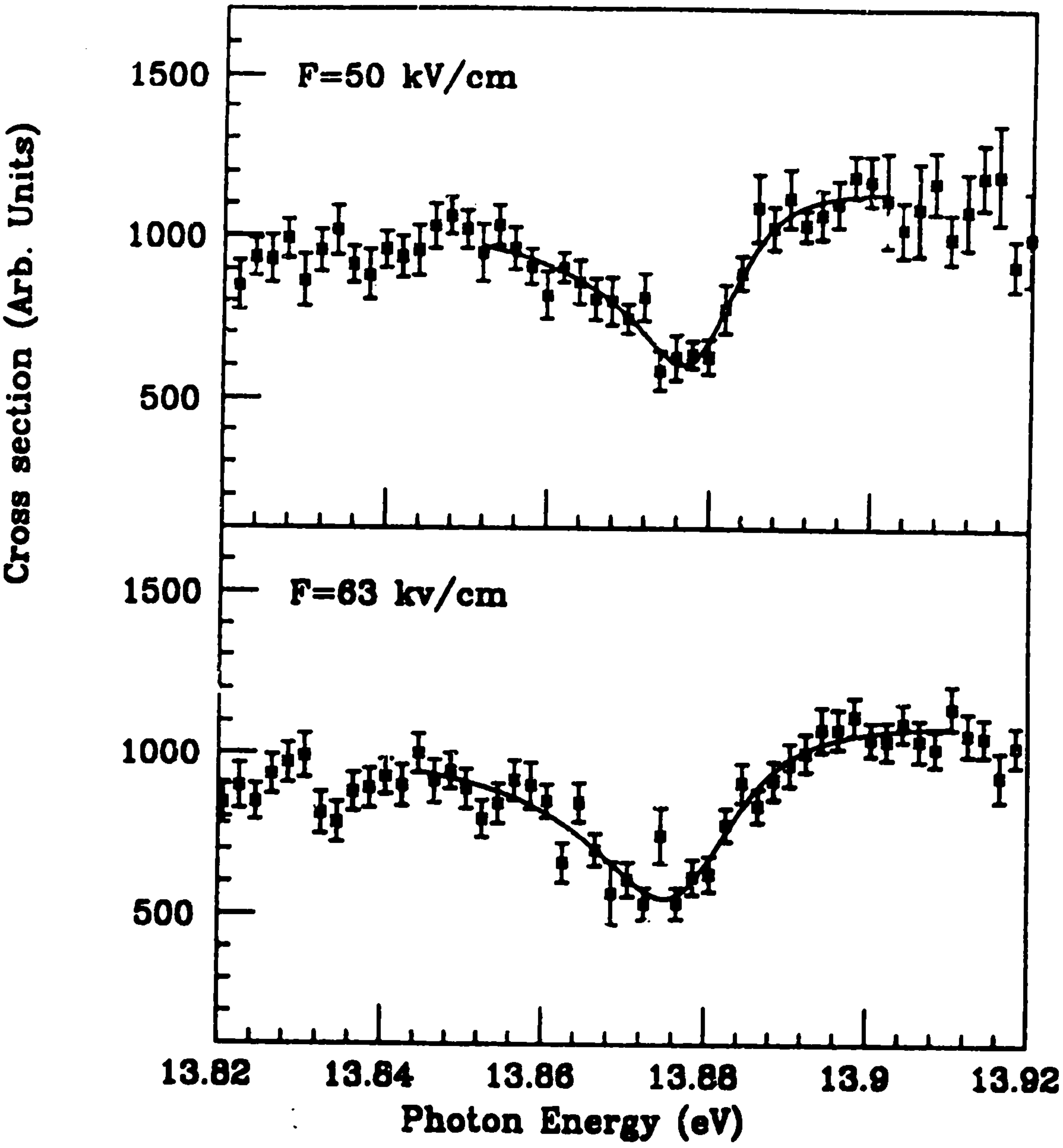

Figure G.13: Lowest resonance in $n=6$ manifold with $F=50$ and 63 kV/cm.

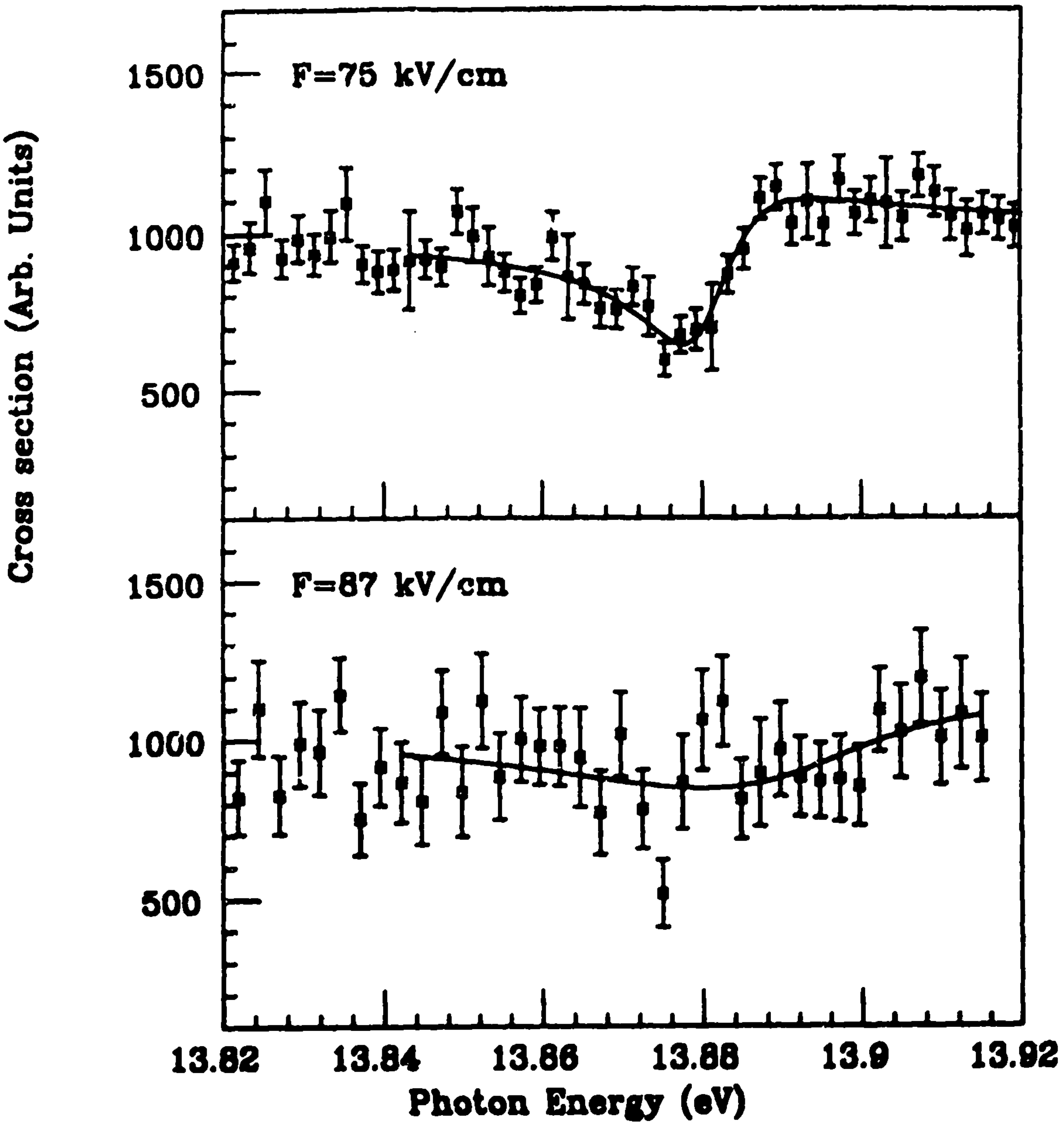

Figure G.14: Lowest resonance in $n=6$ manifold with $F=75$ and 87 kV/cm.

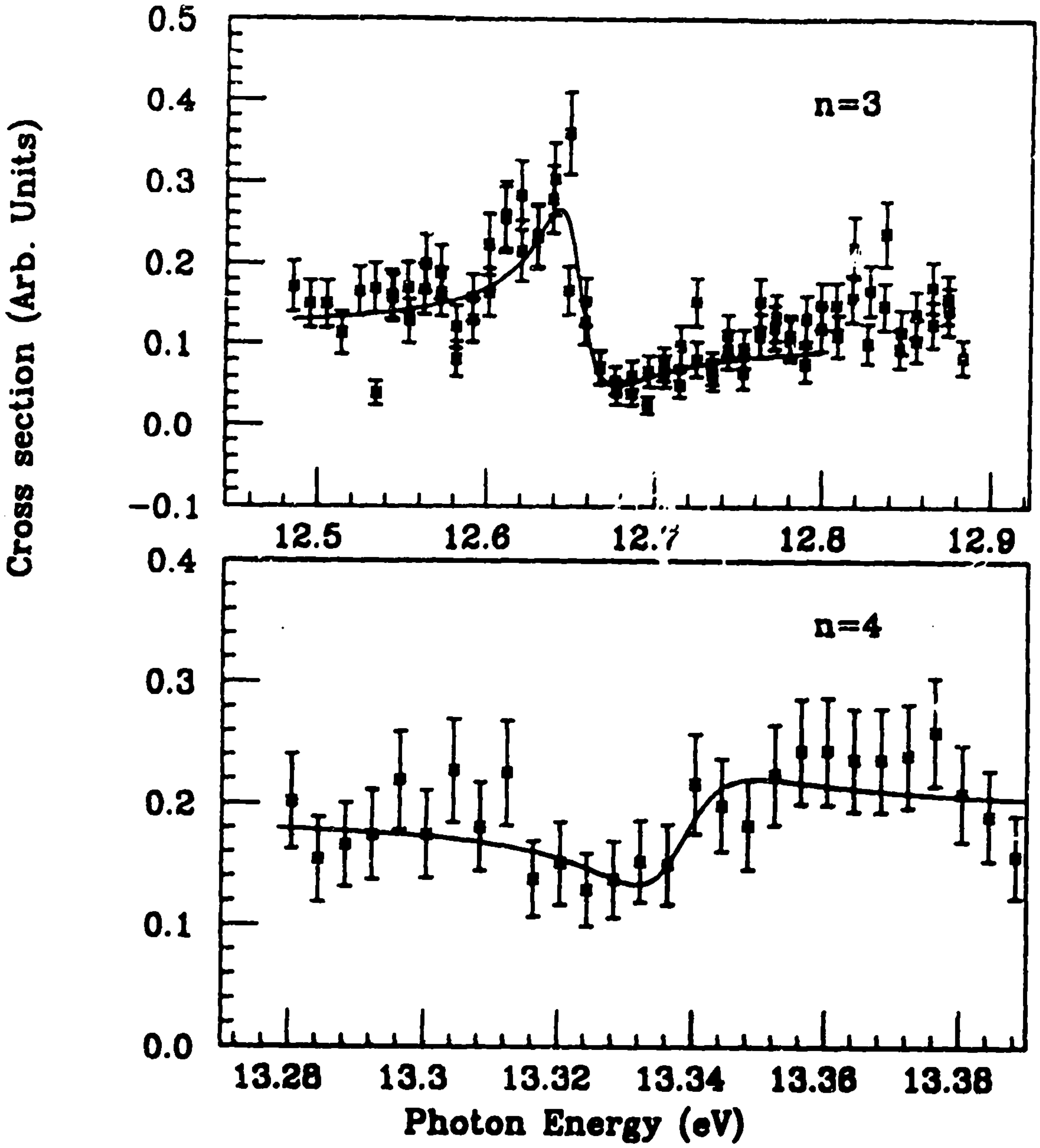

Figure G.15: Lowest resonance in n=3 manifold (top) and n=4 manifold (bottom) with F=0 kV/cm.

Appendix H

Fano parameters for resonances in applied fields

Fano widths Γ and central energies E_0 for ${}_m(K,T)_n^A$ resonances observed in various static field strengths F. The error, assigned by the fitting program MINUIT [65], is the deviation from the best fit value of the parameter that would increase its χ^2 value by one.

Resonance $_m(K,T)_n^A$	F (kV/cm)	E_0 (eV)	Γ (meV)
$_5(3,1)_5^+$	0.0	13.687(1)	23(1)
	13.0	13.686(1)	21(1)
	25.0	13.687(1)	21(1)
	38.0	13.685(1)	22(2)
	63.0	13.687(1)	24(2)
	87.0	13.688(1)	20(2)
$_6(3,1)_5^+$	0.0	13.770(1)	17(1)
	2.0	13.771(1)	18(2)
	5.0	13.770(1)	14(2)
	7.0	13.771(1)	14(2)
	10.0	13.768(1)	21(4)
	11.0	13.769(1)	17(3)
	13.0	13.768(1)	22(3)
	25.0	13.769(1)	15(2)
	38.0	13.773(2)	21(4)
	63.0	13.772(4)	21(9)
	87.0	13.780(17)	27(16)
$_7(3,1)_5^+$	0.0	13.792(2)	20(4)
	2.0	13.792(2)	15(4)
	5.0	13.795(2)	10(2)
	7.0	13.792(2)	12(3)
	10.0	13.791(2)	19(7)
	11.0	13.749(3)	16(1)
$_6(4,1)_6^+$	0.0	13.881(1)	18(1)
	13.0	13.884(2)	26(6)
	25.0	13.883(1)	17(3)
	38.0	13.882(1)	18(3)
	50.0	13.879(1)	17(3)
	63.0	13.878(1)	22(3)
	75.0	13.881(1)	13(2)
$_7(4,1)_6^+$	0.0	13.937(1)	15(1)
	13.0	13.933(2)	26(6)
	25.0	13.932(4)	32(14)

Appendix I

Shape resonance data of J. Callaway

Close-coupling/variational calculated ^1P partial cross sections (units of πa_0^2) for $1s-2s$ and $1s-2p$ excitation in H–e^- scattering (previously unpublished) [69].

k^2	$2s(a_0^2)$	$2p(a_0^2)$
0.7501	0.0008	0.0059
0.7502	0.0002	0.0119
0.7503	0.0011	0.0199
0.7504	0.0033	0.0303
0.7505	0.0072	0.0445
0.7506	0.0128	0.0632
0.7507	0.0206	0.0874
0.7508	0.0308	0.1181
0.7509	0.0431	0.1552
0.7510	0.0573	0.1974
0.7511	0.0722	0.2415
0.7512	0.0860	0.2827
0.7513	0.0972	0.3158
0.7514	0.1042	0.3378
0.7515	0.1069	0.3473
0.7516	0.1060	0.3460
0.7517	0.1024	0.3370
0.7518	0.0972	0.3231
0.7519	0.0913	0.3068
0.7520	0.0852	0.2897
0.7521	0.0792	0.2730
0.7522	0.0735	0.2573
0.7523	0.0683	0.2426
0.7524	0.0636	0.2293
0.7525	0.0593	0.2171
0.7530	0.0433	0.1717
0.7535	0.0335	0.1435
0.7540	0.0271	0.1248
0.7550	0.0193	0.1021
0.7560	0.0150	0.0888
0.7570	0.0122	0.0801
0.7580	0.0103	0.0740
0.7600	0.0079	0.0659

Appendix J

Shape resonance width

Below is a plot of the FWHM of the H^{-**} shape resonance as a function of field strength [95]. The experimental data is from Ref. [25]. The solid line represents unpublished theoretical predictions from R-matrix calculations of C. H. Greene and V. Z. Slonim (private communication).

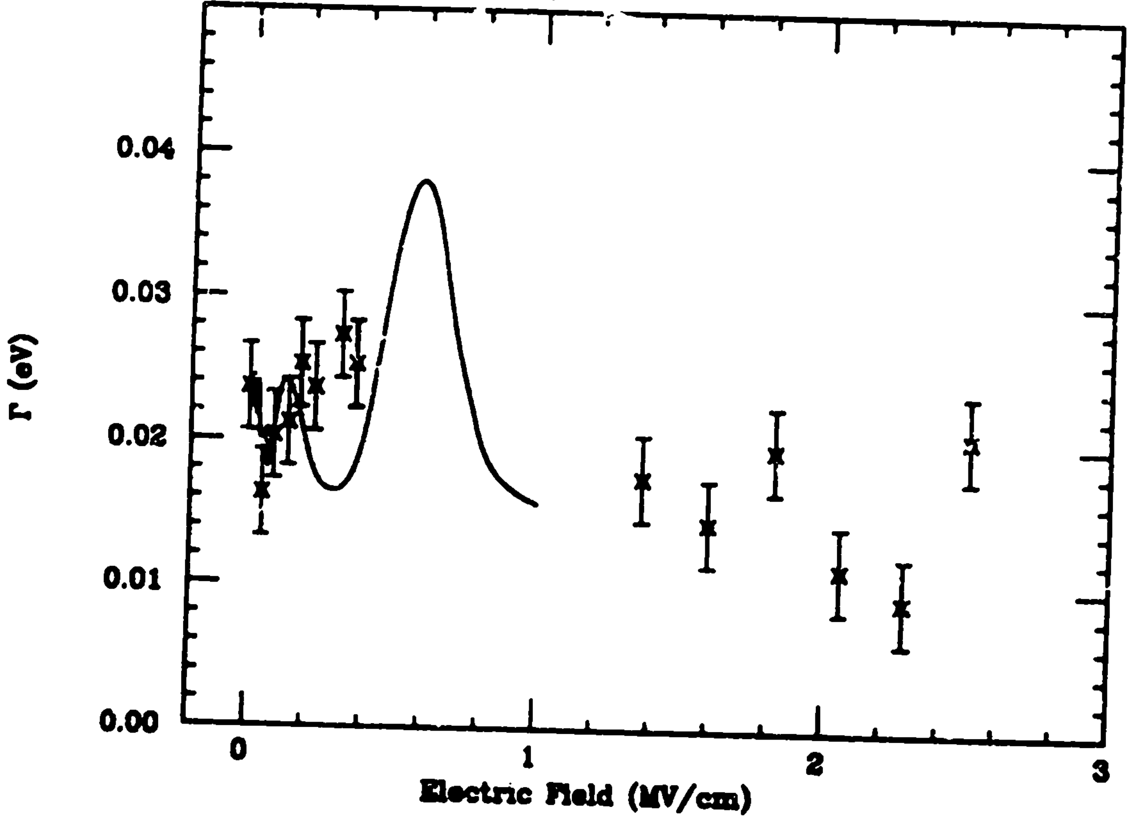

Bibliography

[1] H. R. Sadeghpour, Chris H. Greene, and Michael Cavagnero, Phys. Rev. A **45**, 1587 (1992).

[2] Hans A. Bethe and Edwin E. Salpeter, *Quantum Mechanics of One- and Two-Electron Atoms* (Academic Press, 1957).

[3] G. J. Schulz and R. E. Fox, Phys. Rev. **106**, 1179 (1957).

[4] E. P. Wigner, Phys. Rev. **73**, 1002 (1948).

[5] E. Baranger and E. Gerjuoy, Phys. Rev. **106**, 1182 (1957).

[6] S. Silverman and E. N. Lassettre, Rept. 9, R. F. Project 464, Ohio State University Research Foundation, Columbus, Ohio (1958, unpublished); see also U. Fano, reference [7].

[7] U. Fano, Phys. Rev. **124**, 1866 (1961).

[8] P. G. Burke and H. M. Schey, Phys. Rev. **126**, 147 (1962).

[9] R. P. Madden and K. Codling, Phys. Rev. Lett **10**, 516 (1963).

[10] J. W. Cooper, U. Fano, and F. Prats, Phys. Rev. Lett. **10**, 518 (1963).

[11] N. Bohr, Nature **137**, 351 (1936).

[12] H. Feshbach, Ann. Phys. **5**, 357 (1958) and **19**, 287 (1962).

[13] In the past these states have also been labeled as core excited I, compound state, or hole-particle resonances [14].

[14] H. S. Taylor, Adv. Chem. Phys., **18**, 91 (1970).

[15] U. Fano and A. R. P. Rau, *Atomic Collisions and Spectra* (Academic Press, 1986).

[16] H. R. Sadeghpour and Chris H. Greene, Phys. Rev. Lett. **65**, 313 (1990).

[17] H. R. Sadeghpour, Phys. Rev. A **43**, 5821 (1991).

[18] A. Joanna Taylor and P. G. Burke, Proc. Phys. Soc. **92**, 336 (1967).

[19] J. Macek, Proc. Phys. Soc. **92**, 365 (1967).

[20] J. W. McGowan, J. F. Williams, and F. K. Carley, Phys. Rev. **180**, 132 (1969).

[21] J. F. Williams and B. A. Willis, J. Phys. B **7**, L61 (1974).

[22] H. Tootoonchi Sarraf, Ph.D. dissertation, University of New Mexico (1977).

[23] D. W. MacArthur, K. B. Butterfield, D. A. Clark, J. B. Donahue, P. A. M. Gram, H. C. Bryant, C. J. Harvey, W. W. Smith, and G. Comtet, Phys. Rev. A **32**, 1921 (1985).

[24] M. E. Hamm, R. W. Hamm, J. Donahue, P. A. M. Gram, J. C. Pratt, M. A. Yates, R. D. Bolton, D. A. Clark, H. C. Bryant, C. A. Frost, and W. W. Smith, Phys. Rev. Lett. **43**, 1715 (1979).

[25] Kenneth B. Butterfield, Ph.D. dissertation, University of New Mexico (1983).

[26] P. G. Harris, H. C. Bryant, A. H. Mohagheghi, R. A. Reeder, C. Y. Tang, J. B. Donahue, and C. R. Quick, Phys. Rev. A **42**, 6443 (1990).

[27] Chris H. Greene and H. R. Sadeghpour, Phys. Rev. Lett. **65**, 313 (1990).

[28] Bin Zhou and C. D. Lin, Phys. Rev. Lett. **69**, 3294 (1992).

[29] Anthony F. Starace, Phys. Rev. A **16**, 231 (1977)

[30] M. Chrysos, Y. Komninos, Th. Mercouris, and C. A. Nicolaides, Phys. Rev. A **42**, 2634 (1990).

[31] C. H. Greene, private communication.

[32] A. R. P. Rau, private communication.

[33] M. Halka, H. C. Bryant, E. P. Mackerrow, W. Miller, A. H. Mohagheghi, C. Y. Tang, S. Cohen, J. B. Donahue, A. Hsu, C. R. Quick, J. Tiee, and K. Rózsa, Phys. Rev. A **44**, 6127 (1991).

[34] P. A. M. Gram, J. C. Pratt, M. A. Yates-Williams, H. C. Bryant, J. Donahue, H. Sharifian, and H. Tootoonchi, Phys. Rev. Lett. **40**, 107 (1978).

[35] H. A. Hyman, V. L. Jacobs, and P. G. Burke, J. Phys. B **5**, 2282 (1972).

[36] John T. Broad and William P. Reinhardt, Phys. Rev. A **14**, 2159 (1976).

[37] A. W. Wishart, J. Phys. B **12**, 3511 (1979).

[38] Chih-Ray Liu, Nin-Ying Du, and Anthony F. Starace, Phys. Rev. A **43**, 5891 (1991).

[39] Michael Chrysos, Yannis Komninos, and Cleanthes A. Nicolaides, J. Phys. B **25** (1992).

[40] H. C. Bryant, A. Mohagheghi, J. E. Stewart, J. B. Donahue, C. R. Quick, R. A. Reeder, V. Yuan, C. R. Hummer, W. W. Smith, Stanley Cohen, William P. Reinhardt, and Lillian Overman, Phys. Rev. Lett. **58**, 2412 (1987).

[41] P. G. Harris , H. C. Bryant. A. H. Mohagheghi, C. Tang, J. B. Donahue, C. R. Quick, R. A. Reeder, Stanley Cohen, W. W. Smith, J. E. Stewart, and Carol Johnstone, Phys. Rev. A **41**, 5968 (1990) and references therein.

[42] M. L. Du and J. B. Delos, Phys. Rev. A **38**, 5609 (1988).

[43] A. R. P. Rau and Hin-Yiu Wong, Phys. Rev. A **37**, 632 (1988).

[44] Hin-Yiu Wong, A. R. P. Rau, and Chris H. Greene, Phys. Rev. A **37**, 2393 (1988).

[45] M. Gailitis and R. Damburg, Proc. Phys. Soc. 82, 192 (1963).

[46] Chris Greene and A. R. P. Rau, Phys. Rev. A **32**, 1352 (1985).

[47] H. R. Sadeghpour, unpublished calculations (private communication, 1991).

[48] Note that for $n \geq 9$ decay to the H($n - 1$) continuum becomes energetically forbidden in zero-field [17, 26].

[49] Chii-Dong Lin (private communication, 1991).

[50] Y. K. Ho and J. Callaway, Phys. Rev. A **34**, 130 (1986).

[51] Anil Pathak, A. E. Kingston, and K. A. Berrington, J. Phys. B **21**, 2939 (1988).

[52] V. Z. Slonim and Chris H. Greene, Radiation Effects and Defects in Solids **122-123**, 679 (1991).

[53] P. W. Schmor, Helvetica Physica Acta **59**, 643-651 (1986).

[54] John C. Allred *et al*, *lampf*, edited by John C. Allred and Beverly Talley, Los Alamos report LA-UR-87-327 (1987).

[55] L. D. Landau and E. M. Lifshitz, *Quantum Mechanics: Non-Relativistic Theory*, (Addison-Wesley, 1965).

[56] For example, see Wolfgang Rindler, *Essential Relativity* (Springer-Verlag, 1977).

[57] Philip G. Harris, Ph.D. dissertation, University of New Mexico (1990).

[58] L. Lipsky and M. J. Conneely, Phys. Rev. A **14**, 2193 (1976).

[59] *Quanta-Ray Pulsed Nd:YAG Laser Instruction Manual*, Spectra-Physics Lasers (Darmstadt, 1991).

[60] James E. Stewart, Ph.D. dissertation, University of New Mexico (198)7.

[61] S. J. Lindenbaum and Luke C. L. Yuan in *Methods of Experimental Physics*, Vol. 5a, edited by Luke C. L. Yuan and Chien-Shiung Wu, (Academic Press, 1963).

[62] Richard J. Barrett, Bryon D. Anderson, Harvey B. Willard, Alan N. Anderson, and Nelson Jarmie, Nucl. Instr. Meth. **129**, 441 (1975).

[63] See Los Alamos National Laboratory Documents MP-1-3411-2,3,5,6.

[64] A. H. Mohagheghi, Ph.D. dissertation, University of New Mexico (1990).

[65] F. James and M. Roos, Comput. Phys. Commun. **10**, 343 (1975).

[66] John T. Broad (private communication, 1991).

[67] J. R. Peterson, Y. K. Bai, and D. L. Huestis, Phys. Rev. Letters **7**, 692 (1985).

[68] H. R. Sadeghpour, unpublished R-matrix calculations (private communication, 1992).

[69] J. C. Callaway, unpublished variational calculations (private communication, 1992).

[70] Stanley Cohen, H. C. Bryant, C. J. Harvey, J. E. Stewart, K. B. Butterfield, D. A. Clark, J. B. Donahue, D. W. MacArthur, G. Comtet, and W. W. Smith, Phys. Rev. A **36**, 4728 (1987).

[71] R. S. Oberoi, J. Phys. B: Atom. Molec. Phys. **5**, 1120 (1972).

[72] C. A. Nicolaides and Y. Komninos, Phys. Rev. A **35**, 999 (1987).

[73] J. Callaway, Phys. Lett. 75a, 43 (1979).

[74] A. R. P. Rau, Science 258, 1444 (1992).

[75] Philip R. Bevington, *Data Reduction and Error Analysis for the Physical Sciences* (McGraw-Hill, 1969).

[76] For example, see C. D. Lin in *Few-Body Methods: Principles & Applications*, pp. 507-543, edited by T. K. Lim, C. G. Bao, D. P. Hou, and H. S. Huber (World Scientific, Singapore, 1986).

[77] H. Tootoonchi Sarraf, Ph.D. dissertation, University of New Mexico (1977); H. C. Bryant, David A. Clark, Kenneth B. Butterfield, C. A. Frost, H. Sharifian, H. Tootoonchi, J. B. Donahue, P. A. M. Gram, M. E. Hamm, R. W. Hamm, J. C. Pratt, M. A. Yates, and W. W. Smith, Phys. Rev. A 27, 2889 (1983); H. C. Bryant in *Electronic and Atomic Collisions*, edited by N. Oda and K. Takayanagi, (North-Holland, 1980); G. Comtet, C. J. Harvey, J. E. Stewart, H. C. Bryant, K. B. Butterfield, D. A. Clark, J. B. Donahue, P. A. M. Gram, D. W. MacArthur, V. Yuan, W. W. Smith, and Stanley Cohen, Phys. Rev. A 35, 1547 (1987); P. A. M. Gram, J. C. Pratt, M. A. Yates-Williams, H. C. Bryant, J. Donahue, H. Sharifian, and H. Tootoonchi, Phys. Rev. Lett. 40, 107 (1978).

[78] The apparent structure below the H(4) threshold when F=0 is thought to be an artifact of our detection scheme. Below threshold H^{-**}(4) states are created but should not be observed since, in this measurement, protons from field-stripping of H(4)s are detected, and it is not energetically possible for H^{-**}(4)

to decay to H(4) when no external field is present. Since the resonant states decay within the laser volume, however, there is a finite probability for H(3) states to be stripped to protons by laser photons within the first interaction region. If these states result from decay of $H^{-**}(4)$s, they might appear as peaks below threshold. These appear to be quenched when static fields are applied. Analysis by subtraction of zero-field from applied-field cross sections assures us that these spurious peaks are completely quenched in F >50 kV/cm, and do not contribute significantly to the spectra.

[79] C. Y. Tang, P. G. Harris, A. H. Mohagheghi, H. C. Bryant, C. R. Quick, J. B. Donahue, R. A. Reeder, Stanley Cohen, W. W. Smith, and J. E. Stewart, Phys. Rev. A **39**, 6068 (1989).

[80] A. H. Mohagheghi, H. C. Bryant, P. G. Harris, R. A. Reeder, H. Sharifian, C. Y. Tang, H. Tootoonchi, C. R. Quick, S. Cohen, W. W. Smith, and J. E. Stewart, Phys. Rev. A **43**, 1345 (1991).

[81] M. Halka, H. C. Bryant, C. J. Harvey, B. Marchini, E. P. MacKerrow, W. Miller, A. H. Mohagheghi, C. Y. Tang, K. B. Butterfield, D. A. Clark, S. Cohen, J. B. Donahue, P. A. M. Gram, R. W. Hamm, A. Hsu, D. W. MacArthur, C. R. Quick, J. Tiee, and K. Rózsa, Phys. Rev. A **46**, 6942 (1992).

[82] W. Reinhardt, Talk given at workshop on *New Developments in Two-Electron Atoms and Ions*, Boulder, CO, July 22-25, 1992.

[83] G. Comtet, C. J. Harvey, J. E. Stewart, H. C. Bryant, K. B. Butterfield, D. A. Clark, J. B. Donahue, P. A. M. Gram, D. W. MacArthur, V. Yuan, W. W. Smith, and Stanley Cohen, Phys. Rev. A 35, 1547 (1987).

[84] I. I. Fabrikant, Phys. Rev. A 40, 2373 (1989).

[85] A. Temkin, J. Phys. B 7, L450 (1974).

[86] J. H. Macek, J. Phys. B 1, 831 (1968).

[87] Birte L. Christensen-Dalsgaard, Phys. Rev. A 29, 470 (1976).

[88] David R. Herrick, Phys. Rev. A. 12, 413 (1975).

[89] S. Watanabe and C. D. Lin, Phys. Rev. A 34, 823 (1986).

[90] Z. Chen and C. D. Lin, Phys. Rev. A 42, 18 (1990).

[91] C. D. Lin, Phys. Rev. Lett. 35, 1150 (1975).

[92] J. M. Rost and J. S. Briggs, J. Phys. B 24, 4293 (1991).

[93] J. S. Briggs (private communication, 1992).

[94] This quantity has been called ${}_nv^A$ in Ref. [17] and others, but is not to be confused with v in Ref. [89] where $v = n - K - 1$. In reference [89], our n is called N, and ${}_nv^A$ is called n.

[95] The widths given here differ from the widths quoted in Ref. [25] which were calculated by fits to the Fano function. As mentioned in Chapter 6, the Fano width is probably not a very reliable measure for the shape resonance.

*U.S. GOVERNMENT PRINTING OFFICE: 1993-774-036/67016